

Numerical Long-Time Analysis of Compact Binary Systems

Diplomarbeit von Jonathan Seyrich

Jonathan Seyrich
Numerical Analysis Group
Eberhard-Karls-Universität Tübingen
Mathematisches Institut
Auf der Morgenstelle 10, 72076 Tübingen

supervised by
Prof. Dr. Wilhelm Kley and *Prof. Dr. Christian Lubich*

December 13, 2012

Erklärung gemäß § 18 (7) der Diplomprüfungsordnung

Hiermit erkläre ich, dass ich diese Arbeit selbständig verfasst und keine anderen als die angegebenen Quellen und Hilfsmittel benutzt habe.

Tübingen, den 03. Dezember 2012

Jonathan Seyrich

Zusammenfassung

Seit Albert Einstein 1915 mit seinen Bewegungsgleichungen für Gravitationsfelder die physikalische Beschreibung der Masse revolutionierte, zählen die mit dieser Theorie verbundenen und durch sie vorhergesagten Phänomene zu den aufregendsten Forschungsgebieten der Wissenschaft.

Eines dieser Phänomene, die *Gravitationswellen*, waren dabei in den letzten Jahren Objekt besonders großen Interesses. Die sie erzeugenden Bewegungen kompakter Binärsysteme, wie Paare von *Schwarzen Löchern* oder Neutronensternen, sind deshalb Ziel zahlreicher Langzeitsimulationen und Untersuchungen hinsichtlich chaotischen Verhaltens.

All diese Simulationen setzen zuverlässige Werkzeuge voraus. Numerische Methoden zur Lösung der Bewegungsgleichungen sollten schnell und genau sein, Chaosindikatoren auch in Zusammenarbeit mit den numerischen Integratoren verlässliche Ergebnisse liefern.

Ziel dieser Arbeit ist die Entwicklung und Bereitstellung eben solcher Werkzeuge. Aus diesem Grunde werden zunächst die gängigsten Chaosindikatoren aus dem Bereich der Allgemeinen Relativität zusammengestellt und anhand erster einfacher Testbeispiele der klassischen Mechanik illustriert.

Im Anschluss hieran werden dann neue strukturerhaltende Integrationsmethoden für die beiden Formalismen der Binärsysteme, die *geodätischen Gleichungen* und die *post-Newton'sche* Beschreibung, vorgestellt. Wir werden sehen, dass der geodätische Ansatz zu Bewegungsgleichungen führt, deren numerische Lösung spezieller Schrittweitensteuerungen bedarf. Da die bisher bekannten Steuerungen an diesen Gleichungen scheitern, entwickeln wir einen neuen Algorithmus. Numerische Tests verdeutlichen den dadurch erzielten großen Gewinn an Genauigkeit und Effizienz.

Im Bereich der post-Newton'schen Bewegungsgleichungen werden wir zeigen, dass das entsprechende Hamiltonsystem einem gestörten Keplerproblem entspricht. Dies würde den Einsatz von Splitting-Verfahren motivieren. Wir werden allerdings sehen, dass es andere, weitaus schnellere Möglichkeiten der strukturerhaltenden Integration gibt. In umfangreichen numerischen Experimenten entpuppen sich diese als große Verbesserung im Vergleich zu den bisher bekannten Algorithmen.

Mithilfe der hier präsentierten Werkzeuge lassen sich zuverlässige Simulationen in effizienter Weise durchführen, wobei die Erhaltungsgrößen der Bewegung keiner numerischen Korrektur unterliegen. Damit hoffen wir, einen Beitrag zur weiteren Untersuchung der Gravitationswellen geleistet zu haben.

**To my parents.
For all their love and support!**

Contents

1. Introduction	9
1.1. The search for gravitational waves	9
1.2. Outline	10
2. Analysing common chaos indicators	13
2.1. The Hénon-Heiles model	13
2.2. Poincaré sections	14
2.2.1. Calculation of Poincaré sections	14
2.2.2. Impact on the sections by numerical schemes	16
2.3. Power spectra	18
2.4. Lyapunov exponents	19
2.4.1. Maximum Lyapunov exponent: The variational method	20
2.4.2. A bit offside the main topic: Calculation of all Lyapunov exponents	21
2.4.3. LE: The two-particle approach	23
2.5. Fast Lyapunov Indicator (FLI)	24
3. Long-time integration of Extreme Mass Ratio Inspirals (EMRIs)	27
3.1. Notation	27
3.2. Geodesic equations of motion	29
3.3. Properties of the geodesic equations of motion	30
3.4. Gauss-Runge-Kutta methods	31
3.5. The need for an efficient step size algorithm	33
3.6. (Problems with) existing step size algorithms	34
3.7. IGEM: A variable step size integration scheme for geodesic equations of motion	37
3.8. Efficient implementation of an implicit Gauss-Runge-Kutta scheme	39
3.9. Our test case: The Manko, Sanabri-Gómez, Manko spacetime background	41
3.10. Numerical experiments for the MSM case	45
3.10.1. $\rho = \mathbf{30.7}$: Quasiperiodic motion	46
3.10.2. $\rho = \mathbf{1.7}$: Non-chaotic but ill-mannered sort of motion	48
3.10.3. $\rho = \mathbf{0.7}$: Chaotic motion	52
4. Long-time integration of post-Newtonian equations of motion	59
4.1. The post-Newtonian formalism	59
4.2. The post-Newtonian equations of motion	63
4.3. Numerical properties of the PN equations of motion	64
4.4. Poisson integrator for post-Newtonian equations	65
4.5. Transformation to symplectic form	67
4.6. Structure preserving integrators for post-Newtonian equations of motion	69
4.7. Calculating the ‘exact’ Kepler-flow	71
4.8. Numerical experiments	74
4.8.1. The test cases	75
4.8.2. Comparing splitting methods I	77
4.8.3. Comparing splitting methods II	79
4.8.4. Comparing various integration methods	80
4.8.5. Comparing methods to calculate Poincaré sections	85

4.8.6. The two-particle method applied to the binary system	88
4.8.7. The frequency spectra	89
4.8.8. Systems with radiation	90
5. Summary	95
Acknowledgments	97
A.	99
B.	101
C.	104
D.	106
E.	107
References	109

1. Introduction

Supposedly motivated by an apple hitting his head, [Newton \(1687\)](#) contrived a theory of gravitation by which the gravitational force is inversely proportional to the square of the distance. This predicted the existence of Neptune but could not correctly describe the motion of the sun's nearest planet Mercury. Nevertheless, Newton's law hold on to its position as state-of-the-art theory until [Einstein \(1915\)](#) presented his field equations, thus giving life to general relativity. Not only was the new theory able to describe Mercury's motion but also predicted it new phenomena such as *black holes* and *gravitational waves*. These two are still, and presumably more than ever, subject to profound research.

1.1. The search for gravitational waves

Due to their non-linearity, the Einstein field equations are in no way easy to solve. Nevertheless, one particular solution was soon found by [Schwarzschild \(1916\)](#) which was the gateway to the description of black holes. These, in turn, are assumed to be the source of gravitational waves. With the aim to finally receive signals of such waves, much experimental effort has been put upon mounting land-based detectors. *Virgo* in France and Italy, *GEO 600* in Germany and the UK, and *LIGO* in the USA are only to name a few. They are soon to be joined by the space-based *eLISA*. In order to track any signal of gravitational waves, templates are required that give a hint on which needle to look for in the haystack of data delivered by all the working detectors.

To obtain such templates, one has to single out promising potential sources of gravitational waves and to calculate their motion in phase space. The main source of waves have been identified to be binary systems consisting of inspiraling compact objects, see ([Blanchet, 2002](#)) for details. Their mass proportions can be anything between equal masses and extreme ratios. Binaries with very unequal masses are called *Extreme Mass Ratio Inspirals* (EMRIs). One common example of an EMRI is a neutron star that orbits a super massive black hole (SMBH). EMRIs allow for a simple description as a free particle (the lighter one) moving in a curved spacetime given by the metric corresponding to the mass of the heavier particle. This approach is commonly known as the *geodesic motion*. Out of this, different templates for gravitational wave signals are obtained by applying various possible shapes of spacetime backgrounds and then calculating the emitted waves. By examining which template fits best to the measured data, one can determine the model that delivers the most reliable description of the spacetime around a SMBH. One famous model is the uncharged axisymmetric *Kerr metric* ([Kerr and Schild, 1963](#)). Another model, proposed by [Manko et al. \(2000\)](#), is presented as a numerical test case in [3.9](#).

Binaries with a not so extreme mass ratio are suitably described by the *post-Newtonian formalism*. This approach was possible after [Arnowitt et al. \(1962\)](#) discovered that Einstein's theory can be formulated as a Hamiltonian System. The idea is then to expand the elements of the metric tensor and the equations of motion of the matter in powers of the small parameter $1/c^2$. This gives the Hamiltonian as a power series in the small parameter, the first term of the series being the Hamiltonian for Newton's law of gravitation. The determination of the individual terms in this expansion is subject to current research in theoretical physics. [Jaranowski and Schäfer \(2001\)](#) have been able to determine the Hamiltonian up to third order

in $1/c^2$. The post-Newtonian approach has even been extended to a binary which is perturbed by a much lighter third body (Galaviz and Brügmann, 2011).

A property of relativistic test-particles which is not known from classical mechanics is their spin. After the foundation for the treatment of this spin had been laid down by Papapetrou (1951), the post-Newtonian formalism could be expanded to include the corresponding contributions, e.g., (Damour and Schafer, 1988). With this extension, the Hamiltonian system becomes a so called *Poisson system*. How to add spin contributions to the geodesic motion is not quite clear so far but will surely be resolved in the future.

This told, both approximations of a compact binary can be represented by a Hamiltonian. But each can give rise to non-integrable systems. As a consequence, the motion described by them can exhibit chaotic properties. If the motion of a particular binary is chaotic, the gravitational waves emitted during its inspiral will be unpredictable, thus leaving the researchers at the various wave detectors without any useful template. Hence, the investigation for chaos of a given binary system is a very important task. To conduct this search, one needs reliable indicators and numerical simulations over very long time spans. Numerical long-term analysis requires efficient and highly accurate integration schemes which behave well even during long-time simulations. To this aim one can take use of the special structure of the two approximations.

Over the last decades, many numerical analysts have been busy with developing tools for the long-term integration of equations of motion. As a result, the numerical analysis community came up with structure preserving algorithms such as *symplectic* schemes for Hamiltonian systems or *symmetric* integrators for time-reversible systems. Regarding long-time behaviour and conservation properties, these schemes are superior to ordinary numerical integrators in many applications of classical mechanics and astronomy. Whereas for standard integration schemes the overall error is normally proportional to the square of the length of the integration interval t_i , it only increases linearly with t_i for structure preserving integrators. And whereas there is a drift in constants of motions for standard methods, these constants are conserved up to a vanishingly small error for symplectic algorithms. These algorithms have been successfully applied even in quantum mechanics. A comprehensive presentation of such methods is given by Hairer *et al.* (2006). Recently, structure preserving algorithms for the post-Newtonian equations of motion have been introduced. Lubich *et al.* (2010) found a non-canonically symplectic integrator that preserves the Poisson structure of the system. Wu and Xie (2010) carried out a transformation of the system to symplectic form (which is always possible as is shown by the *Darboux-Lie theorem*) to which a symplectic algorithm can then be applied.

In view of these developments, this work is meant to provide numerical tools for the gravitational wave community in their simulations of binary systems. Therefore, we invent a structure preserving algorithm for EMRIs and dig deeper into the field of structure preserving algorithms for post-Newtonian equations of motion. In particular, we want to find out what impact a given numerical integrator has on the common indicators of chaos. In order to make this work readable for both physicists and numerical analysts, it is written in a self-contained way. The basic concepts and inputs of either field are explained in detail.

1.2. Outline

We start with introducing in chapter 2 the indicators of chaos which are used hereinafter. We explain how the respective indicators can be calculated numerically. Then, we carry out a first analysis of the different effects on the indicators by different integration schemes. We illustrate this with the help of a simple example.

In the following part 3, we first analyse some special aspects of the geodesic equations of motion. We will see that these aspects put some obstacles in the way of standard algorithms. Therefore, we develop an efficient structure preserving algorithm for geodesic equations of motion and test it against standard explicit Runge-Kutta schemes and standard structure preserving algorithms of classical celestial mechanics. We will observe that the new integrator beats its competitors in categories such as speed and accuracy. Besides, the new scheme is more suitable to calculate chaos indicators such as Poincaré sections.

Chapter 4 deals with the post-Newtonian approximation. Based on the transformation of the Hamiltonian to canonical form, various integration schemes are constructed. We analyse in detail which possibilities exist to enhance the performance of the integration. We then test structure preserving algorithms based on the transformation to canonical form and the Poisson-integrators according to Lubich *et al.* (2010) for efficiency and accuracy against standard explicit integration schemes. We will observe that, though the structure preserving algorithms fare better than the explicit integrators, there are significant differences between the individual schemes. The better ones will turn out to outperform the explicit competitors even in simulations with non-conservative radiation effects.

Finally, we can summarize our results in section 5.

All simulations for this work were run on a Core 2 Duo E6600 machine with 2.4GHz and 4GB RAM. The codes for the simulations have been written in *fortran* (simulations for chapter 3) and *c++* (simulations for chapters 2, 4).

2. Analysing common chaos indicators

If a Hamiltonian system in a $2N$ -dimensional phase space possesses N integrals of motion whose gradients are independent at every point of the phase space, its motion is regular. More specifically, under mild additional assumptions one can transform the system to *action-angle variables* such that the angle variables evolve on an invariant N -dimensional torus. Many systems, among them most examples of binary systems of compact objects, lack this nice property. As a consequence, these systems' motion can be chaotic. We have already discussed above that it is very important for the gravitational wave community to know whether a given system exhibits chaotic traits or not. For this, tools are necessary which allow for the distinction between regular and chaotic motions. Thus, in the present chapter, we examine the most frequently used chaos indicators and analyse which effects different kinds of numerical integrators can have on these. Plainly spoken, we want to get used to the peculiarities of the chaos indicators before applying them to relativistic binary systems in the following parts of this work. In particular, small numerical experiments by [Hairer *et al.* \(2006\)](#) suggest that standard integration schemes can lead to wrong conclusions with regard to the chaoticity of a dynamical system. We will check this for an easy classical example of a non-integrable system. This also gives us the opportunity to demonstrate the properties of the respective indicators of chaos. Let us now introduce our small classical example.

2.1. The Hénon-Heiles model

With the aim to model stellar motion, [Henon and Heiles \(1964\)](#) came up with the two-dimensional Hamiltonian

$$H(\mathbf{p}, \mathbf{x}) = \frac{1}{2} (\|\mathbf{p}\|^2 + \|\mathbf{x}\|^2) + x^2 y - \frac{1}{3} y^3, \quad (2.1)$$

where, for convenience, we assume the mass to be $m = 1$. Countless numerical investigations such as the one by [Benettin *et al.* \(1976\)](#) have shown that the motion in the 'funnel-shaped' potential is regular for energies $E < 0.11$. For energies $0.11 < E < 1/6$ however, the motion can be either regular or chaotic, depending on the region of the phase space the initial conditions are chosen from. To visualize the different kinds of motion, we plot the trajectory of a regular orbit along with a chaotic one in [Fig. 2.1](#). We will use exactly these two orbits to illustrate the behaviour of the chaos indicators below. For the regular orbit we choose the initial conditions

$$x_{\text{reg}} = y_{\text{reg}} = p_{y_{\text{reg}}} = 0, \quad p_{x_{\text{reg}}} = \frac{1}{2}, \quad (2.2)$$

whereas the chaotic example is given by the initial values

$$x_{\text{chaos}} = p_{y_{\text{chaos}}} = 0, \quad y_{\text{chaos}} = -0.1, \quad p_{x_{\text{chaos}}} = \sqrt{\frac{359}{1500}}. \quad (2.3)$$

Both orbits have the same energy $H = 1/8$. In order to obtain the plots in [figure 2.1](#), an $s = 4$ -stage Gauss Runge-Kutta scheme with a step size $h = 0.001$ was used. Throughout the rest of this chapter, this integration scheme is considered to be the 'exact' solution. Detailed information on Gauss-Runge-Kutta schemes is given in [section 3.4](#) below. We now turn our attention towards the indicators of chaos.

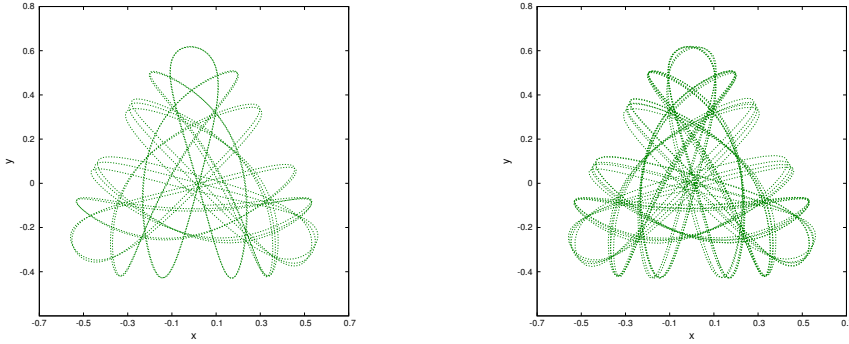


Figure 2.1: Motion in the Hénon-Heiles potential: For the energy $H = 1/8$, the trajectory in the configuration space of a regular orbit with initial conditions $x = y = p_y = 0$, $p_x = \frac{1}{2}$ is plotted in the left panel. The right panel shows a chaotic orbit with initial conditions $x = p_y = 0$, $x = -0.1$, $p_x = \sqrt{\frac{359}{1500}}$.

2.2. Poincaré sections

For a Hamiltonian with two degrees of freedom, the motion is restricted to a three-dimensional submanifold due to the energy conservation. One can then fix a given surface in the phase space and for every time the trajectory intersects with this surface, plot two of the remaining three coordinates against each other. This gives an unambiguous representation of the orbit as the third variable is uniquely determined by the constraint $H = \text{const}$. A discussion of the properties of these so called *Poincaré sections* is not the purpose of this work. We refer the interested reader to a detailed introduction by [Meiss \(1992\)](#). But we note that Poincaré sections are the most reliable tool to distinguish different kinds of orbits in a four-dimensional phase space. We illustrate this by plotting in [Fig. 2.2](#) the Poincaré sections for the two different orbits in the Hénon-Heiles potential of [section 2.1](#). As in the rest of this section, we plot y against p_y for every intersection at $x = 0$ in the time interval $t \in [0, 10^6]$. For the chaotic motion the points seem to be randomly scattered over the subspace whereas they lie on a curve for the other orbit with initial conditions [\(2.2\)](#). Because of this property, the orbit is classified as *quasiperiodic*. We see that the Poincaré sections are an efficient tool for the geodesic trajectory in an EMRI when the spacetime is axisymmetric, for in this case the phase space consists of four dimensions. But how to best compute the sections?

2.2.1. Calculation of Poincaré sections

Without loss of generality, we consider sections of the $x = 0$ -plane. Once having passed this plane during a step $\mathbf{y}_n \rightarrow \mathbf{y}_{n+1}$, then, no matter what the order of the numerical scheme, the section is located with an accuracy of h as this is the difference in time between the consecutive steps. There are various possibilities to improve the accuracy with which the sections are determined:

- One can drastically reduce the length of the steps. If the section is to be located up to an error proportional to the numerical integration error $\mathcal{O}(h^p)$, the step size can be reduced by p orders of size. Such an algorithm is described by the following lines of pseudo code:

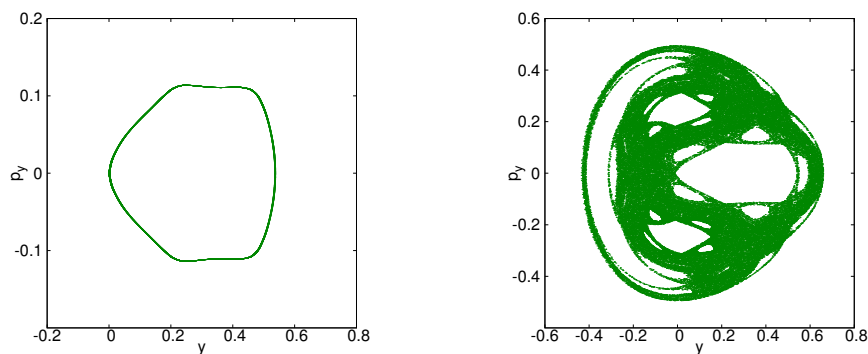


Figure 2.2: Poincaré sections at $x = 0$ for the orbits of Fig. 2.1 calculated with the ‘exact’ solution. The left panel shows the regular case (2.2) and the right panel depicts sections of the chaotic orbit (2.3).

```

1         calculate  $\mathbf{y}_{n+1} = \Phi_{h_{\text{step}}}(\mathbf{y}_n)$ ;
2         if  $x_{n+1} \cdot x_n < 0$  then
3             if  $h_{\text{step}} \leq h^p$  then
4                 set  $\mathbf{y}_{\text{sect}} = \frac{1}{2}(\mathbf{y}_{n+1} + \mathbf{y}_n)$ ;
5                  $h_{\text{step}} = h$ ;
6             else
7                  $h_{\text{step}} = \frac{h_{\text{step}}}{2}$ ;
8                 go back to line 1;
9             fi
10        fi

```

As the numerical solution stays $\mathcal{O}(h^p)$ close to the analytical one and the location of the section is encircled up to a distance of h_{step} , the error between the analytical and the numerical value of the section is

$$\|\mathbf{y}_{\text{sect,an}} - \mathbf{y}_{\text{sect,num}}\| = \mathcal{O}(h^p) + \mathcal{O}(h_{\text{step}}). \quad (2.4)$$

From this we see that $h_{\text{step}} < h^p$ does not make sense. But we notice, that this procedure can be expensive. Even more so when the equations of motion are very costly to calculate as will be the case for the binary systems we consider in the following chapters. Therefore, another method to calculate the sections is necessary.

- If the desired accuracy for the sections is $\mathcal{O}(h^{\tilde{p}})$, one can calculate an interpolation polynomial $\mathbf{U}(t)$ through the points $(\mathbf{y}_{n+\tilde{p}/2}, \dots, \mathbf{y}_{n+1}, \mathbf{y}_n, \dots, \mathbf{y}_{n-\tilde{p}/2})$ via

$$\mathbf{U}(t) = \sum_{i=-\tilde{p}/2}^{\tilde{p}/2} \mathbf{y}_{n+i} \cdot l_i(t), \quad (2.5)$$

where $l_i(t)$ is the Lagrange polynomial, cf. section 3.4. Here, we assumed \tilde{p} to be even, but we can proceed in a similar way for odd \tilde{p} . One can then search for the root of the polynomial’s x -component with the help of a fast *bisection method*. If we replaced the interpolation points with the exact solution at the same time, $\mathbf{y}_{\text{an}}(t)$, we would have

$$\max_{t \in I} \|\mathbf{y}_{\text{an}}(t) - \mathbf{U}(t)\| = \mathcal{O}(h^{\tilde{p}}) \quad (2.6)$$

all over the interpolation interval I . As the interpolation points are an approximation to the exact solution with an error $\mathcal{O}(h^p)$, we have instead

$$\max_{t \in I} \|\mathbf{y}_{\text{an}}(t) - \mathbf{U}(t)\| = \mathcal{O}(h^{\tilde{p}}) + \mathcal{O}(h^p). \quad (2.7)$$

Keeping this in mind, if we locate the root of the polynomial up to a very small error ε , the error in the numerical calculation of the Poincaré section will be

$$\|\mathbf{y}_{\text{sect,an}} - \mathbf{y}_{\text{sect,num}}\| = \mathcal{O}(h^p) + \mathcal{O}(h^{\tilde{p}}) + \mathcal{O}(\varepsilon). \quad (2.8)$$

- If the underlying integrator is a Gauss collocation scheme, the messy book-keeping for the interpolation in the algorithm above can be circumvented. One can conveniently use the collocation property, i.e., the fact that an s -stage Gauss-Runge-Kutta scheme is equivalent to a interpolation polynomial through the points $(0, \mathbf{y}_n)$ and $(c_1, \mathbf{Y}_1), \dots, (c_s, \mathbf{Y}_s)$, see also 3.4. Numerical analysis shows, e.g., (Hairer *et al.*, 1993), that the interpolation polynomial stays $\mathcal{O}(h^s)$ close to the analytical solution within the whole interval between \mathbf{y}_n and \mathbf{y}_{n+1} . Thus, proceeding as in the algorithm before, we efficiently find an approximation $\mathcal{O}(h^s)$ close to the real section. The Poincaré sections of Fig. 2.2 were calculated in this very way.

For efficiency's sake, we always use the interpolation method in the rest of this work. When the underlying integrator is a Gauss collocation scheme, we use the more convenient interpolation via the collocation polynomial.

2.2.2. Impact on the sections by numerical schemes

Hairer *et al.* (2006) employed an explicit Euler scheme

$$\mathbf{y}_{n+1} = \mathbf{y}_n + hf(\mathbf{y}_n) \quad (2.9)$$

with the very small step size $h = 10^{-5}$ to propagate a regular orbit in the Hénon-Heiles potential and found out that the corresponding Poincaré sections looked rather chaotic. This led to the assumption that ‘explicit schemes turn order into chaos’. When we repeat the experiment for our regular initial data (2.2) and track the relative error in the energy

$$\Delta H = \frac{H(\mathbf{y}_n) - H(\mathbf{y}_0)}{H(\mathbf{y}_0)}, \quad (2.10)$$

we observe that it increases to $\Delta H = 0.27$ at $t = 25000$. It is well known that for higher energies a previously regular part of the phase space can become chaotic. The question is thus if the ‘chaoticity-enhancing’ property of explicit schemes is purely a consequence of them increasing the energy or if there is something more behind it. In order to tackle this question, we again consider the system with initial conditions (2.2) for the time interval $t \in [0, 10^6]$. We apply the classical 4th order Runge-Kutta scheme (RK4)

$$\mathbf{y}_{n+1} = \mathbf{y}_n + \sum_{i=1}^s b_i f(\mathbf{Y}_i), \quad (2.11)$$

$$\mathbf{Y}_i = \mathbf{y}_n + \sum_{j=1}^{i-1} a_{ij} f(\mathbf{Y}_j), \quad (2.12)$$

given by

$$\begin{aligned} b_1 = b_4 &= \frac{1}{6}, & b_2 = b_3 &= \frac{1}{3}, \\ a_{21} = a_{32} &= \frac{1}{2}, & a_{43} &= 1, \\ a_{20} = a_{30} = a_{31} &= 0, \end{aligned} \tag{2.13}$$

with a step size $h = 0.01$ and compare the results with the ones obtained by the symplectic 2nd order *Stoermer-Verlet* scheme

$$\tilde{\mathbf{p}} = \mathbf{p}_n - \frac{h}{2} \nabla_{\mathbf{x}} H(\mathbf{x}_n, \mathbf{p}_n) \tag{2.14}$$

$$\mathbf{x}_{n+1} = \mathbf{x}_n + h \nabla_{\mathbf{p}} H(\mathbf{x}_n, \tilde{\mathbf{p}}) \tag{2.15}$$

$$\mathbf{p}_{n+1} = \tilde{\mathbf{p}} - \frac{h}{2} \nabla_{\mathbf{x}} H(\mathbf{x}_{n+1}, \tilde{\mathbf{p}}). \tag{2.16}$$

In Fig. 2.3 we observe that the RK4 scheme yields a smaller energy error ΔH than the structure preserving algorithm. Under these circumstances, there is no difference in the Poincaré sections between the explicit scheme and the structure preserving method or the ‘exact’ solution, respectively, as we can see in Fig. 2.4. The number of sections (157220) is the same, too. Hence, there seems to be no hidden ‘chaoticity-enhancing’ property in explicit schemes.

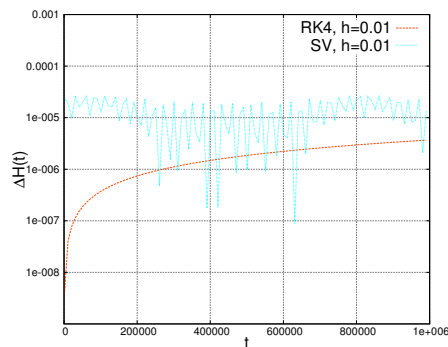


Figure 2.3: Relative error of the Hamiltonian ΔH as a function of time $t \in [0, 10^6]$ for a structure preserving algorithm and the explicit RK4 scheme for the Hénon-Heiles potential with regular initial values.

[Katsanikas and Patsis \(2011\)](#) expanded the Poincaré sections to three-dimensional potentials. At every intersection they plot four remaining coordinates using a three-dimensional plot plus color. Although doing so would exceed all means of illustration, one can in theory expand this tool further to arbitrary dimension, for example by two-dimensional plots for every tuple of coordinates. With this technique, even in the 3D potential case, one cannot satisfactorily distinguish between different kinds of regular motion, ([Katsanikas and Patsis, 2011](#)). But one can still separate regular motion and chaos. Yet, this will result ever more cumbersome with each additional dimension. As we will see below, the interesting system of a binary with spins yields a 10-dimensional phase space. This is why other chaos indicators have been proposed.

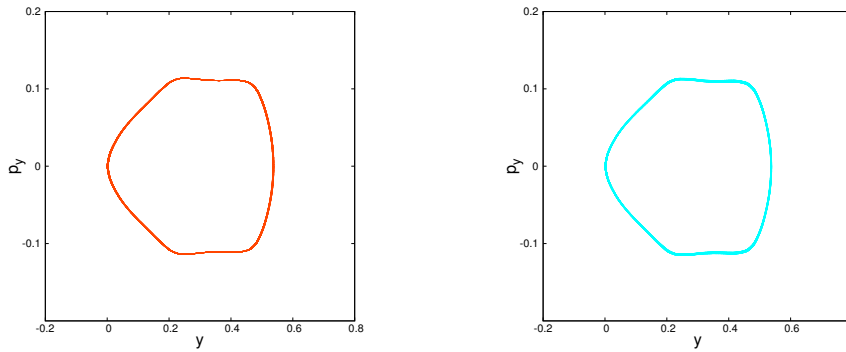


Figure 2.4: Poincaré sections at $x = 0$ for the regular orbit (2.2) calculated with the classical Runge-Kutta scheme, $h = 0.01$ (left panel) and with the Störmer-Verlet method, $h = 0.01$ (right panel).

2.3. Power spectra

Faced with the problem of a high-dimensional phase space as he wanted to examine the solar system, [Laskar \(1990\)](#) focused on the system's frequencies and gave rise to a new method: One can track an arbitrary component of the solution, y^j , over a given time span I and calculate the spectrum of frequencies

$$|f(\omega)^j| = \left| \int_I e^{i\omega t} y^j(t) dt \right|. \quad (2.17)$$

The implementation of the Fourier transform depends on the integrator. If a constant step size scheme is used, one can divide I into 2^k , $k \in \mathbb{N}$ parts. Then a fast Fourier transform (FFT) can be applied to the resulting values $(\mathbf{y}_1, \dots, \mathbf{y}_{2^k})$. If the equations of motion are solved by a variable step size algorithm instead, one can use a suitable interpolation in order to obtain values \mathbf{y}_n , $n = 1, \dots, 2^k$ which all have the same distance in time. To circumvent the book-keeping which is coming along with the interpolation, one can also use any convenient quadrature such as the trapezoidal rule on the non-constant time intervals. This, of course, needs more operations than the FFT does.

For a regular motion, the system can be expressed by action-angle variables. The action variables are first integrals and the angle variables change periodically with time. As a consequence, the coordinates y^j , which can be regarded as functions of the action-angle variables, are also (quasi)periodic. Therefore, their frequency spectrum will either consist of one frequency or be the superposition of a few frequencies. In the case of a chaotic system, the motion is irregular and the spectrum is continuous. We demonstrate the difference in the spectra by plotting the frequency spectrum of x in the time intervals $t \in [0, 15000]$ and $t \in [10^6 - 15000, 10^6]$ for the regular and the chaotic orbit of section 2.1. The result is shown in Fig. 2.5. We see that the regular orbit is a superposition of few frequencies whereas the spectrum for the chaotic orbit is showing noise. Furthermore, a regular orbit's frequencies do not change during the integration but a chaotic one's can.

We now consider an integration interval $t \in [0, 30000]$ and apply the explicit Euler scheme (2.9) with $h = 10^{-5}$ to the regular test orbit. We calculate the frequency once in the interval

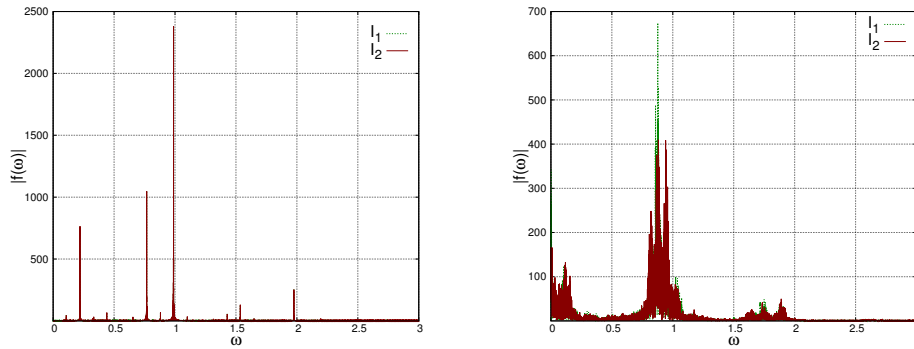


Figure 2.5: For the time intervals $I_1 = [0, 15000]$ and $I_2 = [10^6 - 15000, 10^6]$, the Fourier spectrum of x , $|f(\omega)| = \left| \int_I e^{i\omega t} x(t) dt \right|$ is plotted. The left panel corresponds to the regular orbit (2.2), the right panel shows the spectrum of the chaotic orbit (2.3).

$I_1 = [0, 1500]$ and once for $I_2 = [28500, 30000]$, s. the left panel of Fig. 2.6. This again illustrates how an inexact integrator can turn regular motion into chaos. Calculating the regular orbit's frequency spectrum for $I_1 = [0, 15000]$ and $I_2 = [10^6 - 15000, 10^6]$ with the RK4 scheme of the previous section 2.2.2, we can demonstrate once more that the 'chaos-enhancing' is only due to the Euler method's bad performance and not a consequence of explicitness by itself.

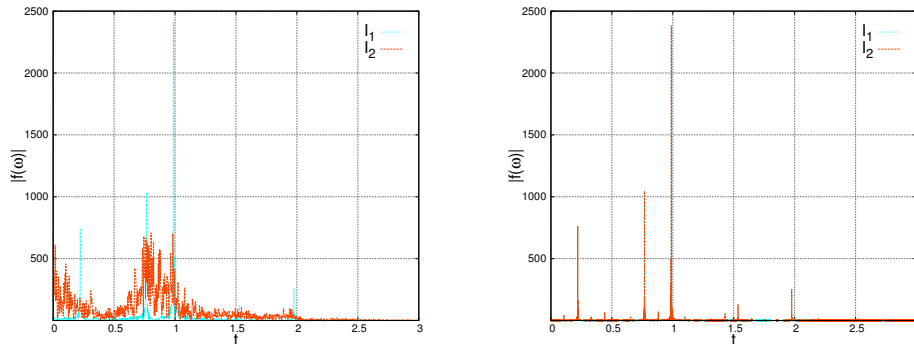


Figure 2.6: For our regular test orbit in the Hénon-Heiles potential, the left panel shows the frequency spectrum of the x component in the intervals $I_1 = [0, 1500]$ and $I_2 = [28500, 30000]$ obtained with an explicit Euler scheme. In the right panel, an RK4 scheme was applied to calculate the frequency spectrum in the intervals $I_1 = [0, 15000]$ and $I_2 = [10^6 - 15000, 10^6]$.

2.4. Lyapunov exponents

Let us ask the following question: What will happen to the solution $\mathbf{y}(t)$ of the differential equation

$$\frac{d\mathbf{y}}{dt} = f(\mathbf{y}), \quad (2.18)$$

$$\mathbf{y}(0) = \mathbf{y}_0 \tag{2.19}$$

if we change the initial value \mathbf{y}_0 , i.e., how does $\partial_i \mathbf{y}(t)$ depend on $\partial_i \mathbf{y}_0$? Obviously, a small change in the initial condition would yield an only slightly different trajectory $\mathbf{y}(t)$ for a regular orbit whereas for a chaotic, unpredictable one, the outcome could be completely different. This observation leads us to another tool to measure chaoticity.

2.4.1. Maximum Lyapunov exponent: The variational method

Deriving both sides of the differential equation (2.18) yields the *variational equation*

$$\frac{d(\partial_i \mathbf{y}(t))}{dt} = [(Df)(\mathbf{y})] \partial_i \mathbf{y}(t), \tag{2.20}$$

$$\partial_i \mathbf{y}(0) = \hat{\mathbf{e}}_i \tag{2.21}$$

which describes how a perturbation in \mathbf{y}_0 propagates in time. If $\tilde{\varphi}(\mathbf{a}_0)$ is the solution of this variational equation for an initial condition \mathbf{a}_0 , then

$$\lambda(\mathbf{a}_0) = \lim_{t \rightarrow \infty} \frac{1}{t} \frac{\log \|\tilde{\varphi}(\mathbf{a}_0)\|}{\|\mathbf{a}_0\|} \tag{2.22}$$

exists for all \mathbf{a}_0 . When one chooses a basis $\{\mathbf{a}_i\}$ of the phase space such that

$$\sum_i \lambda(\mathbf{a}_i) \leq \sum_i \lambda(\tilde{\mathbf{a}}_i) \tag{2.23}$$

for every other basis $\{\tilde{\mathbf{a}}_i\}$, then the numbers

$$\lambda_i := \lambda(\mathbf{a}_i) \tag{2.24}$$

are called the *Lyapunov exponents* of the system (2.18). We remark here that the exponents depend on the initial position in the phase space. The maximum exponent

$$\lambda := \max_i \lambda_i \tag{2.25}$$

is of particular interest. For a regular system, λ is equal to zero. For chaotic motion, λ tends to a finite value. For each vector \mathbf{v} with non-vanishing component in the direction \mathbf{a}_{\max} corresponding to the maximum exponent, we have

$$\lambda(\mathbf{v}) = \lambda. \tag{2.26}$$

Therefore, when calculating the solution of the variational equation

$$\frac{d\mathbf{v}}{dt} = [(Df)(\mathbf{y})] \mathbf{v} \tag{2.27}$$

for an arbitrary $\mathbf{v}(0)$, we have with a probability of one that

$$\lambda = \lim_{t \rightarrow \infty} \frac{1}{t} \frac{\log \|\tilde{\varphi}(\mathbf{v}(0))\|}{\|\mathbf{v}(0)\|}. \tag{2.28}$$

This is the *variational method* to calculate the maximum Lyapunov exponent (LE) as an indicator of chaos. The definition of the LE (2.28) requires the solution of a variational equation. In relativistic systems, such as ours in the following chapters, it is often very cumbersome to derive such an equation. Furthermore, for high-dimensional systems, the (structure preserving) solution of equation (2.27) is very expensive. Thus, another method to calculate the LE is normally used by the general relativity community. This will be presented in the next but one subsection. Before, we deviate a bit from our actual topic, the distinction between chaos and order, and discuss how to calculate all Lyapunov exponents λ_i in the next subsection.

2.4.2. A bit offside the main topic: Calculation of all Lyapunov exponents

In order to calculate all λ_i , one could in theory solve the matrix-valued differential equation

$$\frac{dY}{dt} = [(Df)(\mathbf{y}(t))] Y(t), \quad (2.29)$$

$$Y(0) = (\mathbf{a}_1, \dots, \mathbf{a}_N) \quad (2.30)$$

for the initially orthogonal basis \mathbf{a}_i of the N -dimensional phase space. Unfortunately, round-off errors will cause every column of $Y(t)$ to get a small component in the direction corresponding to the maximum exponent. As a consequence, for integrations over very long times, the columns of the matrix get aligned causing all λ_i to equal λ in the end. To avoid this, one has to re-orthogonalize the vectors from time to time. [Benettin et al. \(1978\)](#) proposed two algorithms to cope with this challenge. Both are based on the QR-decomposition of a matrix,

$$Y = QR, \quad (2.31)$$

where Q is orthogonal and R is an upper tridiagonal matrix. It is well known from numerical analysis that every matrix can be decomposed in such a way. The decomposition (2.31) can be conveniently solved by efficient standard algorithms, s., e.g., ([Flannery et al., 1992](#)). This said, the Lyapunov exponents can be calculated as follows:

- In the *discrete QR algorithm*, the integration interval I is divided into smaller intervals $I = I_0 \cup \dots \cup I_j \cup \dots$, $I_j = [t_j, t_{j+1}]$. Then, one sets

$$Y(0) = Q(0) = I \quad (2.32)$$

and solves for every small interval I_j :

$$\frac{dY_j}{dt} = [Df(y(t))] Y_j, \quad (2.33)$$

$$Y_j(t_j) = Q_j, \quad (2.34)$$

$$Y_j(t_{j+1}) = Q_{j+1} R_{j+1}. \quad (2.35)$$

Here, the QR-decomposition is applied at the end of each interval in step (2.35). One can then show that the Lyapunov exponents are given as

$$\lambda_i = \lim_{j \rightarrow \infty} \frac{\log \|(R_j)_{ii} \cdots (R_1)_{ii}\|}{t_j} \quad (2.36)$$

-
- The *continuous QR algorithm* uses the ansatz $Y(t) = Q(t)R(t)$ to derive a differential equation for the orthogonal QR-part Q which reads

$$\frac{dQ}{dt} = QA(Q, \mathbf{y}), \quad (2.37)$$

$$A(Q, \mathbf{y})_{ij} = \begin{cases} (Q^T [(Df)(\mathbf{y})] Q)_{ij}, & i > j, \\ 0, & i = j, \\ -(Q^T [(Df)(\mathbf{y})] Q)_{ji}, & i < j. \end{cases} \quad (2.38)$$

This implies the differential equation for diagonal entries of the upper-triangular part

$$\frac{dR_{ii}}{dt} = (Q^T [(Df)(\mathbf{y})] Q)_{ii} R_{ii}. \quad (2.39)$$

[Dieci et al. \(1997\)](#) show that in this case, the i -th Lyapunov exponent is given as

$$\lambda_i = \lim_{t \rightarrow \infty} \frac{\log R_{ii}(t)}{t} = \lim_{t \rightarrow \infty} \frac{1}{t} \int_0^t (Q^T [(Df)(\mathbf{y})] Q)_{ii} dt. \quad (2.40)$$

We now want to illustrate the two methods. Therefore, we apply them to our chaotic test orbit in the Hénon-Heiles potential (2.3). For the discrete QR algorithm, we use the RK4 method with a step size $h = 0.01$ to solve the variational equation along with the differential equation for the system (2.18). In order to avoid an overflow, we have to apply the QR-decomposition every 10 time units. In the case of the continuous QR algorithm, we have to guarantee that $Q(t)$ stays orthonormal during the integration. If we used the RK4 scheme for this algorithm, we would have to project the numerical solution Q_n after each time-step. The projection \mathcal{P} of a matrix onto the manifold of orthonormal matrices is given by, e.g., ([Hairer et al., 2006](#)),

$$\mathcal{P}Q_n = UV^T, \quad (2.41)$$

where U and V are the orthogonal matrices of the singular value composition

$$Q_n = U\Sigma V^T, \quad (2.42)$$

$$\Sigma = \text{diag}(\sigma_1, \dots, \sigma_N), \quad (2.43)$$

$$\sigma_1 \geq \dots \geq \sigma_N \geq 0. \quad (2.44)$$

The calculation of the singular value decomposition at each time step would lead to unsustainable computational cost. Therefore, we use an $s = 2$ -stage Gauss Runge-Kutta scheme with $h = 0.1$ to solve both the differential equation for the orbit and equation (2.37). The orthogonality of $Q(t)$ is a first integral,

$$Q(t)^T Q(t) = \mathcal{I} = \text{const}, \quad (2.45)$$

and thus conserved by Gauss-Runge-Kutta schemes, see ([Hairer et al., 2006](#)) for example. We then apply the trapezoidal rule to calculate the integral in (2.40). For both QR algorithms, we integrate until $t = 10^6$ in order to approach the limit in time. In Fig. 2.7 we give the results of our simulations. There, we can see how the exponents approach their limit as time is advancing. The plots also contain the ‘exact’ solution for the LE with the variational method.

Once more, the ‘exact’ solution is given by the Gauss-Runge-Kutta scheme with $s = 4$ and $h = 0.001$. We observe that the largest exponent as given by the QR methods converges towards the LE for large times. But we notice that the largest exponent of the continuous QR algorithm does not come as close towards the LE as the one of the discrete algorithm. With a step size $h = 0.1$, the trapezoidal rule cannot adequately approximate the integral in equation (2.40). To demonstrate this, we interpolated the solution between two time steps with a polynomial of order 4 (which is the same order as the integration scheme). This enabled us to divide each interval of the trapezoidal rule into 10 smaller ones. Doing so, the largest exponent given by the continuous QR algorithm was closer to the LE as before. Thus, the integral (2.40) and not the integration scheme was responsible for the bad approximation.

In order to illustrate the additional computational cost incurred by the need for all Lyapunov exponents, we compare in table 2.1 the computation time of the two simulations above with simulations where only the LE is calculated via the variational method (2.28) with the same two integrators and the same step sizes. It is obviously very expensive to calculate all the exponents. Let us now focus on our main topic again.

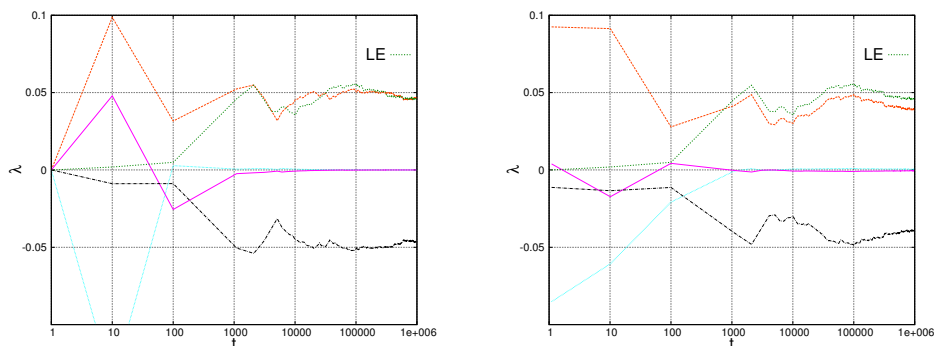


Figure 2.7: The evolution in time of the Lyapunov exponents λ_i once calculated with the discrete QR method (left panel) and once obtained via the continuous QR algorithm. Both panels also show the LE as a function of time.

Simulation	$T_{\text{calc}}[\text{s}]$
discrete QR	211.59
continuous QR	478.52
LE with RK4	34.57
LE with Gauss, $s = 2$	61.25

Table 2.1: The CPU calculation times for the QR algorithms are compared with the CPU times for the calculation of the LE.

2.4.3. LE: The two-particle approach

Although the variational method is much cheaper than the QR algorithms, it can still be very cumbersome, especially in relativistic simulations. To avoid this, one can resort to an idea

first introduced by [Benettin et al. \(1976\)](#):

To calculate the LE of a given orbit with initial conditions \mathbf{y}_0 , we consider a second trajectory $\tilde{\mathbf{y}}(t)$ with initial conditions very close to the actual orbit $\mathbf{y}(t)$. This is called the *two-particle method* or *shadow trajectory method*. One integrates both orbits simultaneously and tracks their distance in phase space

$$d(t) = \|\mathbf{y}(t) - \tilde{\mathbf{y}}(t)\|. \quad (2.46)$$

One can then obtain the maximum Lyapunov exponent as

$$\lambda = \lim_{t \rightarrow \infty} \frac{1}{t} \log \frac{d(t)}{d(0)}. \quad (2.47)$$

For Hamiltonian systems, the manifold defined by $H = \text{const}$ is usually bounded. Consequently, the maximal distance between an orbit and its shadow is bounded, too. Thus, one has to apply a renormalization to avoid that λ tends to zero due to the bounded distance. With a fixed threshold d smaller than the diameter of the manifold $H = \text{const}$, the two-particle method with renormalization is as follows:

```

1         function calculate_LE
2             initialize__y(0);
3             calculate__ytilde(0);
4             initialize__lambda = 0;
5             while ( $t < t_{\text{end}}$ ) do
6                 calculate__yn+1(yn,  $h$ );
7                 calculate__ytilden+1(ytilden,  $h$ );
8                 calculate__d( $t$ ) =  $\|\mathbf{y}_{n+1} - \tilde{\mathbf{y}}_{n+1}\|$ ;
9                 if ( $d(t) > d$ ) do
10                      $\lambda = \lambda + \frac{1}{t_{\text{end}}} \log \frac{d(t)}{d(0)}$ 
11                     reset__ytilden+1 =  $\mathbf{y}_{n+1} + \frac{d(0)}{d(t)}(\tilde{\mathbf{y}}_{n+1} - \mathbf{y}_{n+1})$ 
12                 fi
13             od
14         end

```

[Wu et al. \(2006\)](#) argued that the two-particle method should be preferred over the variational method in general relativistic simulations.

We compare the result of the two methods to calculate the LE in Fig. 2.8. For both the regular and the chaotic case, the LE as given by the shadow-trajectory approach converges towards the variational result and we see that either method leads to the same conclusion about chaoticity.

2.5. Fast Lyapunov Indicator (FLI)

In some cases one can abbreviate the calculations and get a first hint on the kind of motion by applying the *Fast Lyapunov Indicator* which was proposed by [Wu et al. \(2006\)](#). The idea is to omit the time-limit in the LE's definition (2.47) and track the function

$$\text{FLI}(t) = \log \frac{d(t)}{d(0)}. \quad (2.48)$$

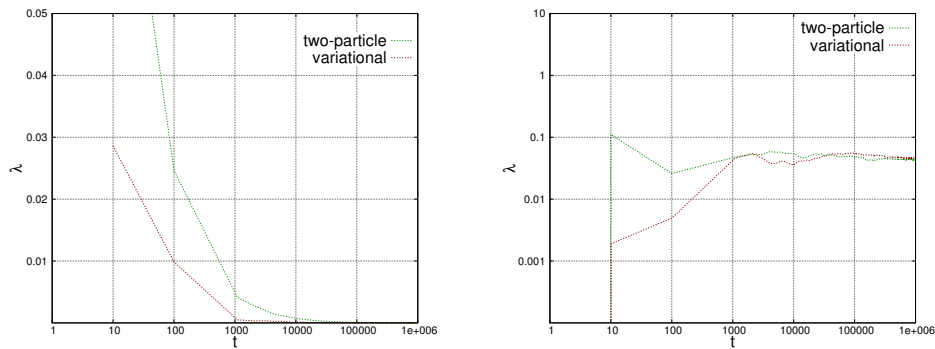


Figure 2.8: The evolution in time of LE calculated with the variational and the two-particle method. The left panel shows the result for the regular orbit (2.2). The LE for the chaotic case 2.2 is shown in the right panel in double logarithmic scale.

Put practically, FLI measures how fast two initially close orbits are diverging, thus separating order from chaos. The advantage of this method is that, in cases where it is applicable, it does not require a large time interval. Hence, one need not care about the long-time behaviour of the numerical integrator and can choose a fast scheme instead. We remark that in practical implementations, a renormalization as described in the previous section is necessary again.

As we have seen in the previous sections, the RK4 scheme with a step size of $h = 0.01$ shows a satisfactory behaviour for not too long integrations. We thus employ this scheme to track the FLI over the interval $t \in [0, 10^5]$. The results for our two test cases are given in Fig. 2.9. One observes that the indicator increases slowly with time for the regular orbit whereas it is growing linearly for chaotic motion. From Fig. 2.9 it becomes also clear that for too small time scales one cannot distinguish chaos from order as for $t < 10000$ the plot for the chaotic orbit resembles the one for the regular trajectory.

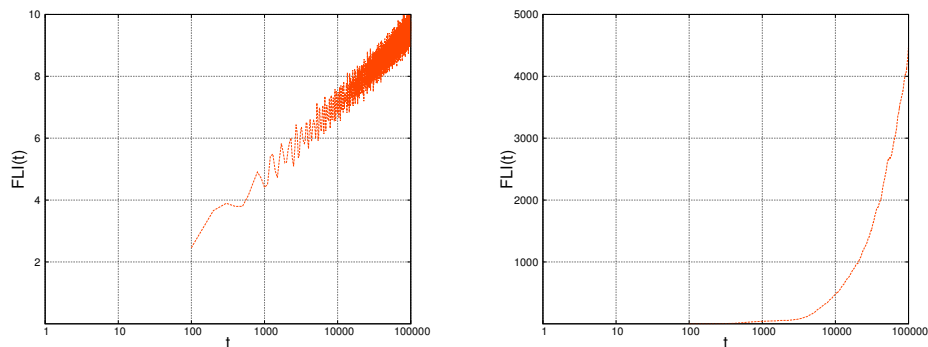


Figure 2.9: The Fast Lyapunov Indicator (FLI) against time for the regular orbit (2.2) (left panel) and the chaotic test case (2.3) (right panel) in semi-logarithmic scale.

Having introduced the useful tools of chaos analysis, we finally turn our attention towards binary systems.

3. Long-time integration of Extreme Mass Ratio Inspirals (EMRIs)

According to its name, an EMRI is a binary for which the mass of one object is much larger than the mass of the second. Without loss of generality we have $m_1 \gg m_2$. One can thus regard an EMRI as a system of a test particle moving in the stationary gravitational field of the much heavier mass –just as one can approximate the system earth-sun by regarding the position of the sun as fixed, with the earth moving around it. Given the equivalence of gravitation and curved space, a test particle in a gravitational field is regarded as a free particle moving in a non-Euclidean space described by a metric $g_{\mu\nu}$. A free particle that moves from a point x_a to a point x_b always does so minimizing the distance between these points. In a curved spacetime this paths are geodesics. Thus, the equations which describe the orbital motion of an EMRI's light mass around the much heavier one are called *geodesic equations of motion*. These will be derived as soon as we have introduced some notation in the following section.

3.1. Notation

Throughout the rest of this work, τ denotes proper time. A dot symbolizes derivation with regard to τ . In sections elaborating the physical background, we use the standard covariant and contravariant formalism which is common in relativity. Accordingly, greek letters stand for indices $\alpha = 1, 2, 3, 4$ and variables with greek subscript (superscript) denote covariant (contravariant) four-vectors. Variables with two indices denote tensors. Furthermore, we use Einstein's sum convention, i.e.,

$$g_{\mu\nu}x^\mu x^\nu = \sum_{\mu,\nu=1}^4 g_{\mu\nu}x^\mu x^\nu. \quad (3.1)$$

In the numerical analysis parts, we change the symbolism and use common notations from this field. Thus, h represents the length of a time-step. We distinguish between time and space and denote space-like vectors by bold variables. In particular, \mathbf{y} denotes a point in the phase space (which itself shall be called \mathcal{X})

$$\mathbf{y} = \begin{pmatrix} \mathbf{p} \\ \mathbf{x} \end{pmatrix}, \quad (3.2)$$

where \mathbf{p} and \mathbf{x} are canonical momenta and coordinates, respectively. In order to simplify the notation of the Hamilton equations

$$\dot{\mathbf{p}} = -\nabla_{\mathbf{x}}H \quad (3.3)$$

$$\dot{\mathbf{x}} = \nabla_{\mathbf{p}}H, \quad (3.4)$$

we introduce

- the unitary matrix \mathcal{I} which has half the same dimension of \mathcal{X} ,
- the symplecticity matrix

$$J := \begin{pmatrix} 0 & \mathcal{I} \\ -\mathcal{I} & 0 \end{pmatrix}, \quad (3.5)$$

- the phase space gradient

$$\nabla := \begin{pmatrix} \nabla_{\mathbf{p}} \\ \nabla_{\mathbf{x}} \end{pmatrix}, \quad (3.6)$$

- and the function

$$f(\mathbf{y}) := J^{-1} \nabla H(\mathbf{y}). \quad (3.7)$$

With this, the equations (3.3) and (3.4) are given in short form as

$$\frac{d\mathbf{y}}{d\tau} = f(\mathbf{y}). \quad (3.8)$$

We denote by φ_τ the flow corresponding to a system (3.8) with initial conditions \mathbf{y}_0 , i.e.,

$$\mathbf{y}(\tau) = \varphi_\tau(\mathbf{y}_0). \quad (3.9)$$

Φ_h is the numerical approximation to that flow over a time interval h .

When referring to a Runge-Kutta method, we make use of the following quantities:

- the number of inner stages s ,
- the inner stages c_1, \dots, c_s ,
- the weights at the inner stages, b_i and a_{ij} , respectively,
- the matrix

$$A := \begin{pmatrix} a_{11} & \dots & a_{1s} \\ \vdots & \ddots & \vdots \\ a_{s1} & \dots & a_{ss} \end{pmatrix}, \quad (3.10)$$

- the vector

$$\vec{y}_n := \left(\underbrace{\mathbf{y}_n, \dots, \mathbf{y}_n}_{s \text{ times}} \right)^T, \quad (3.11)$$

- the inner-stage values

$$\vec{Y} := (\mathbf{Y}_1, \dots, \mathbf{Y}_s)^T, \quad (3.12)$$

- the auxiliary variables

$$\vec{Z} := (\mathbf{Z}_1, \dots, \mathbf{Z}_s)^T = \vec{Y} - \vec{y}_n, \quad (3.13)$$

- and the function

$$F(\vec{Y}) := (f(\mathbf{Y}_1), \dots, f(\mathbf{Y}_s))^T. \quad (3.14)$$

Furthermore, we define the phase space $\vec{\mathcal{X}} := \mathcal{X} \times \dots \times \mathcal{X}$ whereby we have $\vec{Y}, \vec{Z} \in \vec{\mathcal{X}}$. Finally, \otimes denotes the tensor product for matrices, i.e., for matrices A and B , we have

$$A \otimes B = \begin{pmatrix} a_{11}B & \dots & a_{1n}B \\ \vdots & \ddots & \vdots \\ a_{n1}B & \dots & a_{nn}B \end{pmatrix}. \quad (3.15)$$

Now, we are prepared to derive the geodesic equations of motion.

3.2. Geodesic equations of motion

The action S of a free particle of mass m_0 that moves from one point in spacetime x_a to another point x_b is given by

$$S = -m_0 c^2 \int_{x_a}^{x_b} ds, \quad (3.16)$$

where ds is the Lorentz-invariant line element $(ds)^2 = g_{\mu\nu} dx^\mu dx^\nu$. If we parametrize the particle's path via

$$x^\mu = x^\mu(\sigma), \quad \sigma \in \mathbb{R}, \quad (3.17)$$

we get

$$dx^\mu = \underbrace{\frac{dx^\mu}{d\sigma}}_{:=\dot{x}^\mu} d\sigma, \quad (3.18)$$

and thus

$$ds = \sqrt{g_{\mu\nu} \dot{x}^\mu \dot{x}^\nu} d\sigma. \quad (3.19)$$

If we choose as the parameter the line element itself, we have

$$ds = \sqrt{g_{\mu\nu} \dot{x}^\mu \dot{x}^\nu} ds, \quad (3.20)$$

which implies the *four-velocity-constraint*

$$g_{\mu\nu} \dot{x}^\mu \dot{x}^\nu \stackrel{!}{=} 1. \quad (3.21)$$

The particle moves in space in such a way that the action is minimized. Due to the monotony of the square-root, physics does not change if we replace the integrand (3.19) by

$$ds = g_{\mu\nu} \dot{x}^\mu \dot{x}^\nu d\sigma. \quad (3.22)$$

From this, we deduce the Lagrangian function

$$L = \frac{1}{2} m_0 g_{\mu\nu} \dot{x}^\mu \dot{x}^\nu, \quad (3.23)$$

which is a conserved quantity due to the four-velocity constraint.

We now define the momenta p^μ via

$$p_\mu := \frac{\partial L}{\partial \dot{x}^\mu} \quad (3.24)$$

and apply a Legendre transform to the Lagrangian (3.23) to obtain the corresponding Hamiltonian

$$H = p_\mu \dot{x}^\mu - L = \frac{1}{2m_0} g^{\mu\nu} p_\mu p_\nu. \quad (3.25)$$

The variables x^μ and the momenta (3.24) thus satisfy the Hamilton equations

$$\dot{p}_\mu = -\frac{\partial H}{\partial x^\mu} \quad (3.26)$$

$$\dot{x}^\mu = \frac{\partial H}{\partial p_\mu}. \quad (3.27)$$

As, for an EMRI, the gravitational field is considered to be stationary, the metric $g_{\mu\nu}$ and, as a consequence, the Lagrangian does not depend on time explicitly. We thus have an autonomous system with

$$\frac{dH}{d\tau} = 0. \quad (3.28)$$

Most simulations concerning EMRIs consider axisymmetric gravitational fields. Therefore, if we use spherical space-like coordinates, i.e. $x^\mu = (t, r, \theta, \phi)^T$, the metric is independent of ϕ . In these cases, t and ϕ are cyclic coordinates and, hence, the corresponding momenta

$$\mathcal{E} := p_t = \frac{\partial L}{\partial \dot{t}} \quad (3.29)$$

and

$$L_z := p_\phi = \frac{\partial L}{\partial \dot{\phi}} \quad (3.30)$$

are conserved. \mathcal{E} and L_z are the *specific energy* and the *specific azimuthal component of the angular momentum* respectively. With these two additional constants, the number of ordinary differential equations of the system (3.26), (3.27) is reduced from eight to four first order equations. Our numerical example of subsection 3.9 is of exactly this type.

But what are the properties of the just mentioned equations of motion? And how to handle these numerically? To address these questions, we switch to a notation common in numerical analysis, as already announced in 3.1.

3.3. Properties of the geodesic equations of motion

Equations (3.26), (3.27) clearly have a canonical structure, i.e., they can be written as

$$\frac{d\mathbf{y}}{d\tau} = f(\mathbf{y}), \quad (3.31)$$

$$f(\mathbf{y}) = J^{-1} \nabla H(\mathbf{y}). \quad (3.32)$$

Hence, symplectic integration schemes should be legitimate candidates for numerically propagating the system. However, there are some properties of the system which complicate its numerical solution.

First, we notice that the ‘mass-matrix‘ in the Hamiltonian 3.25, which in this case is the metric $g_{\mu\nu}$, apparently depends on the positions. Consequently, the Hamiltonian cannot be separated in the form

$$H(\mathbf{p}, \mathbf{x}) = T(\mathbf{p}) + V(\mathbf{x}). \quad (3.33)$$

Sadly, a non-separable Hamiltonian and the explicitness of a symplectic scheme are mutually exclusive, as it is shown by [Hairer *et al.* \(2006\)](#) for example. As a consequence, one has to apply implicit schemes.

What is more, in most applications of the geodesic approach, the metric is such that the system lacks a fourth first integral such as the *Carter constant* in the Kerr case. As a consequence, not only does the system become non-integrable but also is it often highly sensitive to changes in the argument. To state this in a formal way, let $(Df)(\mathbf{y})$ denote the Jacobian of $f(\mathbf{y})$ around some point \mathbf{y} in the phase space \mathcal{X} . Then, there exists a subset $\mathcal{U} \subset \mathcal{X}$, with

$$\|(Df)(\mathbf{y})\| \gg 1, \quad \forall \mathbf{y} \in \mathcal{U}. \quad (3.34)$$

We will see below that this condition combined with the non-separability poses severe restrictions on the implementation of structure preserving algorithms. But first, we introduce a class of structure preserving integration schemes suited for non-separable problems.

3.4. Gauss-Runge-Kutta methods

Gauss-Runge-Kutta methods are in fact collocation methods. Therefore, we give some background concerning these schemes.

Given an interval $[\tau_0, \tau_0 + h]$, stages $0 \leq c_1 < \dots < c_s \leq 1$, and an initial-value problem

$$\mathbf{y}(\tau_0) = \mathbf{y}_0, \quad (3.35)$$

$$\frac{d\mathbf{y}}{d\tau} = f(\tau, \mathbf{y}), \quad (3.36)$$

the polynomial $u(\tau)$ of degree s , satisfying

$$u(\tau_0) = \mathbf{y}_0, \quad (3.37)$$

$$\dot{u}(\tau_0 + c_i h) = f(\tau_0 + c_i h, u(\tau_0 + c_i h)), \quad i = 1, \dots, s \quad (3.38)$$

is called a *collocation polynomial*.

In order to solve an initial-value problem (3.35), (3.36) by *collocation*, one has to find the polynomial $u(\tau)$ which satisfies the collocation conditions (3.37), (3.38). This gives an approximate solution of the initial value problem after a time step h by setting

$$\mathbf{y}(\tau_0 + h)_{\text{col}} := u(\tau_0 + h). \quad (3.39)$$

A detailed introduction to collocation methods can be found in ([Hairer *et al.*, 1993](#)).

It can now readily be shown, e.g., ([Hairer *et al.*, 1993](#)), that a collocation method is equivalent to an implicit s -stage Runge-Kutta scheme

$$\mathbf{y}_{n+1} = \mathbf{y}_n + h \sum_{i=1}^s b_i f(\mathbf{Y}_i), \quad (3.40)$$

$$\mathbf{Y}_i = \mathbf{y}_n + h \sum_{j=1}^s a_{ij} f(\mathbf{Y}_j), \quad (3.41)$$

with coefficients

$$a_{ij} = \int_0^{c_i} l_j(\tau) d\tau, \quad (3.42)$$

$$b_j = \int_0^1 l_i(\tau) d\tau. \quad (3.43)$$

Here, $l_i(\tau)$ denote the *Lagrange-polynomials* of degree s

$$l_i(\tau) = \prod_{i \neq j} \frac{\tau - c_j}{c_i - c_j}. \quad (3.44)$$

Depending on which set of stages $0 \leq c_1 < \dots < c_s \leq 1$ is chosen, different collocation methods can be constructed. By setting

$$c_i = \frac{1}{2}(1 + \tilde{c}_i), \quad (3.45)$$

with \tilde{c}_i being the roots of the *Legendre-polynomial* of degree s , one obtains a *Gauss collocation method*. The order of this methods is $\mathcal{O}(h^{2s})$, cf. (Hairer *et al.*, 1993), which is optimal in the sense that there are no other s -stage one-step methods that achieve a similar high order without further numerical ruse. In addition, Gauss collocation methods are symplectic and time-reversible, as is proven in (Hairer *et al.*, 2006). Due to all these properties, implicit Gauss-Runge-Kutta methods are one of the most popular candidates for solving non-separable Hamiltonian systems.

Rewriting the set of implicit equations (3.41) in matrix-vector notation yields

$$\begin{pmatrix} \mathbf{Y}_1 \\ \vdots \\ \mathbf{Y}_s \end{pmatrix} = h \begin{pmatrix} a_{11}\mathcal{I} & \dots & a_{1s}\mathcal{I} \\ \vdots & \ddots & \vdots \\ a_{s1}\mathcal{I} & \dots & a_{ss}\mathcal{I} \end{pmatrix} \begin{pmatrix} f(\mathbf{Y}_1) \\ \vdots \\ f(\mathbf{Y}_s) \end{pmatrix}. \quad (3.46)$$

Using the notation introduced in 3.1, we can write equation (3.46) as

$$\vec{Y} = \vec{y}_n + h(A \otimes \mathcal{I})F(\vec{Y}). \quad (3.47)$$

Employing the auxiliary variables (3.13), the Runge-Kutta scheme's implicit equations (3.41) can be given in quite short form as

$$\vec{Z} = h(A \otimes \mathcal{I})F(\vec{Z}). \quad (3.48)$$

Here, $F(\vec{Z})$ is to be read as

$$F(\vec{Z}) = \begin{pmatrix} f(\mathbf{Y}_1) \\ \vdots \\ f(\mathbf{Y}_s) \end{pmatrix} = \begin{pmatrix} f(\mathbf{y}_n + \mathbf{Z}_1) \\ \vdots \\ f(\mathbf{y}_n + \mathbf{Z}_s) \end{pmatrix}. \quad (3.49)$$

The system of implicit equations (3.48) has to be solved during each integration step. We will see in the following, that this leads to a constraint on the allowed step sizes.

3.5. The need for an efficient step size algorithm

There are two possibilities to solve equation (3.48) for the inner stage values \vec{Z} .

- The most straightforward way is to apply a direct iteration or *fixed-point iteration*, i.e., to iterate

$$\vec{Z}^{k+1} = h(A \otimes \mathcal{I})F(\vec{Z}^k). \quad (3.50)$$

A sufficient condition for its convergence is given by the *Banach fixed-point theorem*: If the iteration (3.50) is a contraction on the whole space \mathcal{X} then it converges towards a unique solution \vec{Z} .

For this to hold, we need

$$\left\| \vec{Z}^{k+2} - \vec{Z}^{k+1} \right\| \stackrel{!}{<} \left\| \vec{Z}^{k+1} - \vec{Z}^k \right\|. \quad (3.51)$$

Because of

$$\begin{aligned} \left\| \vec{Z}^{k+2} - \vec{Z}^{k+1} \right\| &= \left\| h(A \otimes \mathcal{I})(F(\vec{Z}^{k+1}) - F(\vec{Z}^k)) \right\| \\ &\leq \max_{\vec{Z} \in \mathcal{X}} \left\| h(A \otimes \mathcal{I})(DF)(\vec{Z}) \right\| \left\| \vec{Z}^{k+1} - \vec{Z}^k \right\|, \end{aligned} \quad (3.52)$$

condition (3.51) is nothing other than

$$h \left\| (A \otimes \mathcal{I})DF(\vec{Z}) \right\| \stackrel{!}{<} 1, \quad \forall \vec{Z} \in \mathcal{X}. \quad (3.53)$$

- An alternative to the simple iteration above is based on the modified *Newton iteration*. In this case, we search for the roots of the function

$$\hat{F}(\vec{Z}) := \vec{Z} - h(A \otimes \mathcal{I})F(\vec{Z}), \quad (3.54)$$

wherefore we use the very modified Newton iteration. Hence, we iterate

$$\vec{Z}^{k+1} = \vec{Z}^k + \Delta \vec{Z}^k \quad (3.55)$$

$$\Delta \vec{Z}^k = -M^{-1} \hat{F}(\vec{Z}^k), \quad (3.56)$$

with

$$M := \mathcal{I} - (A \otimes \mathcal{I})(\mathcal{I} \otimes Df(\mathbf{y}_n)). \quad (3.57)$$

Combining (3.55) and (3.56) to one single step

$$\vec{Z}^{k+1} = \vec{Z}^k - M^{-1} \hat{F}(\vec{Z}^k), \quad (3.58)$$

we see that the Newton iteration is in fact a pre-conditioned fixed-point iteration. Thus, we can again apply Banach's theorem as soon as we can ensure

$$\begin{aligned} \left\| \vec{Z}^{k+2} - \vec{Z}^{k+1} \right\| &= \left\| \vec{Z}^{k+1} - M^{-1} \hat{F}(\vec{Z}^{k+1}) - \left(\vec{Z}^k - M^{-1} \hat{F}(\vec{Z}^k) \right) \right\| \\ &\leq \max_{\vec{Z} \in \mathcal{X}} h \left\| \mathcal{I} - M^{-1} D\hat{F}(\vec{Z}) \right\| \left\| \vec{Z}^{k+1} - \vec{Z}^k \right\| \\ &\stackrel{!}{<} \left\| \vec{Z}^{k+1} - \vec{Z}^k \right\|, \end{aligned} \quad (3.59)$$

or rather

$$h \left\| \mathcal{I} - M^{-1} D\hat{F}(\vec{Z}) \right\| \stackrel{!}{<} 1, \quad \forall \vec{Z} \in \vec{\mathcal{X}}. \quad (3.60)$$

When using a modified Newton iteration, one has to calculate a Jacobian and to solve a linear system which can be very costly. The reduced number of iterations normally does not make up for this additional effort. Consequently, one should prefer the fixed-point iteration whenever it is possible. Even heavier machinery for the solution of the implicit equation (3.48) is supplied by the *Newton-Raphson method*. There, M in eq. (3.56) is replaced by

$$M(\vec{Z}^k) = \mathcal{I} - (A \otimes \mathcal{I})(DF(\vec{Z}^k)). \quad (3.61)$$

This gives an iteration with quadratic convergence. But it is much more expensive because a Jacobian has to be calculated at every iteration step. Hence, standard literature recommends to do without it whenever possible, e.g., (Hairer *et al.*, 2006). In the numerical experiments part 3.10 we will observe that this still holds true for geodesic equations of motion.

But no matter which iterative scheme we use to solve the implicit equations that inevitably arise with the use of a collocation method, we always have some restriction on the step size. It has to be small enough for a requirement such as (3.53) or (3.60) to hold. For cases with the property (3.34) of high sensitivity on changes in the argument, this means that to propagate the system in the subset \mathcal{U} , we have to choose a very small step size $h \ll 1$. On the other hand, there will almost surely be other parts \mathcal{V} of the phase space, where

$$\|(Df)(\mathbf{y})\| \sim 1, \quad \forall \mathbf{y} \in \mathcal{V}. \quad (3.62)$$

or even parts $\tilde{\mathcal{V}}$ with

$$\|(Df)(\mathbf{y})\| \ll 1, \quad \forall \mathbf{y} \in \tilde{\mathcal{V}}. \quad (3.63)$$

Propagating the system in this parts of the phase space with the very small step size h adapted to the part \mathcal{U} would be a massive waste of computational time. In parts of the phase space for which (3.62) or (3.63) hold, one would rather work with a large step size.

The only way to cope with this problem is to use a variable step size. But finding a suitable variable step size algorithm for problems common in the geodesic approach is not a simple task as we will argue next.

3.6. (Problems with) existing step size algorithms

Variable step sizes have been used for a long time in applications such as stiff differential equations, e.g., (Hairer and Wanner, 1996). The perhaps easiest way would be to compare the numerical solution \mathbf{y}_n with a reference solution and calculate their difference. This can then be interpreted as the error of the numerical solution. If this error is larger than a given tolerance, one can reduce the step size and calculate the last step from anew. If, on the other hand, the numerical integrator does satisfyingly well, one could increase the step size before calculating the next step.

But, however well such algorithms may work in some cases, one cannot simply combine them with geometric integrators. Trying to do so, one would realize that the structure preserving

property will be lost. An illustration of this phenomenon is given by [Hairer et al. \(2006\)](#). In fact, [Stoffer \(1988\)](#) demonstrated that variable step size and efficient symplectic integration are mutually exclusive. Thus, the following structure preserving properties such as *symmetry* and *reversibility* come to the fore:

- A numerical integration scheme Φ_h is called *symmetric*, if it satisfies

$$\Phi_{-h}(y) = \Phi^{-1}(y). \quad (3.64)$$

- It is called *time-reversible* if for the linear involution

$$\zeta \begin{pmatrix} \mathbf{p} \\ \mathbf{x} \end{pmatrix} = (-\mathbf{p}, \mathbf{x}), \quad (3.65)$$

one has

$$\Phi_h^{-1} \circ \zeta = \zeta \circ \Phi_h. \quad (3.66)$$

When applying a symmetric, reversible integration scheme to a symmetric, reversible problem, one can expect the same benevolent long-time behaviour as when applying a symplectic scheme to a canonical system. [Hairer et al. \(2006\)](#) discuss this in great detail.

Over the last years, some few step size controllers have been proposed for applications in classical (celestial) mechanics. The most efficient and popular among these was presented by [Hairer and Söderlind \(2005\)](#). They express the variable step size sequence $\tau = \tau_1, \dots, \tau_n, \tau_{n+1}, \dots$ by means of a constant step size sequence $\epsilon = \epsilon_1, \dots, \epsilon_n, \epsilon_{n+1}, \dots$ and a scalar function $\sigma(\mathbf{y})$ via $d\tau = \sigma(\mathbf{y})d\epsilon$. The dependence of \mathbf{y} on ϵ then is as follows:

$$\frac{d\mathbf{y}}{d\epsilon} = \frac{d\mathbf{y}}{d\tau} \frac{d\tau}{d\epsilon} = f(\mathbf{y}) \frac{d\tau}{d\epsilon} = f(\mathbf{y})\sigma(\mathbf{y}). \quad (3.67)$$

Their main idea then is to consider the inverse of the scaling function $\sigma(\mathbf{y})$,

$$w := \frac{1}{\sigma(\mathbf{y})}, \quad (3.68)$$

and its derivative by ϵ

$$\begin{aligned} \frac{dw}{d\epsilon} &= -\frac{1}{\sigma^2}(\nabla\sigma) \frac{d\mathbf{y}}{d\epsilon} \\ &= -\frac{1}{\sigma}(\nabla\sigma)f(\mathbf{y}). \end{aligned} \quad (3.69)$$

The last equality follows by replacing $\frac{d\mathbf{y}}{d\epsilon}$ with the help of relation (3.67). Combining equations (3.67), (3.69) and defining

$$G(\mathbf{y}) := -\frac{1}{\sigma}(\nabla\sigma)f(\mathbf{y}) \quad (3.70)$$

leads to the augmented system

$$\begin{pmatrix} \frac{d\mathbf{y}}{d\epsilon} \\ \frac{dw}{d\epsilon} \end{pmatrix} = \begin{pmatrix} \frac{1}{w}f(\mathbf{y}) \\ G(\mathbf{y}) \end{pmatrix}. \quad (3.71)$$

Hairer and Söderlind (2005) solve this system with the scheme

$$w_{n+\frac{1}{2}} = w_n + \epsilon G(\mathbf{y}_n) \quad (3.72)$$

$$\mathbf{y}_{n+1} = \Phi_{\epsilon/w_{n+\frac{1}{2}}}(\mathbf{y}_n) \quad (3.73)$$

$$w_{n+1} = w_{n+\frac{1}{2}} + \epsilon G(\mathbf{y}_{n+1}), \quad (3.74)$$

$$w_0 = \frac{1}{\sigma(\mathbf{y}_0)}, \quad (3.75)$$

where Φ_h is a symmetric reversible integrator for the original equation of motion (3.31). This method is symmetric and time-reversible, (Hairer and Söderlind, 2005).

Unfortunately, this scheme is of almost no use for the non-integrable systems of the geodesic approach. To demonstrate this, let us denote the scheme (3.72) - (3.75) by

$$\begin{pmatrix} \mathbf{y}_{n+1} \\ w_{n+1} \end{pmatrix} = \chi_\epsilon(\mathbf{y}_n, w_n). \quad (3.76)$$

The integrator χ_ϵ is in fact strang splitted as

$$\chi_\epsilon(\mathbf{y}_n, w_n) = \phi_{\epsilon/2} \circ \Phi_\epsilon \circ \phi_{\epsilon/2}, \quad (3.77)$$

where the propagator $\phi_{\epsilon/2}$ corresponds to (3.72) and (3.74), respectively, and Φ_ϵ propagates \mathbf{y} with fixed w . We now first observe that ϕ is nothing else but the explicit Euler method. This is known to produce reliable results only if the increment $\epsilon G(\mathbf{y}_n)$ is small (which, by the way, is the reason why explicit schemes are not used for stiff differential equations). Next, we already argued that to solve the non-separable initial value problem (3.36) we need to apply a implicit scheme. This will inevitably lead to implicit equations of the form (3.48). Solving this system via a fixed-point iteration requires a step size somehow proportional to the inverse of $\|(Df)(\mathbf{y})\|$ due to the constraint (3.53). Therefore, we have

$$\sigma(\mathbf{y}) \propto \frac{1}{\|(Df)(\mathbf{y})\|}, \quad (3.78)$$

and hence

$$G(\mathbf{y}) = -\frac{1}{\sigma}(\nabla\sigma)f(\mathbf{y}) = \sum_{i,j,k} \frac{((Df)(\mathbf{y}))_{ij} \left(\frac{\partial((Df)(\mathbf{y}))_{ij}}{\partial \mathbf{y}_k} \right) (f(\mathbf{y}))_k}{\|(Df)(\mathbf{y})\|^2}. \quad (3.79)$$

For applications in geodesics, there are surely regions of the phase space where

$$\|D^2f \cdot f\| \gg \|Df\|. \quad (3.80)$$

Thus $\epsilon \cdot G(\mathbf{y}_n)$ would be very large, unless we choose ϵ to be very small. But as ϵ is the underlying constant step size parameter, this would signify that we were again left with a very small constant step size during the whole integration.

Choosing a (modified) Newton iteration for the solution of the implicit equations of the type (3.48) does not improve anything. In this case, we must comply with requirement (3.60), i.e.,

we have

$$\begin{aligned}\sigma(\mathbf{y}) &\propto \frac{1}{\|\mathcal{I} - M^{-1}D\hat{F}(\vec{Z})\|} \\ &= \frac{1}{\|\mathcal{I} - (\mathcal{I} - (A \otimes Df(\mathbf{y}_n)))^{-1}(\mathcal{I} - (A \otimes \mathcal{I})DF(\vec{Z}))\|}.\end{aligned}\quad (3.81)$$

In the scheme (3.72)-(3.75), we have to consider σ as a function of the phase space variable \mathbf{y} . But, is by no means clear how one should do this. The only feasible way would be to set $\vec{Z} = (\mathbf{0}, \dots, \mathbf{0})^T$ in the last expression. To calculate $G(\mathbf{y})$, one would then have to derive σ in (3.81). Derivation of $\frac{1}{\|\dots\|}$ would yield a factor

$$\frac{1}{\|\mathcal{I} - (\mathcal{I} - (A \otimes Df(\mathbf{y}_n)))^{-1}(\mathcal{I} - (A \otimes \mathcal{I})(DF)(\vec{Z}))\|^2}.\quad (3.82)$$

Because of $(DF)(\vec{Z}) = \mathcal{I} \otimes Df(y)$ for the \vec{Z} chosen above, this factor would be

$$\frac{1}{\|\mathcal{I} - (\mathcal{I} - (A \otimes Df(\mathbf{y}_n)))^{-1}(\mathcal{I} - (A \otimes (Df)(\mathbf{y})))\|^2}.\quad (3.83)$$

If, then, in eq. (3.72), we want to evaluate the function G at the point \mathbf{y}_n , we would have to divide by zero due to the factor (3.83). As a consequence, it is not possible to use a Newton iteration along with the presented step size control algorithm. Hence the need for a new controller which will be presented in the next subsection.

3.7. IGEM: A variable step size integration scheme for geodesic equations of motion

The *Integrator for Geodesic Equations of Motion* (IGEM) which we will present now is designed to cope with all the difficulties we have encountered above. Its variable step size $h = h(\epsilon, \mathbf{y})$ depends on both an underlying constant step size ϵ and the actual state of the system \mathbf{y} . As the underlying integrator we use an s -stage Gauss collocation method. With this, our scheme has the following properties:

- It is symmetric and reversible. Therefore, the theoretical results on the long-time behaviour of such schemes are applicable, cf. (Hairer *et al.*, 2006).
- It has convergence order $\mathcal{O}(h^{2s})$ as the order is determined by the underlying integration method.
- For the step size h the relation

$$h(\epsilon, \mathbf{y}) \propto \frac{1}{\|(Df)(\mathbf{y})\|}\quad (3.84)$$

holds, and, thus, the integrator complies with condition (3.53).

The main idea consists of slightly tweaking requirement (3.53) for the step size and setting

$$\|h(Df)(\mathbf{y})\| \stackrel{!}{=} \epsilon, \quad \epsilon < 1.\quad (3.85)$$

The parameter ϵ will act as the underlying constant step size. For symmetry's and reversibility's sake, we modify the defining equation (3.85) to

$$\left\| \frac{h}{2} (Df(\mathbf{Y}_1) + Df(\mathbf{Y}_s)) \right\| \stackrel{!}{=} \epsilon. \quad (3.86)$$

Here, \mathbf{Y}_1 is the inner stage value at the first stage c_1 , \mathbf{Y}_s is its counterpart at the last stage c_s . As will be shown now, this modification ensures the structure preserving properties of the integration scheme.

Symmetry of a numerical scheme means that when starting at a point $\mathbf{y}_{n+1} = \Phi_h(\mathbf{y}_n)$ and then propagating backwards, one must be back at \mathbf{y}_n , i.e.,

$$\Phi_{-h_{\text{backw}}} \circ \Phi_{h_{\text{forw}}}(\mathbf{y}_n) \stackrel{!}{=} \mathbf{y}_n. \quad (3.87)$$

To satisfy this equation, the step size when propagating the system forwards,

$$h_{\text{forw}} = |h(\epsilon, \mathbf{y}_n)|, \quad (3.88)$$

must be the same as the step size for a propagation backwards,

$$h_{\text{backw}} = |h(-\epsilon, \mathbf{y}_{n+1})|. \quad (3.89)$$

In this case, we have

$$\Phi_{-h_{\text{forw}}} \circ \Phi_{h_{\text{forw}}}(\mathbf{y}_n) = \mathbf{y}_n, \quad (3.90)$$

which holds true because the underlying integrator satisfies the symmetry condition (3.64).

Let $\hat{\mathbf{Y}}_i$ denote the inner stage values for the integration backwards in time. The symmetry of the Gauss collocation method then results in

$$\hat{\mathbf{Y}}_i = \mathbf{Y}_{s+1-i} \quad \forall \quad i = 1, \dots, s, \quad (3.91)$$

because the collocation polynomial for $\mathbf{y}_{n+1} = \Phi_h(\mathbf{y}_n)$, which is the interpolation polynomial through the points $(0, y_n)$ and (c_i, \mathbf{Y}_i) , is the same as the collocation polynomial for $\mathbf{y}_n = \Phi_{-h}(\mathbf{y}_{n+1})$, i.e., the interpolation polynomial through the points $(1, y_{n+1})$ and $(c_i, \hat{\mathbf{Y}}_i)$. Here, we tacitly used that for the symmetric Gauss collocation schemes we have

$$c_i = c_{s+1-i}. \quad (3.92)$$

Now, with the help of relation (3.91), we arrive at

$$\begin{aligned} h(-\epsilon, \mathbf{y}_{n+1}) &= \frac{-\epsilon}{\left\| \frac{1}{2} [Df(\hat{\mathbf{Y}}_1) + Df(\hat{\mathbf{Y}}_s)] \right\|} \\ &= \frac{-\epsilon}{\left\| \frac{1}{2} [Df(\mathbf{Y}_s) + Df(\mathbf{Y}_1)] \right\|} \\ &= -h(\epsilon, \mathbf{y}_n). \end{aligned} \quad (3.93)$$

We see that the step sizes are indeed equal. As a consequence, the new integrator is symmetric.

For the proof of reversibility, we regard the variable step size integrator $\Phi_h(\epsilon, \mathbf{y})$ as a constant step size integration scheme Ψ_ϵ . The reversibility condition then reads

$$\Psi_\epsilon^{-1} \circ \zeta \stackrel{!}{=} \zeta \circ \Psi_\epsilon. \quad (3.94)$$

With the symmetry just proven, this is the same as

$$\Psi_{-\epsilon} \circ \zeta \stackrel{!}{=} \zeta \circ \Psi_{\epsilon}. \quad (3.95)$$

Inserting the definition of Ψ_{ϵ} , the condition becomes

$$\Phi_{h(-\epsilon, \zeta \mathbf{y}_{n+1})} \circ \zeta \stackrel{!}{=} \zeta \circ \Phi_{h(\epsilon, \mathbf{y}_n)}. \quad (3.96)$$

From this we see that the reversibility of Ψ_{ϵ} follows by the reversibility of the integrator Φ_h if we can guarantee

$$h(-\epsilon, \zeta \mathbf{y}_{n+1}) = -h(\epsilon, \mathbf{y}_n). \quad (3.97)$$

In order to prove condition (3.97), we denote by $\tilde{\mathbf{Y}}$ the inner stage values for the integration that starts at $\zeta \mathbf{y}_{n+1}$. We then notice, that the reversibility of the Gauss-Runge-Kutta scheme means that when calculating the collocation polynomial through the points $(0, y_n)$ and (c_i, \mathbf{Y}_i) and then multiplying the resulting polynomial with ζ , we have the same polynomial as when calculating the polynomial through $(1, \zeta \mathbf{y}_{n+1})$ and $(c_i, \tilde{\mathbf{Y}}_i)$. Remembering property (3.92), we find

$$\tilde{\mathbf{Y}}_i = \zeta \mathbf{Y}_{s+1-i}. \quad (3.98)$$

Using this relation, we get

$$\begin{aligned} h(-\epsilon, \zeta \mathbf{y}_{n+1}) &= \frac{-\epsilon}{\left\| \frac{1}{2} [Df(\tilde{\mathbf{Y}}_1) + Df(\tilde{\mathbf{Y}}_s)] \right\|} \\ &= \frac{-\epsilon}{\left\| \frac{1}{2} \zeta^{-1} [Df(\mathbf{Y}_s) + Df(\mathbf{Y}_1)] \right\|} \\ &= -h(\epsilon, \mathbf{y}_n), \end{aligned} \quad (3.99)$$

where the last equality is a consequence of the orthogonality of the linear involution ζ . Thanks to relation (3.99), our IGEM is reversible.

To implement our scheme, we combine the implicit equation (3.48) for the auxiliary variables \mathbf{Z}_i with equation (3.86) for the step size and thus get the system

$$\begin{pmatrix} \vec{Z} \\ h \end{pmatrix} = \begin{pmatrix} h(A \otimes \mathcal{I})F(\vec{Z}) \\ \frac{\epsilon}{\left\| \frac{1}{2} [Df(\mathbf{y}_n + \mathbf{Z}_1) + Df(\mathbf{y}_n + \mathbf{Z}_s)] \right\|} \end{pmatrix}. \quad (3.100)$$

In order to solve this, we insert the second equation into to first one and apply a fixed-point iteration. This yields

$$\vec{Z}^{k+1} = \frac{\epsilon(A \otimes \mathcal{I})F(\vec{Z}^k)}{\frac{1}{2} \left\| Df(\mathbf{y}_n + \mathbf{Z}_1^k) + Df(\mathbf{y}_n + \mathbf{Z}_s^k) \right\|}. \quad (3.101)$$

We thus have an implicit Runge-Kutta scheme which we solve iteratively. Therefore, it seems useful to give some remarks regarding the implementation of such schemes.

3.8. Efficient implementation of an implicit Gauss-Runge-Kutta scheme

In theory, Gauss-Runge-Kutta schemes have a good long-time behaviour and conserve first integrals of motion such as the energy up to arbitrarily small remainders. In practice, however, one is confronted with the problem of rounding-errors. At every time step, a small rounding error occurs due to the finite representation of numbers, normally in double precision. These round-off errors can then sum up over the integration and destroy the good long-time behaviour. But these effects can be ameliorated by clever implementation. Let us briefly introduce the main sources of errors and some simple remedies.

- For every one-step method a propagation in time $\mathbf{y}_n \rightarrow \mathbf{y}_{n+1}$ is obtained via

$$\mathbf{y}_{n+1} = \mathbf{y}_n + \delta_n, \quad (3.102)$$

where the increment δ_n is usually much smaller than the old value \mathbf{y}_n . For instance,

$$\delta_n = h \sum_{i=1}^s b_i f(\mathbf{Y}_i) \quad (3.103)$$

for a Runge-Kutta scheme. Adding a small number to a comparingly large one inevitably leads to the loss of the smaller number's last digits. If we have $\delta_n/\|\mathbf{y}_n\| \approx 10^{-2}$ for example, the last two of the 16 decimals of δ_n are not taken into account when calculating \mathbf{y}_{n+1} . Relief to this problem is given by the *compensated summation*. It uses a 'storage' variable $\mathbf{y}_{\text{store}}$ to collect the omitted last decimals at every time step. If, then, the omitted last decimals add up to a large enough number, they are returned back to the actual value \mathbf{y}_n . A numerical one-step scheme with compensated summation looks as follows.

```
1  function one_step_method( $\mathbf{y}_0$ )
2       $\mathbf{y}_{\text{store}} = 0$ ;
3       $\mathbf{y}_n = \mathbf{y}_0$ ;
4      do while( $\tau < t_{\text{end}}$ )
5
        calculate_increment( $f, \delta_n, \mathbf{y}_n$ )
         $\tau = \tau + h$ ;
        // start of compensated summation
         $\mathbf{y}_{\text{store}} = \mathbf{y}_{\text{store}} + \delta_n$ ;
         $\mathbf{y}_{n+1} = \mathbf{y}_n + \mathbf{y}_{\text{store}}$ ;
         $\mathbf{y}_{\text{store}} = \mathbf{y}_{\text{store}} + (\mathbf{y}_n - \mathbf{y}_{n+1})$ ;
        // end of compensated summation
         $\mathbf{y}_{n+1} = \mathbf{y}_n$ 
6      od
7      end
```

A nice illustration of the compensated summation can be found in ([Higham, 1993](#)).

- Another source of round-off errors is connected to the use of iteration methods for implicit schemes. Often, the iteration for an equation such as (3.48) is implemented in the following way:

```

1   function fixed_point_iteration( $\vec{Z}$ )
2       do while( $\|\vec{Z}^{k+1} - \vec{Z}^k\| > Tol$ )
3           ...;
4       od
5   end
    
```

Here, Tol is a small number but still greater than 0. Thus, again, errors occur during each step which can accumulate. Hairer *et al.* (2008) propose to implement the iteration as

```

1   function fixed_point_iteration( $\vec{Z}$ )
2       do while( $\|\vec{Z}^{k+1} - \vec{Z}^k\| < \|\vec{Z}^k - \vec{Z}^{k-1}\| \ \&\& \ \|\vec{Z}^{k+1} - \vec{Z}^k\| > 0$ )
3           ...;
4       od
5   end
    
```

which they show to reduce the long-time accumulation of errors.

- To reduce the number of iterations, it is recommendable to start the iteration with a good guess for \vec{Z} . For an implicit Runge-Kutta scheme one can easily obtain such a guess without any additional function evaluation. Let \vec{Z}_{n-1} denote the auxiliary variables of the previous step. A reasonable guess for the starting values for the current iteration \vec{Z}_n^0 is then given by

$$\mathbf{Z}_{n,i}^0 = h \sum_{j=1}^s \beta_{ij} f(\mathbf{Z}_{n-1,j}) \quad (3.104)$$

where the function evaluations are available from the previous step. If the coefficients β_{ij} satisfy

$$\sum_{j=1}^s \beta_{ij} c_j^{k-1} = \frac{(1 + c_i)^k}{k}, \quad k = 1, \dots, s, \quad (3.105)$$

one has $\|\vec{Z}_n - \vec{Z}_n^0\| = \mathcal{O}(h^s)$, e.g., (Hairer *et al.*, 2006).

In all simulations for this work, compensated summation was used. The other aforementioned techniques were applied whenever possible, above all when implementing Gauss collocation schemes.

3.9. Our test case: The Manko, Sanabri-Gómez, Manko spacetime background

As a simple example to compare the performance of our new integrator with various others, we choose a stationary solution of the Einstein equations that is asymptotically flat and

axisymmetric. More precisely, we take the solution found by [Manko *et al.* \(2000\)](#) which describes the exterior field of a charged, magnetized, and spinning deformed mass, see ([Manko *et al.*, 2000](#)). The metric depends on five parameters which are

- the mass m ,
- the total charge q ,
- the magnetic dipole moment \mathcal{M} ,
- the mass quadrupole moment \mathcal{Q} ,
- and the spin per unit mass a .

\mathcal{Q} and \mathcal{M} implicitly define two auxiliary parameters μ and b via

$$\mathcal{M} = \mu + q(a - b), \quad (3.106)$$

$$\mathcal{Q} = -m(d - \delta - a b + a^2), \quad (3.107)$$

with

$$\delta := \frac{\mu^2 - m^2 b^2}{m^2 - (a - b)^2 - q^2}, \quad (3.108)$$

$$d := \frac{1}{4}[m^2 - (a - b)^2 - q^2]. \quad (3.109)$$

Because of its axisymmetry, the spacetime can suitably be described by cylindrical position coordinates ρ, ϕ, z . ρ and z can be transformed to prolate spherical coordinates u and v via

$$\begin{pmatrix} u \\ v \end{pmatrix} = \chi^{-1}(\rho, z), \quad (3.110)$$

where

$$\chi(u, v) = \begin{pmatrix} \kappa \sqrt{(u^2 - 1)(1 - v^2)} \\ \kappa uv \end{pmatrix}, \quad (3.111)$$

$$\kappa := \sqrt{d + \delta}. \quad (3.112)$$

With the help of the prolate spherical coordinates, one can define the following auxiliary functions:

$$P := 2\{\kappa m u [(2\kappa u + m)^2 - 2v^2(2\delta + ab - b^2) - a^2 + b^2 - q^2] - 2\kappa^2 q^2 u^2 - 2v^2(4\delta d - m^2 b^2)\}, \quad (3.113)$$

$$R := 4[\kappa^2(u^2 - 1) + \delta(1 - v^2)]^2 + (a - b)[(a - b)(d - \delta) - m^2 b + q \mu](1 - v^2)^2, \quad (3.114)$$

$$S := -4(a - b)[\kappa^2(u^2 - v^2) + 2\delta v^2] + v^2(m^2 b - q \mu), \quad (3.115)$$

$$T := 4(2\kappa m b u + 2m^2 b - q \mu)[\kappa^2(u^2 - 1) + \delta(1 - v^2)] + \dots \\ + (1 - v^2)\{(a - b)(m^2 b^2 - 4\delta d) - \dots \\ - (4\kappa m u + 2m^2 - q^2)[(a - b)(d - \delta) - m^2 b + q \mu]\}, \quad (3.116)$$

$$\lambda_1 := \kappa^2(u^2 - 1), \quad (3.117)$$

$$\lambda_2 := v^2 - 1, \quad (3.118)$$

$$E = R^2 + \lambda_1 \lambda_2 S^2, \quad (3.119)$$

$$D = E + RP + \lambda_2 ST, \quad (3.120)$$

$$F = RT - \lambda_1 SP. \quad (3.121)$$

These messy functions, in turn, help to define three functions

$$f = \frac{E}{D}, \quad (3.122)$$

$$e^{2\gamma} = \frac{E}{16} \kappa^8 (u^2 - v^2)^4, \quad (3.123)$$

$$\omega = (v^2 - 1) \frac{E}{F}, \quad (3.124)$$

with the help of which the components of the metric in prolate spherical coordinates can be given as

$$g_{tt} = -f, \quad (3.125)$$

$$g_{uu} = \frac{\kappa^2 e^{2\gamma}}{f} \frac{u^2 - v^2}{u^2 - 1}, \quad (3.126)$$

$$g_{vv} = \frac{\kappa^2 e^{2\gamma}}{f} \frac{u^2 - v^2}{1 - v^2}, \quad (3.127)$$

$$g_{\phi\phi} = \frac{1}{f} [\kappa^2 (u^2 - 1)(1 - v^2) - (f\omega)^2], \quad (3.128)$$

$$g_{t\phi} = \omega f = g_{\phi t}. \quad (3.129)$$

The other components are all equal to 0. If we insert these expressions for the metric components into equation (3.23), we get the Lagrangian as a function of (t, u, v, ϕ) :

$$L = \frac{1}{2} \left(g_{tt} \dot{t}^2 + 2g_{t\phi} \dot{t} \dot{\phi} + g_{\phi\phi} \dot{\phi}^2 + g_{uu} \dot{u}^2 + g_{vv} \dot{v}^2 \right). \quad (3.130)$$

As the metric does neither depend on t nor on ϕ , we have

$$\frac{\partial L}{\partial t} = 0 \quad (3.131)$$

and

$$\frac{\partial L}{\partial \phi} = 0, \quad (3.132)$$

whereby the energy (3.29) and the angular momentum (3.30) are indeed conserved, as was already mentioned in 3.2. The equations for the energy and the angular momentum,

$$\frac{\partial L}{\partial \dot{t}} = -m_0 \mathcal{E}, \quad (3.133)$$

$$\frac{\partial L}{\partial \dot{\phi}} = L_z, \quad (3.134)$$

can be transformed to yield

$$\dot{t} = \frac{g_{t\phi}L_z + g_{\phi\phi}m_0\mathcal{E}}{\kappa^2(u^2 - 1)(1 - v^2)}, \quad (3.135)$$

$$\dot{\phi} = -\frac{g_{tt}L_z + g_{t\phi}m_0\mathcal{E}}{\kappa^2(u^2 - 1)(1 - v^2)}. \quad (3.136)$$

The Euler-Lagrange equations for u and v ,

$$\frac{d}{ds} \frac{\partial L}{\partial \dot{u}} = \frac{\partial L}{\partial u} \quad (3.137)$$

$$\frac{d}{ds} \frac{\partial L}{\partial \dot{v}} = \frac{\partial L}{\partial v}, \quad (3.138)$$

lead to

$$\ddot{u} = \frac{1}{g_{uu}} \left(\frac{1}{m_0} \frac{\partial L}{\partial u} - \left(\frac{\partial g_{uu}}{\partial u} \dot{u} + \frac{\partial g_{uu}}{\partial v} \dot{v} \right) \dot{u} \right), \quad (3.139)$$

and

$$\ddot{v} = \frac{1}{g_{vv}} \left(\frac{1}{m_0} \frac{\partial L}{\partial v} - \left(\frac{\partial g_{vv}}{\partial u} \dot{u} + \frac{\partial g_{vv}}{\partial v} \dot{v} \right) \dot{v} \right), \quad (3.140)$$

with

$$\frac{1}{m_0} \frac{\partial L}{\partial u} = \frac{1}{2} \left(\frac{\partial g_{tt}}{\partial u} \dot{t}^2 + 2 \frac{\partial g_{t\phi}}{\partial u} \dot{t} \dot{\phi} + \frac{\partial g_{\phi\phi}}{\partial u} \dot{\phi}^2 + \frac{\partial g_{uu}}{\partial u} \dot{u}^2 + \frac{\partial g_{vv}}{\partial u} \dot{v}^2 \right) \quad (3.141)$$

and

$$\frac{1}{m_0} \frac{\partial L}{\partial v} = \frac{1}{2} \left(\frac{\partial g_{tt}}{\partial v} \dot{t}^2 + 2 \frac{\partial g_{t\phi}}{\partial v} \dot{t} \dot{\phi} + \frac{\partial g_{\phi\phi}}{\partial v} \dot{\phi}^2 + \frac{\partial g_{uu}}{\partial v} \dot{u}^2 + \frac{\partial g_{vv}}{\partial v} \dot{v}^2 \right). \quad (3.142)$$

In order to write the Euler-Lagrange equations as a system of first order differential equations, we introduce the ‘momenta’

$$p_u = \dot{u} \quad (3.143)$$

and

$$p_v = \dot{v}. \quad (3.144)$$

With these, the equations of motion (3.31) read

$$\dot{p}_u = \frac{1}{g_{uu}} \left(\frac{1}{m_0} \frac{\partial L}{\partial u} - \left(\frac{\partial g_{uu}}{\partial u} p_u + \frac{\partial g_{uu}}{\partial v} p_v \right) p_u \right), \quad (3.145)$$

$$\dot{p}_v = \frac{1}{g_{vv}} \left(\frac{1}{m_0} \frac{\partial L}{\partial v} - \left(\frac{\partial g_{vv}}{\partial u} p_u + \frac{\partial g_{vv}}{\partial v} p_v \right) p_v \right), \quad (3.146)$$

$$\dot{u} = p_u, \quad (3.147)$$

$$\dot{v} = p_v. \quad (3.148)$$

Their exact form is given by replacing $\dot{\phi}$ and \dot{t} in (3.141) and (3.142) with the help of (3.135) and (3.136) and meticulously calculating all derivatives appearing in (3.139), (3.140), (3.141) and (3.142). The result of this tedious exercise is given in appendix A.

The right hand side of the equations of motion (3.145)-(3.148) is not of the symplectic form (3.32). This is because we express the equations of motion by means of the coordinates u , v and the ‘momenta’ which are in fact their corresponding velocities. We do so because it would be more cumbersome to re-express the velocities through the momenta (3.24). But as the Lagrange formalism leads to the same motion as the canonical Hamiltonian equations (3.26), (3.27), the system is still symplectic. In order to calculate the Hamiltonian’s error in the numerical experiment section, we can consider it as a function of the coordinates and velocities. We simply have to replace the momenta in the Hamiltonian (3.25) with the help of their definition (3.24), i.e., with p_u and p_v now denoting the momenta corresponding to u and v , we use

$$p_u = \frac{\partial L}{\partial \dot{u}} = g_{uu}\dot{u} \quad (3.149)$$

and

$$p_v = \frac{\partial L}{\partial \dot{v}} = g_{vv}\dot{v}. \quad (3.150)$$

Having derived the equations of motion, we are now able to carry out numerical tests in the next section.

3.10. Numerical experiments for the MSM case

As competitors for our IGEM scheme, we choose four methods that are a representative cross-section of frequently used algorithms. Let us shortly introduce them:

- To represent simple explicit methods with constant step size, we use a fifth-order *Cash-Karp Runge-Kutta scheme* (CK5) with constant step size h . The CK5 scheme is given by the following tableau, cf. (Flannery *et al.*, 1992):

$$\begin{array}{c|cccccc}
 0 & & & & & & \\
 1/5 & 1/5 & & & & & \\
 3/10 & 3/40 & 9/40 & & & & \\
 3/5 & 3/10 & -9/10 & 6/5 & & & \\
 1 & -11/54 & 5/2 & -70/27 & 35/27 & & \\
 7/8 & 1631/55296 & 175/512 & 575/13824 & 44275/110592 & 253/4096 & \\
 \hline
 & 37/378 & 0 & 250/621 & 125/594 & 0 & 512/1771.
 \end{array} \quad (3.151)$$

Hereinafter, this method is denoted by ‘CK5con’.

- As an example for explicit schemes with standard ‘stiff differential equations like’ control algorithms, a CK5 method with variable step size, ‘CK5var’, is considered. One step of this algorithm is qualitatively given by the following lines of pseudo code:

```

1   function CK5var_step( $\mathbf{y}_n, \epsilon$ )
2       calculate_CK5con_step( $\mathbf{y}_n, h$ );
3        $\delta H = \left| \frac{H(\mathbf{y}_{n+1}) - H(\mathbf{y}_n)}{H(\mathbf{y}_n)} \right|;$ 
    
```

```

4      if( $\delta H > tol_1$  &&  $h > h_{min}$ ) then
5           $h = \frac{h}{2}$ ;
6          go back to line 2;
7      elseif( $\delta H < tol_2$  &&  $h < h_{max}$ ) then
8           $h = 2h$ ;
9      fi
10      $\mathbf{y}_n = \mathbf{y}_{n+1}$ ;
11 end

```

Unless stated otherwise, the parameters are set to be $h_{min} = 10^{-10}$, $tol_1 = 10^{-12}$, and $tol_2 = 10^{-14}$. For h_{max} we used different values during the experiments.

- We also test one of the most popular controllers in classical astronomy. This is the algorithm exposed in section 3.6 where the scaling function is $\sigma(\mathbf{y}) = 1/\|f(\mathbf{y})\|$. As the underlying integrator, we choose implicit Gauss-Runge-Kutta schemes. This method will be referred to as ‘Astro1’.
- To illustrate the problems which harsh conditions on the implicit equations such as (3.53) pose to step size controllers of classical astronomy, we combine the controller of section 3.6 with the scaling function $\sigma(\mathbf{y}) = 1/\|(Df)(\mathbf{y})\|$. Again, implicit Gauss collocation methods are used as the underlying integrator. In the following, this algorithm shows up under the name ‘Astro2’.

All schemes employed in this section are implemented in the error-minimizing way described in section 3.8. As for our test case, the parameters introduced in 3.9 are fixed as $m = 2.904$, $a = 1.549$, $q = 0$, $\mu = 0$, and $b = 0.8$. The constant momenta are set to be $E = 0.971$ and $L_z = 9.3$, respectively. Our calculations are done using the prolate spherical coordinates for which the equations of motion were derived in 3.9, i.e., the variables of our $N = 4$ -dimensional phase space are

$$\mathbf{y}_n = (\dot{u}, \dot{v}, u, v). \quad (3.152)$$

The output is given in cylindrical coordinates which are linked to the prolate ones via the transformation (3.111). To compare the individual methods, we analyse the relative error in the Hamiltonian

$$\Delta H = \left| \frac{H(\mathbf{y}_n) - H(\mathbf{y}_0)}{H(\mathbf{y}_0)} \right|. \quad (3.153)$$

In chapter 2, bad energy conservation was shown to cause incorrect predictions of a system’s behaviour. Therefore, our simulations are aborted due to low accuracy as soon as

$$\Delta H > 10^{-6}. \quad (3.154)$$

The Hamiltonian has a constant value of $H = -1/2$. With regard to the initial values, we always set $z = \dot{\rho} = 0$, while we vary ρ to obtain different sorts of motion. The vertical velocity \dot{z} is then implicitly determined by

$$H(\rho, z = 0, \dot{\rho} = 0, \dot{z}) \stackrel{!}{=} -\frac{1}{2}. \quad (3.155)$$

We consider three different sorts of motion.

3.10.1. $\rho = 30.7$: Quasiperiodic motion

For $\rho = 30.7$ the orbit is regular. To illustrate this, we plot in Fig. 3.1 the trajectory in the configuration space along with the Poincaré sections for $z = 0$ as obtained via the ‘exact’ solution for $\tau \in [0, 500\,000]$. The ‘exact’ solution is given by IGEM with the very small step size $\epsilon = 0.01$ and $s = 6$ stages in the underlying integrator. To compare the accuracy of

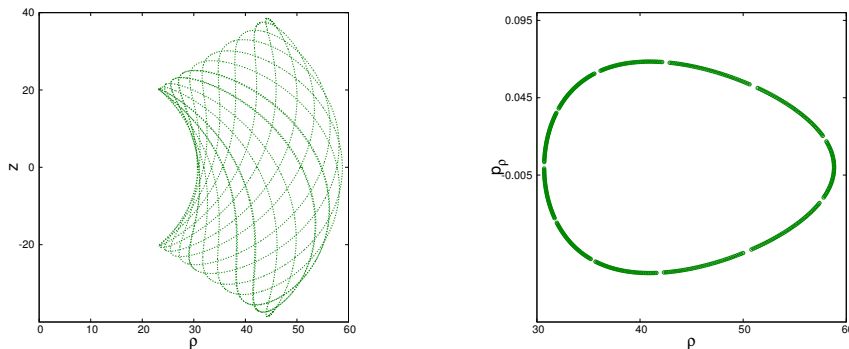


Figure 3.1: For the case $\rho = 30.7$ the left panel is showing the ρ, z -projection of the trajectory of the light particle in the time interval $\tau \in [0, 500\,000]$. The corresponding sections of the $z = 0$ -plane are depicted in right panel. The plots clearly correspond to quasiperiodic motion. N.b.: The quantity along the right panel’s vertical axis is the ‘momentum’ $p_\rho = \dot{\rho}$ as introduced in 3.9.

the individual integrators, we plot their relative error in the energy for an integration time $\tau \in [0, 500\,000]$ in Fig. 3.2. In table 3.1, we list the respective calculation times T_{calc} the integrators needed to arrive at $\tau = 500\,000$.

Integrator	$T_{\text{calc}}[\text{s}]$
CK5con, $h = 0.01$	222.9
CK5var, $h_{\text{max}} = 0.01$	160.6
Astro1, $\epsilon = 1.0, s = 4$	17.3
Astro2, $\epsilon = 1.0, s = 4$	46.1
IGEM, $\epsilon = 1.0, s = 4$	41.3

Table 3.1: The CPU calculation times for the proper time interval $\tau \in [0, 500\,000]$ for the individual integration schemes in the quasiperiodic case $\rho = 30.7$.

The CK5 schemes do not conserve the first integral of motion but show a linear drift. This is despite their very small step size which in turn makes them very slow. The other integrators show, up to rounding errors, no variation in this constant of motion. Taking into account the calculation times, we observe that the Astro1 shows the best performance for this quasiperiodic motion case. This is no surprise given the fact that for the relatively large initial distance $\rho = 30.7$ between the two particles, the system resembles a classical Keplerian motion. Astro1 was constructed for exactly those classical planetary orbits.

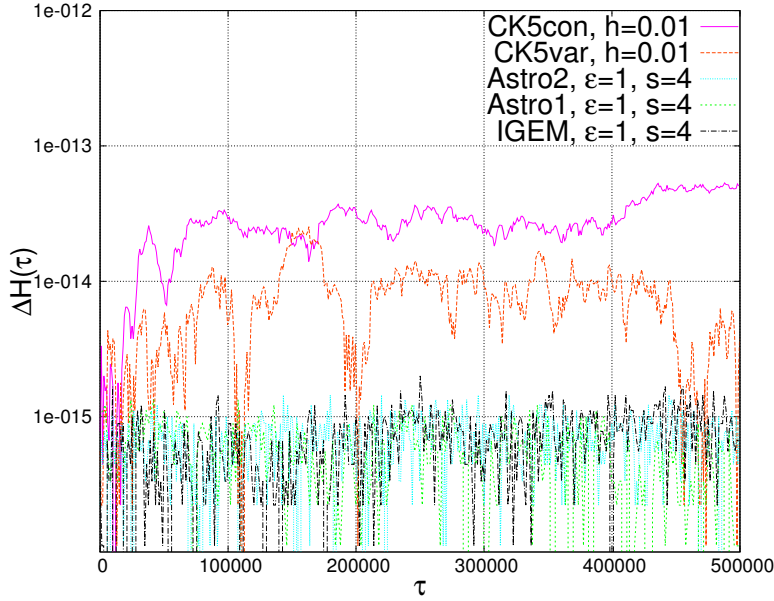


Figure 3.2: The relative error in the Hamiltonian for the respective integration schemes with initial condition $\rho = 30.7$. The explicit schemes show a linear drift but the other integrators conserve the energy.

3.10.2. $\rho = 1.7$: Non-chaotic but ill-mannered sort of motion

With this shorter initial distance between the light particle and the stationary, heavy one, the motion becomes a bit ‘nastier’. To demonstrate this, we again plot the trajectory in the configuration space together with the corresponding Poincaré section as given by the ‘exact’ solution, s. Fig 3.3. As the ‘exact’ solution, we again take IGEM with $\epsilon = 0.01$ and $s = 6$. To further illustrate the behaviour of the motion, we track the the step sizes of the IGEM-integrator with $\epsilon = 0.1$ along the propagation (Fig. 3.4), as we have $h \propto 1/\|Df(y(\tau))\|$. $\|Df(y(\tau))\|$ is varying fast with time. For this kind of orbit, we again tested the individual integrators. When we used the CK5var scheme, it needed one week of calculation time only to arrive at $\tau = 758$. Therefore, we relaxed the restrictions on the acceptable relative errors per step and set $tol_1 = 10^{-9}$ and $tol_2 = 10^{-11}$. The result of the simulations is shown in Fig. 3.5 and table 3.2. We observe that the symplectic standard schemes from classical celestial

Integrator	$T_{\text{calc}}[\text{s}]$
CK5con, $h = 10^{-4}$	23813.2
CK5var, $h_{\text{max}} = 10^{-4}$	19207.7
Astro1, $\epsilon = 0.1$, $s = 4$	266.9
Astro2, $\epsilon = 0.1$, $s = 4$	2100.9
IGEM, $\epsilon = 0.1$, $s = 4$	2202.1

Table 3.2: The calculation times T_{calc} for the proper time interval $\tau \in [0, 500\,000]$ for the different integrators in the case of the still regular orbit with $\rho = 1.7$.

mechanics are fastest but show very bad conservation properties for the Hamiltonian. The

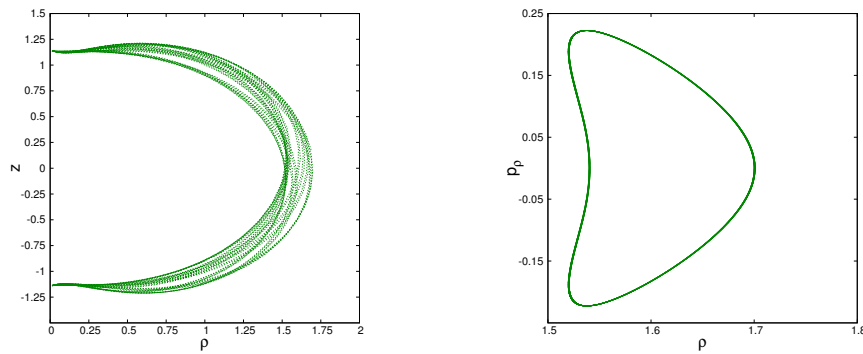


Figure 3.3: For the case $\rho = 1.7$ the left panel is showing the ρ, z -projection of the trajectory of the light particle in the time interval $\tau \in [0, 500\,000]$. The corresponding sections of the $z = 0$ -plane are depicted in the right panel. The Poincaré section shows the quasiperiodic character of the motion but the trajectory behaves in a more ill-mannered way. N.b.: The quantity along the right panel's vertical axis is the 'momentum' $p_\rho = \dot{\rho}$ as introduced in 3.9.

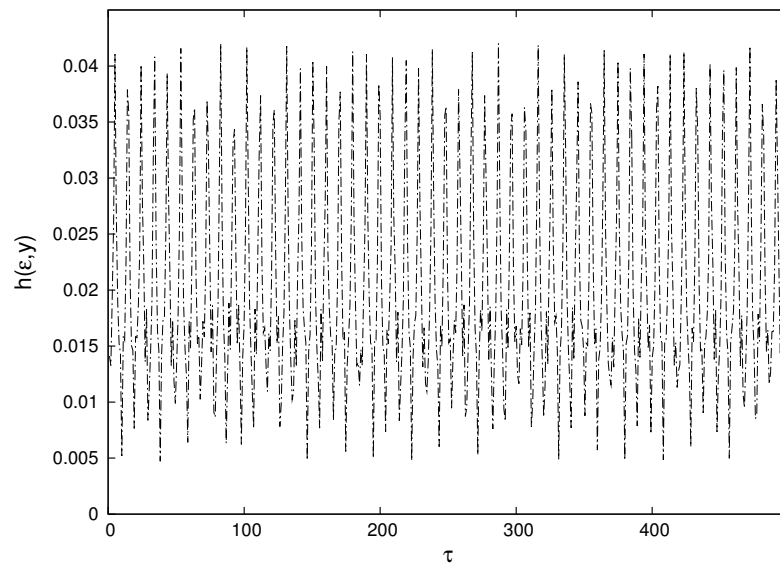


Figure 3.4: The variable step size of the IGEM integrator as function of integration time τ .

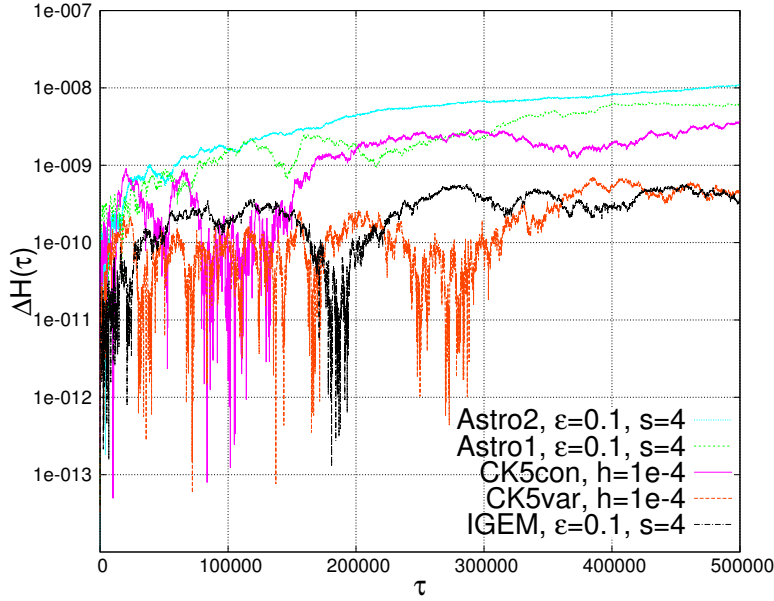


Figure 3.5: The relative error ΔH as function of the proper time τ in normal scale for the orbit with $\rho = 1.7$.

relative error is even worse than for the constant step size, explicit CK5con which shows a linear drift. On the other side of the spectrum, IGEM shows the best long-time behaviour for affordable computational cost.

As, in this work, we are concerned with the impact which a certain scheme can have on the indicators of chaos, we now consider the Poincaré sections resulting from the five schemes. First, we see that the number of sections in the integration interval (25699) is the same for every integrator. Calculating the relative error at each section as

$$err = \sqrt{\frac{(\rho_{\text{num}} - \rho_{\text{exact}})^2}{\rho_{\text{exact}}^2} + \frac{(p_{\rho_{\text{num}}} - p_{\rho_{\text{exact}}})^2}{p_{\rho_{\text{exact}}}^2}}, \quad (3.156)$$

we observe in Fig. 3.6 that there are large differences between the schemes, in accord with Fig. 3.5. But looking at the respective sections in Fig. 3.7, we see that for the time interval of the simulation, the differences in err do not yet result in qualitatively different plots.

3.10.3. $\rho = 0.7$: Chaotic motion

Putting the two objects this close together, leads to chaotic motion. To visualize this, we show the trajectory of the light particle along with its Poincaré section in Fig 3.8. Additionally, we plot the Fourier spectrum for ρ in figure 3.9. We see that the motion has no distinguished frequency and noise prevails. This is characteristic for chaotic orbits.

As in this case the calculation becomes much more expensive, we reduce the integration interval to $\tau \in [0, 50000]$. We again conducted simulations with all five integration schemes. The results of these simulations are listed in table 3.3. All of them, except the one with IGEM, were soon aborted because of low accuracy. For Astro1 the step size became negative during

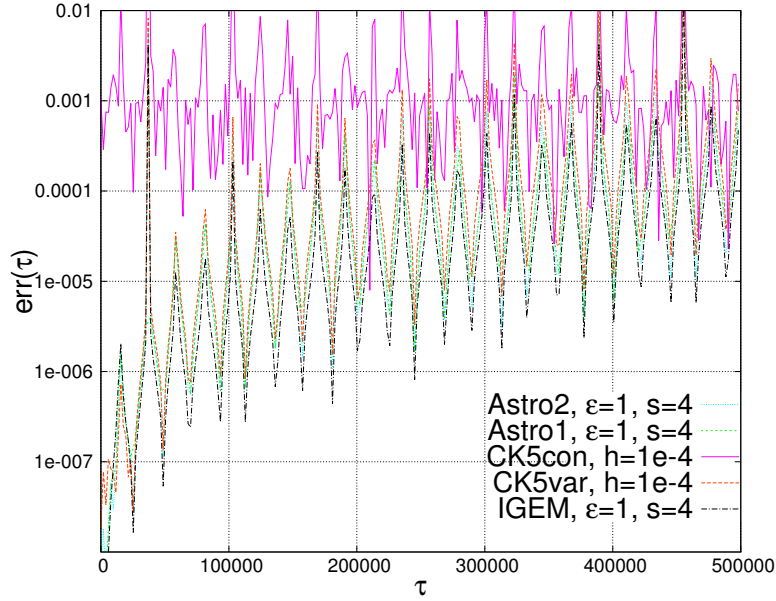


Figure 3.6: The relative error err at the Poincaré sections as function of the proper time τ in normal scale for the orbit with $\rho = 1.7$.

the simulation. We see, that the IGEM is the only scheme that can cope with this initial conditions. But when plotting its relative error in the Hamiltonian in Fig. 3.10 we observe

Integrator	result	$T_{\text{calc}}[\text{s}]$ until abortion
CK5con, $h = 10^{-6}$	aborted after propagation time of $\tau = 11254.0$ because $\Delta H > 10^{-6}$	40739.7
CK5var, $h_{\text{max}} = 10^{-4}$	aborted after propagation time of $\tau = 1087.3$ because $\Delta H > 10^{-6}$	149469.9
Astro1, $\epsilon = 0.01$, $s = 4$	aborted after propagation time of $\tau = 9559.9$ because $h(l, \mathbf{y}) < 0$	34.2
Astro2, $\epsilon = 0.01$, $s = 4$	aborted after propagation time of $\tau = 4180.1$ because $\Delta H > 10^{-6}$	1353.9
IGEM, $\epsilon = 0.1$, $s = 4$	no abortion in $\tau = [0, 50000]$, $T_{\text{calc}} = 995.3\text{s}$.	–

Table 3.3: Results of the simulations for the chaotic orbit with $\rho = 0.7$.

some peaks. In order to explain them, we first notice that they coincide with non-convergence of the fixed-point iteration (3.101). For this iteration to be a contraction, it must satisfy

$$\left\| D \left(\frac{\epsilon(A \otimes \mathcal{I})F(\vec{Z})}{\frac{1}{2}\|Df(\mathbf{Z}_1) + Df(\mathbf{Z}_s)\|} \right) \right\| \stackrel{!}{<} 1, \quad (3.157)$$

with

$$\begin{aligned} D \left(\frac{\epsilon(A \otimes \mathcal{I})F(\vec{Z})}{\frac{1}{2}\|Df(\mathbf{Z}_1) + Df(\mathbf{Z}_s)\|} \right)_{ij} &= \frac{(\epsilon(A \otimes \mathcal{I})(DF)(\vec{Z}))_{ij}}{\frac{1}{2}\|Df(\mathbf{Z}_1) + Df(\mathbf{Z}_s)\|} - \frac{(\epsilon(A \otimes \mathcal{I})F(\vec{Z}))_i}{\frac{1}{2}\|Df(\mathbf{Z}_1) + Df(\mathbf{Z}_s)\|^3} \times \dots \\ &\times \sum_{kl} (Df(\mathbf{Z}_1)_{kl} + Df(\mathbf{Z}_s)_{kl}) \frac{\partial (Df(\mathbf{Z}_1)_{kl} + Df(\mathbf{Z}_s)_{kl})}{\partial \vec{Z}_j}. \end{aligned} \quad (3.158)$$

The norm of the first term is smaller than 1 by construction of the algorithm but the second term can be large. This happens at points, where $f(\mathbf{y})$ becomes almost singular. To see

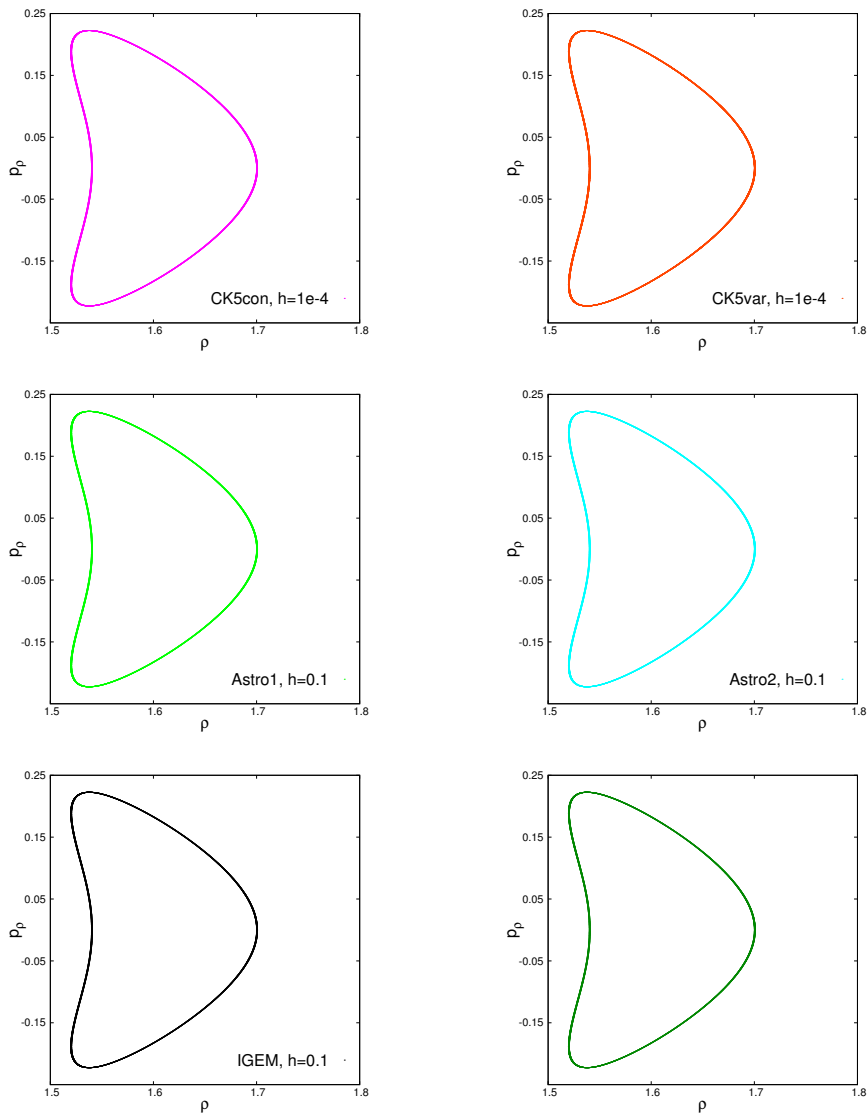


Figure 3.7: Poincaré sections for the case $\rho = 1.7$ for an integration time $\tau \in [0, 500\,000]$. All plots resemble the exact Poincaré section shown in the bottom right panel.

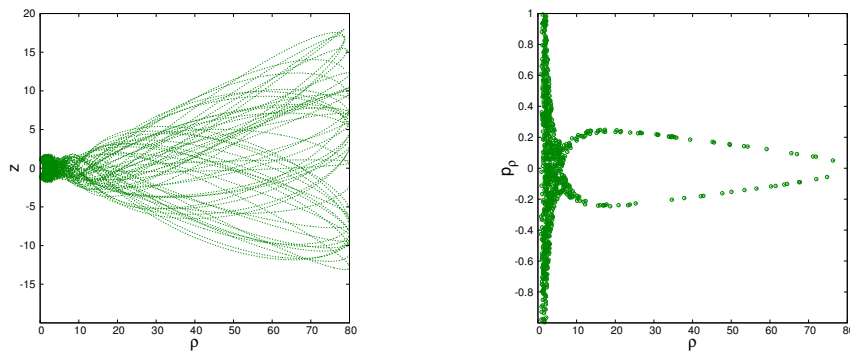


Figure 3.8: For the case $\rho = 0.7$ the left panel is showing the ρ, z -projection of the trajectory of the light particle in the time interval $\tau \in [0, 5000]$. The unusual Poincaré section as shown in the right panel suggests chaotic motion.

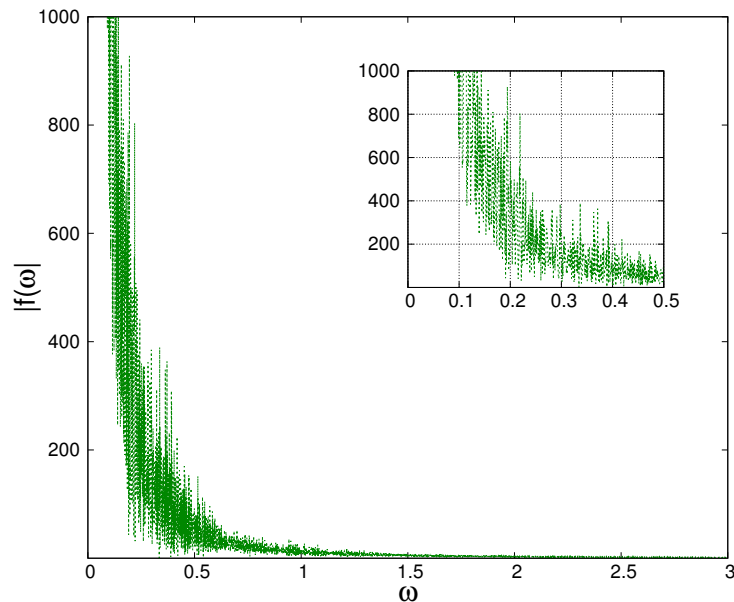


Figure 3.9: For the case $\rho = 0.7$ and the time interval $\tau \in [0, 5000]$, the spectrum of frequencies $|f(\omega)| = \left| \int e^{i\omega\tau} \rho(\tau) d\tau \right|$ clearly shows the characteristic noise of chaotic orbits. A magnification of the Fourier spectrum is shown in the embedded panel.

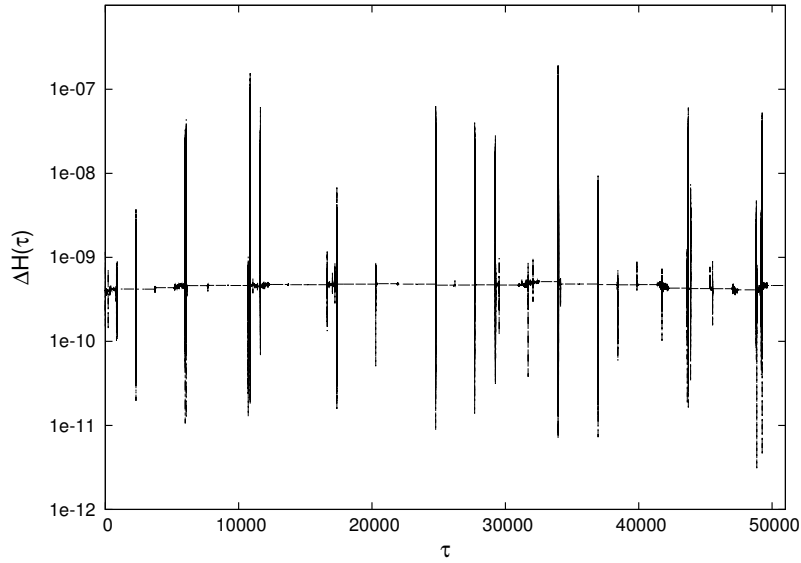


Figure 3.10: The relative error ΔH in semi-logarithmic scale for the IGEM with $\epsilon = 0.1$ as a function of proper time τ for the chaotic orbit with $\rho = 0.7$.

this, we plot the ‘velocity’ $V^2(\tau) = \dot{z}^2 + \dot{\rho}^2$ in Fig. 3.11. We observe that each peak in the Hamiltonian comes hand in hand with a peak in the velocity. To analyse the peaks further,

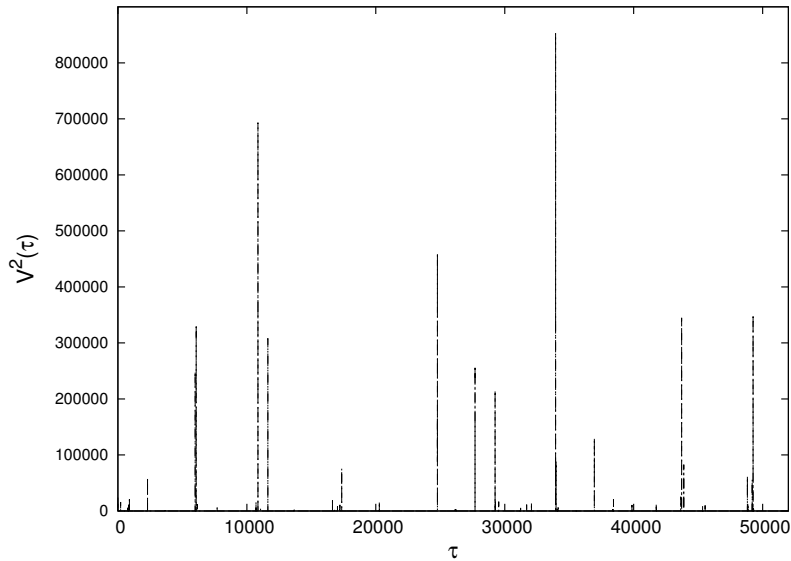


Figure 3.11: The ‘velocity’ $V(\tau)^2$ as function of proper time τ for the chaotic orbit with $\rho = 0.7$.

we first localize the first peak at $\tau = 2296.39$. We then consider the interval $\tau \in [2286, 2306]$ and compare the behaviour of IGEM with that of the ‘exact’ solution. As the ‘exact’ solution, we choose IGEM with the prohibitively small step size $\epsilon = 10^{-4}$. As it would take too much simulation time to calculate until $\tau = 2306$ using $\epsilon = 10^{-4}$, we obtain the ‘accurate’ solution

as follows: We propagate the system until $\tau = 2286$ with IGEM and only then switch to $\epsilon = 10^{-4}$. When we plot the trajectory as given by this accurate solution along with some points of the trajectory given by IGEM, see Fig. 3.12, we realize that the peak coincides with an inflexion point of the trajectory where $f(\mathbf{y})$ becomes almost singular. In other words, the EMRI's light particle behaves like a ball which is thrown upon a wall. Fig. 3.12 shows further

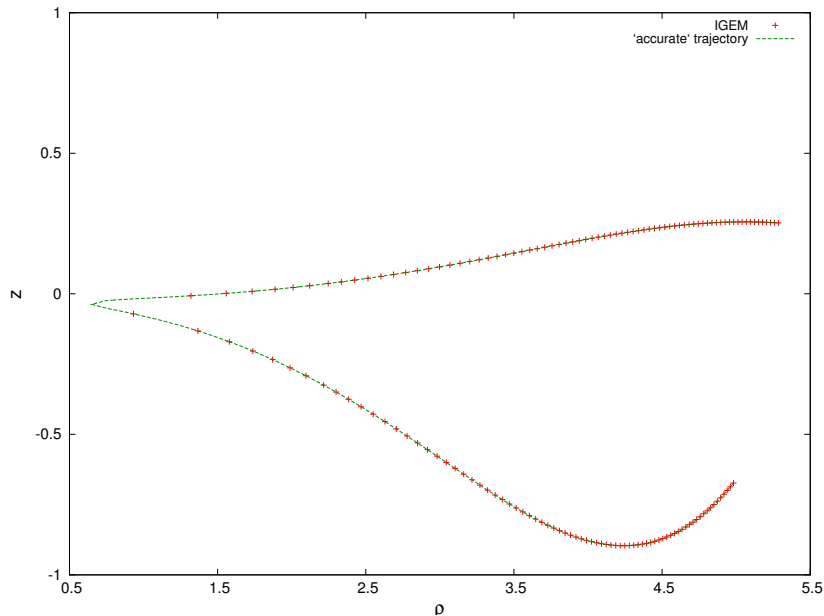


Figure 3.12: The trajectory of the test particle for $\tau \in [2286, 2306]$. The points correspond to the trajectory calculated by IGEM whereas the continuous line gives the ‘accurate’ trajectory. One can see how the test particle bounces back once having arrived at $\rho = 0.66$.

that the solution as calculated by IGEM seems to come back close to the accurate solution soon after the rebound. To state this quantitatively, we plot the difference

$$\text{Dif} = \sqrt{\frac{(\rho_{\text{IGEM}} - \rho_{\text{ac}})^2}{\rho_{\text{ac}}^2} + \frac{(\dot{\rho}_{\text{IGEM}} - \dot{\rho}_{\text{ac}})^2}{\dot{\rho}_{\text{ac}}^2} + \frac{(z_{\text{IGEM}} - z_{\text{ac}})^2}{z_{\text{ac}}^2} + \frac{(\dot{z}_{\text{IGEM}} - \dot{z}_{\text{ac}})^2}{\dot{z}_{\text{ac}}^2}} \quad (3.159)$$

in Fig. 3.13 and see that the solution by IGEM indeed recovers its original trajectory. This behaviour matches perfectly with Fig. 3.10 where we see that the Hamiltonian recovers its previous value right after the inflexion. During the simulation we observed that only for a time range of $3 \cdot 10^{-3}$ out of the whole integration interval of 50000 is the relative error in the Hamiltonian larger than $\Delta H = 10^{-9}$ and, hence, the Hamiltonian is conserved for almost all $\tau \in [0, 50000]$.

One can now hope to circumvent the convergence-problems at the near-singular points by replacing the fixed-point iteration with a Newton-Raphson scheme. However, when trying this one observes that some peaks in the Hamiltonian still remain. What is more, the computational cost increases steeply to $T_{\text{calc}} = 7521.0\text{s}$. The reason for this increase is that during each iteration the complicated derivative of (3.101) has to be calculated. As a consequence, the cost per iteration multiplies while the average number of iterations per integration step decreases

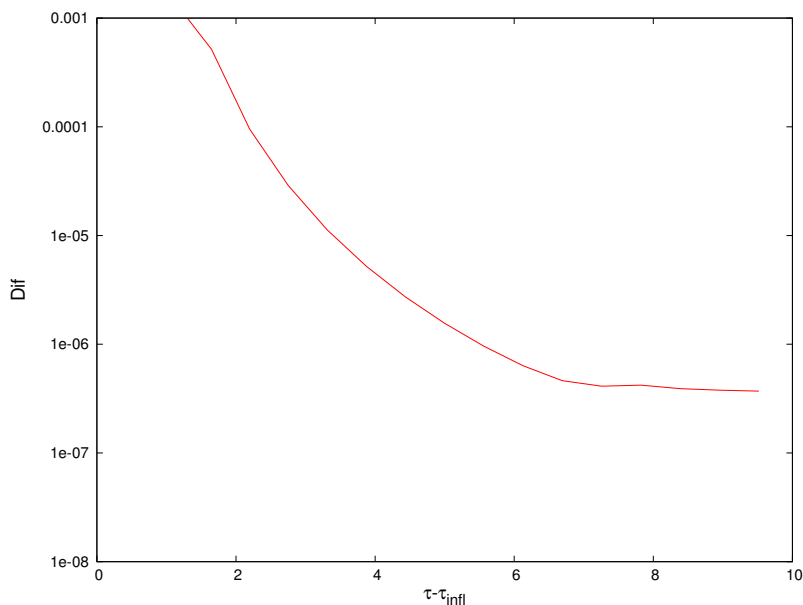


Figure 3.13: Difference between IGEM and the ‘accurate’ solution directly after the first inflexion at $\tau_{\text{infl}} = 2296$.

only slightly from 3.94 to 3.57. We thus observe that for geodesic equations of motions, too, one should renounce on the Newton-Raphson iteration.

As a last point, we want to know which effect our algorithm to calculate the Poincaré sections has on the accuracy. As announced in subsection 2.2.1, it is convenient to take use of the collocation property when calculating sections with a Gauss-Runge-Kutta scheme. Because of this, we applied this algorithm to calculate the Poincaré sections for our three test cases. But we have also seen in subsection 2.2.1 that the collocation error is $\mathcal{O}(h^s)$ and thus the error for the sections can be of order $\mathcal{O}(h^s) + \mathcal{O}(h^{2s})$ for Gauss collocations. Due to the collocation a term larger than the integration error occurs in the error estimate (2.8). To examine whether this is a problem in the EMRI case, we calculate all Poincaré sections for the chaotic test case in the interval $t \in [0, 50000]$ with our IGEM and the help of the collocation algorithm of subsection 2.2.1. We then consider the relative error in the energy for the points on the section

$$\Delta H_{\text{sect}} = \left| \frac{H(\mathbf{y}_{\text{sect}}) - H(\mathbf{y}_0)}{H(\mathbf{y}_0)} \right|, \quad (3.160)$$

and plot it along with the relative error for the trajectory that has already been considered in Fig. 3.10. The result is shown in Fig. 3.14. We observe that the energy at almost all sections is the same as for the points of the trajectory. Thus, the error term of order $\mathcal{O}(h^s)$ does not become noticeable. This is why we recommended the use of the convenient collocation algorithm in subsection 2.2.1.

Having constructed an integrator which suits the special demands of the geodesic equations of motion, we can now turn our attention on binary systems with a less extreme mass ratio.

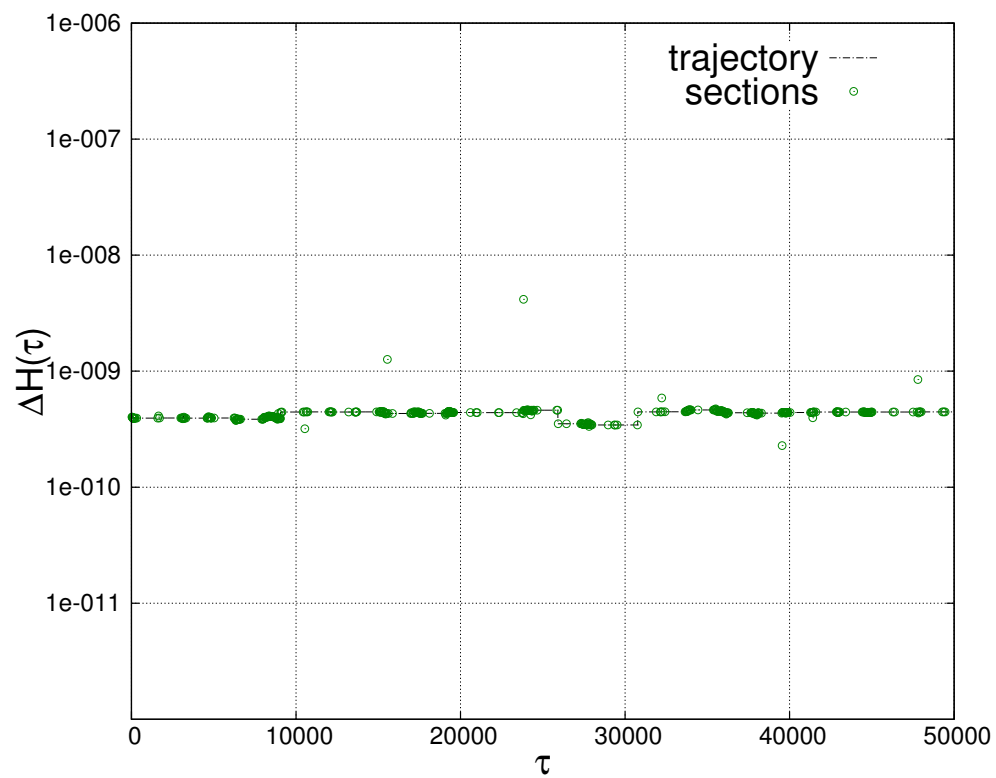


Figure 3.14: For the chaotic test case and $\tau \in [0, 50000]$, the error in the energy at the Poincaré sections obtained via IGEM with $\epsilon = 0.1$ and $s = 4$ and the help of the collocation algorithm is compared with the error along the trajectory for the same integrator.

4. Long-time integration of post-Newtonian equations of motion

In current research concerning a binary of equal or not extremely unequal masses, the post-Newtonian formalism is the state-of-the-art approach. Here, the system is described by a Hamiltonian which is composed of a Newtonian part describing Keplerian orbital motion and smaller perturbative terms. Let us first present this formalism.

4.1. The post-Newtonian formalism

The Einstein equations for a free gravitational field,

$$R_{\mu\nu} - \frac{1}{2}g_{\mu\nu}R = 0, \quad (4.1)$$

were derived as the Euler-Lagrange equations of the coordinate invariant action

$$S = \int \mathcal{L} d^4x = \int d^4x \sqrt{-g} R. \quad (4.2)$$

Here, g is the determinant of the metric $g_{\mu\nu}$, and $R_{\mu\nu}$ is the *Ricci tensor* which is the trace of the Riemann curvature tensor

$$R_{\mu\nu} = R^\lambda_{\mu\lambda\nu} = \partial_\lambda \Gamma^\lambda_{\mu\nu} - \partial_\nu \Gamma^\lambda_{\mu\lambda} + \Gamma^\lambda_{\mu\nu} \Gamma^\alpha_{\lambda\alpha} - \Gamma^\lambda_{\mu\alpha} \Gamma^\alpha_{\nu\lambda}, \quad (4.3)$$

with the Christoffel-symbols

$$\Gamma^\lambda_{\alpha\beta} = \frac{1}{2}g^{\lambda\delta} \left(\frac{\partial g_{\delta\alpha}}{\partial x^\nu} + \frac{\partial g_{\delta\beta}}{\partial x^\alpha} - \frac{\partial g_{\mu\nu}}{\partial x^\delta} \right). \quad (4.4)$$

The *Gauss curvature* R , in turn, is the contraction of the Ricci tensor,

$$R = R^\mu_{\mu}. \quad (4.5)$$

One can now single out the time-like dimension by defining the quantities

$$N := \frac{1}{\sqrt{-g^{00}}}, \quad (4.6)$$

$$N_i := g_{0i}, \quad (4.7)$$

$$\pi^{ij} := \sqrt{-g} \left(\Gamma^0_{\alpha\beta} - g_{\alpha\beta} \Gamma^0_{\gamma\delta} g^{\gamma\delta} \right) g^{i\alpha} g^{j\beta}. \quad (4.8)$$

With these, the Lagrangian in (4.2) can be rewritten in parametrized form

$$\mathcal{L} = \pi^{ij} \partial_t g_{ij} - NR^0 - N_i R^i, \quad R^\mu \stackrel{!}{=} 0, \quad (4.9)$$

where t denotes the parameter and

$$R^\mu = R^\mu(g_{ij}, \pi^{ij}) \quad (4.10)$$

are four constraint equations. The N_i can thus be considered as Lagrange multipliers. Due to the analogy between system (4.9) and a parametrized Lagrangian of N particles in classical mechanics,

$$L = \sum_i^{N+1} p_i \partial_t q_i - NR, \quad R \stackrel{!}{=} 0, \quad (4.11)$$

the π^{ij} are regarded as the canonical conjugate variables to the metric field g_{ij} . Along the lines of classical mechanics, one can derive a Hamiltonian formulation for the system (4.9). With the *eccentric curvature*

$$K_{ij} = \frac{1}{\sqrt{-g}} \left(\frac{1}{2} g_{kl} \pi^{kl} g_{ij} - g_{ik} g_{jl} \pi^{kl} \right), \quad (4.12)$$

the corresponding Hamiltonian reads

$$\mathcal{H} = - \int N(R + K^2 - K_{ij} K^{ij}) - 2N^i (D_j K_i^j - D_i K) \sqrt{-g} d^3x, \quad (4.13)$$

where D_i is the covariant derivative with regard to the 3-metric g_{ij} , e.g., (Arnowitt *et al.*, 1962). The solutions $(\pi^{ij}, g_{ij}, N^\mu)$ of the Hamiltonian equations

$$\frac{\partial \pi^{ij}}{\partial t} = - \frac{\partial H}{\partial g_{ij}}, \quad (4.14)$$

$$\frac{\partial g_{ij}}{\partial t} = \frac{\partial H}{\partial \pi^{ij}}, \quad (4.15)$$

$$\frac{\partial H}{\partial N^\mu} = 0, \quad (4.16)$$

solve the Einstein equations (4.1).

To describe a gravitational field which is caused by matter, a source term has to be added to the field equations. They then read

$$R_{\mu\nu} - \frac{1}{2} g_{\mu\nu} R = \frac{16\pi G}{c^4} T_{\mu\nu}. \quad (4.17)$$

Here, G is the gravitational constant and $T_{\mu\nu}$ is the *stress-energy tensor*. For a fluid with energy-density e , pressure p and fluid velocity u^μ , the stress-energy tensor looks like

$$T^{\mu\nu} = (e + p) u^\mu u^\nu + p g^{\mu\nu}. \quad (4.18)$$

In presence of a source term, the Hamiltonian becomes

$$H = \int d^3x \left[N \left(\frac{(16\pi G)^2}{c^6} \pi^{ij} G_{ijkl} \pi^{kl} - \sqrt{-g} R + \frac{16\pi G}{c^4} \sqrt{-g} n_\mu T^{\mu\nu} n_\nu \right) - N^i \left(2g_{ik} D_j \pi^{kj} - \frac{1}{c\sqrt{-g}} T_i^0 \right) \right] + \frac{c^4}{16\pi G} \oint_\infty d^2s_i (\partial_j g_{ij} - \partial_i g_{jj}), \quad (4.19)$$

with the unit normal vector to the hypersurface n_μ and the three-dimensional contravariant metric

$$G_{ijkl} = \frac{1}{2\sqrt{g}} (g_{ik} g_{jl} + g_{il} g_{jk} - g_{ij} g_{kl}). \quad (4.20)$$

Choosing the mass-density ρ and its canonical conjugate

$$\pi_i = \frac{1}{c\sqrt{-g}} T_i^0 \quad (4.21)$$

as variables for the fluid, the Hamilton equations (4.14) and (4.15) are joined by the equations

$$\frac{\partial \rho}{\partial t} = -\partial_i \left(\frac{\delta H}{\delta \pi_i} \rho \right), \quad (4.22)$$

$$\frac{\partial \pi_i}{\partial t} = -\partial_j \left(\frac{\delta H}{\delta \pi_j} \pi_i \right) - \partial_i \left(\frac{\delta H}{\delta \pi_j} \right) \pi_j - \partial_i \left(\frac{\delta H}{\delta \rho} \right) \rho, \quad (4.23)$$

where δ denotes the Fréchet derivative. Not all the components of the metric tensor are independent. Instead, the whole field can be expressed by means of the transverse, traceless components g_{ij}^{TT} and π^{ijTT} , which satisfy

$$\partial^j g_{ij}^{TT} \stackrel{!}{=} 0, \quad g_{ii}^{TT} \stackrel{!}{=} 0, \quad (4.24)$$

$$\partial_j \pi^{ijTT} \stackrel{!}{=} 0, \quad p^{iiTT} \stackrel{!}{=} 0. \quad (4.25)$$

When modeling a binary of two compact masses, the source variables can be set to be

$$\rho = \sum_{a=1}^2 m_a \delta^3(\mathbf{x} - \mathbf{x}_a(t)), \quad (4.26)$$

$$\pi_i = \sum_{a=1}^2 m_a p_{ai} \delta^3(\mathbf{p} - \mathbf{p}_a(t)). \quad (4.27)$$

The positions \mathbf{x}_a and momenta \mathbf{p}_a satisfy the Hamilton equations

$$\frac{\partial \mathbf{p}_a}{\partial t} = -\nabla_{\mathbf{x}_a} H, \quad (4.28)$$

$$\frac{\partial \mathbf{x}_a}{\partial t} = \nabla_{\mathbf{p}_a} H. \quad (4.29)$$

Alas, the exact form of the Hamiltonian is not known as it depends on the field variables g_{ij}^{TT} and π^{ijTT} which in turn depend on \mathbf{x}_a and \mathbf{p}_a .

The ansatz in the post-Newtonian approach is now to expand the metric $g_{\mu\nu}$ as follows, (Schäfer, 1997):

$$c^2 g_{00} = -c^2 + \sum_{n=0}^{\infty} \frac{1}{c^{2n}} g_{00}^{(n)}(x, \rho, g^{TT}, \pi^{TT}), \quad (4.30)$$

$$c g_{0i} = \sum_{n=0}^{\infty} \frac{1}{c^{2n}} g_{0i}^{(n)}(x, \rho, g^{TT}, \pi^{TT}), \quad (4.31)$$

$$g_{ij} = \delta_{ij} + \sum_{n=0}^{\infty} \frac{1}{c^{2n}} g_{ij}^{(n)}(x, \rho, g^{TT}, \pi^{TT}). \quad (4.32)$$

Until now, it has been possible to express the metric components up to $n = 3$ by means of only the coordinates and momenta of the compact masses, see, e.g., (Jaranowski and Schäfer, 2001). The Hamiltonian of the equations (4.28) and (4.29) is thus approximated as

$$H(\mathbf{p}, \mathbf{x}) = H_N(\mathbf{p}, \mathbf{x}) + H_{1\text{PN}}(\mathbf{p}, \mathbf{x}) + H_{2\text{PN}}(\mathbf{p}, \mathbf{x}) + H_{3\text{PN}}(\mathbf{p}, \mathbf{x}). \quad (4.33)$$

Here, we only consider the center of mass dynamics with $\mathbf{x} = \mathbf{x}_1 - \mathbf{x}_2$ and $\mathbf{p} = \mathbf{p}_1 = -\mathbf{p}_2$, as these are of interest in most applications. $H_{n\text{PN}}$ contains all contribution of the n th-order. The zero-order term $H_N(\mathbf{p}, \mathbf{x})$ is just the Hamiltonian of Newtonian gravitation.

The Hamiltonian (4.33) still misses an important aspect of general relativity. It was derived assuming the compact particles to be point-like. In fact, each object is of finite size. Therefore, the motion of an object around its own axis, i.e., its *spin*, has to be taken into account. The equations of motion of a particle's four-dimensional spin vector S_μ are known to be

$$D_\tau S_\mu = 0, \quad (4.34)$$

where D is the covariant derivative with regard to proper time. The derivative with regard to coordinate time $t = x^0/c$ is then given as

$$\frac{dS_\mu}{dt} = c\Gamma_{\mu\alpha}^\nu S_\nu v^\alpha, \quad (4.35)$$

with

$$v^\mu = \frac{1}{c} \frac{dx^\mu}{dt}. \quad (4.36)$$

Equation (4.35) describes the interaction between a particle's spin and its orbit. With the help of the *spin supplementary condition*,

$$S_\mu u^\mu \stackrel{!}{=} 0 \quad (4.37)$$

(u^μ being the normalized 4-velocity), equation (4.35) can be transformed to yield an equation for the three-dimensional spin

$$\frac{dS_i}{dt} = \epsilon_{ijk} \Omega_j S_k. \quad (4.38)$$

The interaction term Ω_j depends on the position and the momentum of the particle as well as on the gravitational field. Inserting the field's post-Newtonian expansion, one can obtain a *spin-orbit interaction Hamiltonian* H_{SO} , such that equation (4.38) is given as

$$\frac{dS_i}{dt} = \epsilon_{ijk} \frac{\partial H_{\text{SO}}}{\partial S_j} S_k. \quad (4.39)$$

The detailed derivation of the spin-orbit interaction can be found in (Damour *et al.*, 2008). When considering a binary of compact objects, one can similarly derive a *spin-spin interaction Hamiltonian* H_{SS} . Putting everything together, we are able to present the Hamiltonian system of the post-Newtonian approximation in the next section.

4.2. The post-Newtonian equations of motion

The Hamiltonian for a binary system in the center-of-mass frame depends on the positions $\mathbf{x} = \mathbf{x}_2 - \mathbf{x}_1$, the momenta $\mathbf{p} = \mathbf{p}_1 = -\mathbf{p}_2$, and the spins of the two particles \mathbf{S}_1 and \mathbf{S}_2 . It has the form

$$H(\mathbf{p}, \mathbf{x}, \mathbf{S}_1, \mathbf{S}_2) = H_N(\mathbf{p}, \mathbf{x}) + H_{\text{PN}}(\mathbf{p}, \mathbf{x}) + H_{\text{SO}}(\mathbf{p}, \mathbf{x}, \mathbf{S}_1, \mathbf{S}_2) + H_{\text{SS}}(\mathbf{p}, \mathbf{x}, \mathbf{S}_1, \mathbf{S}_2). \quad (4.40)$$

The dynamics of the respective variables are given by

$$\frac{d\mathbf{p}}{dt} = -\nabla_{\mathbf{x}}H, \quad (4.41)$$

$$\frac{d\mathbf{x}}{dt} = \nabla_{\mathbf{p}}H, \quad (4.42)$$

$$\frac{d\mathbf{S}_a}{dt} = (\nabla_{\mathbf{S}_a}H) \times \mathbf{S}_a. \quad (4.43)$$

In most ongoing applications, orbital terms up to the third post-Newtonian order and spin-orbit interactions of first or second order are taken into account. As for the spin-spin contribution, only the leading order is considered as the next term would already be small compared to the 3PN orbital term. As the motion does not depend on the absolute value of the masses but on their ratio, one can w.l.o.g. assume the total mass $m := m_1 + m_2$ to be equal to 1. Using the reduced mass $\mu = m_1 m_2 / m$, $q = \|\mathbf{x}\|$, $\nu = \mu/m$, and the unit vector $\mathbf{n} = \mathbf{x}/q$ and choosing units such that $G = c = 1$, the relevant terms of the orbital Hamiltonian are

$$H_N(\mathbf{p}, \mathbf{x}) = \frac{\mathbf{p}^2}{2\mu} - \frac{\mu}{q}, \quad (4.44)$$

$$H_{1\text{PN}}(\mathbf{p}, \mathbf{x}) = \frac{1}{8\mu^3}(3\nu - 1)(\mathbf{p}^2)^2 - \frac{1}{2\mu^2 q}[(3 + \nu)\mathbf{p}^2 + \nu(\mathbf{np})^2] + \frac{\mu}{2q^2}, \quad (4.45)$$

$$\begin{aligned} H_{2\text{PN}}(\mathbf{p}, \mathbf{x}) &= \frac{1}{16\mu^5}(1 - 5\nu - 5\nu^2)(\mathbf{p}^2)^3 + \frac{1}{8\mu^3 q}[(5 - 20\nu - 3\nu^2)(\mathbf{p}^2)^2 \\ &\quad - 2\nu^2(\mathbf{np})^2\mathbf{p}^2 + 3\nu^2(\mathbf{np})^4] + \dots \\ &\quad + \frac{1}{2\mu q^2}[3\nu(\mathbf{np})^2 + (5 + 8\nu)\mathbf{p}^2] - \frac{(1 + 3\nu)\mu}{4q^3}, \end{aligned} \quad (4.46)$$

$$\begin{aligned} H_{3\text{PN}}(\mathbf{p}, \mathbf{x}) &= \frac{1}{128\mu^7}(-5 + 35\nu - 70\nu^2 + 35\nu^3)(\mathbf{p}^2)^4 + \dots \\ &\quad + \frac{1}{16\mu^5 q}[(-7 + 42\nu - 53\nu^2 - 5\nu^3)(\mathbf{p}^2)^3 + (2 - 3\nu)\nu^2(\mathbf{np})^2(\mathbf{p}^2)^2 \\ &\quad + 3(1 - \nu)\nu^2(\mathbf{np})^4\mathbf{p}^2 - 5\nu^3(\mathbf{np})^6] + \dots \\ &\quad + \frac{1}{16\mu^3 q^2}\left[(-27 + 136\nu + 109\nu^2)(\mathbf{p}^2)^2 + \dots \right. \\ &\quad \left. + (17 + 30\nu)\nu(\mathbf{np})^2\mathbf{p}^2 + \frac{3}{4}(5 + 43\nu)\nu(\mathbf{np})^4\right] + \dots \\ &\quad + \frac{1}{\mu q^3}\left\{\left[-\frac{25}{8} + \left(\frac{\pi^2}{64} - \frac{335}{48}\right)\nu - \frac{23}{8}\nu^2\right]\mathbf{p}^2 + \dots\right\} \end{aligned}$$

$$\begin{aligned}
& + \left(-\frac{85}{16} - \frac{3\pi^2}{64} - \frac{7\nu}{4} \right) \nu(\mathbf{np})^2 \Big\} + \dots \\
& + \frac{\mu}{q^4} \left[\frac{1}{8} + \left(\frac{109}{12} - \frac{21\pi^2}{32} \right) \nu \right].
\end{aligned} \tag{4.47}$$

The leading order spin-orbit coupling can be expressed by means of the orbital angular momentum $\mathbf{L} = \mathbf{x} \times \mathbf{p}$ and the effective spin

$$\mathbf{S}_{\text{eff}} = \left(1 + \frac{3m_2}{4m_1} \right) \mathbf{S}_1 + \left(1 + \frac{3m_1}{4m_2} \right) \mathbf{S}_2 \tag{4.48}$$

as

$$H_{\text{SO}}(\mathbf{p}, \mathbf{x}, \mathbf{S}_1, \mathbf{S}_2) = 2 \frac{\mathbf{S}_{\text{eff}} \cdot \mathbf{L}}{q^3}. \tag{4.49}$$

The spin-spin interaction is composed of three terms:

$$H_{\text{SS}}(\mathbf{p}, \mathbf{x}, \mathbf{S}_1, \mathbf{S}_2) = H_{S_1 S_2}(\mathbf{p}, \mathbf{x}, \mathbf{S}_1, \mathbf{S}_2) + H_{S_1 S_1}(\mathbf{p}, \mathbf{x}, \mathbf{S}_1) + H_{S_2 S_2}(\mathbf{p}, \mathbf{x}, \mathbf{S}_2), \tag{4.50}$$

where the individual contributions are given as

$$H_{S_1 S_2}(\mathbf{p}, \mathbf{x}, \mathbf{S}_1, \mathbf{S}_2) = \frac{1}{q^3} [3(\mathbf{S}_1 \mathbf{n})(\mathbf{S}_2 \mathbf{n}) - \mathbf{S}_1 \mathbf{S}_2], \tag{4.51}$$

$$H_{S_1 S_1}(\mathbf{p}, \mathbf{x}, \mathbf{S}_1) = \frac{m_2}{2m_1 q^3} [3(\mathbf{S}_1 \mathbf{n})^2 - \mathbf{S}_1 \mathbf{S}_1], \tag{4.52}$$

$$H_{S_2 S_2}(\mathbf{p}, \mathbf{x}, \mathbf{S}_2) = \frac{m_1}{2m_2 q^3} [3(\mathbf{S}_2 \mathbf{n})^2 - \mathbf{S}_2 \mathbf{S}_2]. \tag{4.53}$$

The equations of motion corresponding to the just presented Hamiltonian are given in appendix [B](#). There is obviously no possibility to solve them analytically. Numerical tools for their solution are necessary. In view of this, we now discuss the numerical properties of the post-Newtonian equations.

4.3. Numerical properties of the PN equations of motion

The equations (4.41)-(4.43) are a Poisson-system for $\mathbf{y} = (\mathbf{p}, \mathbf{x}, \mathbf{S}_1, \mathbf{S}_2)^T$, i.e.,

$$\frac{d\mathbf{y}}{dt} = B(\mathbf{y}) \nabla H, \tag{4.54}$$

with

$$B(\mathbf{y}) = \begin{pmatrix} 0 & -\mathcal{I} & 0 & 0 \\ \mathcal{I} & 0 & 0 & 0 \\ 0 & 0 & B_1(\mathbf{y}) & 0 \\ 0 & 0 & 0 & B_2(\mathbf{y}) \end{pmatrix}, \tag{4.55}$$

$$B_1(\mathbf{y}) = \begin{pmatrix} 0 & -S_{1z} & S_{1y} \\ S_{1z} & 0 & -S_{1x} \\ -S_{1y} & S_{1x} & 0 \end{pmatrix}, \quad B_2(\mathbf{y}) = \begin{pmatrix} 0 & -S_{2z} & S_{2y} \\ S_{2z} & 0 & -S_{2x} \\ -S_{2y} & S_{2x} & 0 \end{pmatrix}. \tag{4.56}$$

Thus, one should preferably apply a numerical scheme which preserves this special structure. In this case, one can expect a benevolent long-time behaviour similar to the symplectic case, e.g., (Hairer *et al.*, 2006).

The post-Newtonian system can be considered as a perturbed Kepler problem, the corrections to the classical motion scaling with $1/c^2$. In the units $G = c = 1$ this scaling is encoded in the higher orders of $1/q$ or \mathbf{p}^2 in the post-Newtonian terms. As $q > 1$ and $\mathbf{p}^2 < 1$ in most circumstances, one has a Hamiltonian of the form

$$H = H_N + \delta\tilde{H}, \quad \delta \ll 1, \quad (4.57)$$

where the ‘larger’ part can be solved analytically. But still, when the two compact objects are close together, the post-Newtonian corrections can become relatively large.

As a last point, we notice that the Hamiltonian is non-separable as the variables are coupled in the non-classical contributions. A structure preserving integration will thus inevitably involve implicit methods.

We now present two ways to construct an integrator which copes with all these requirements. We start with an idea of Lubich *et al.* (2010).

4.4. Poisson integrator for post-Newtonian equations

The idea is to calculate one by one the flows φ_N , Φ_{PN} and $\Phi_{SS,SO}$ corresponding to the Hamiltonian H_N , H_{PN} and $H_{SO,SS}$, respectively, and then construct the numerical solution Φ_h as a suitable composition of the single integrators. In this approach, φ_N can be obtained exactly. To solve the orbital post-Newtonian contribution, one uses a symplectic scheme, the order of which does not need to be high because a simple splitting does not have order higher than two anyway. The Hamiltonian $H_{SO,SS}$ is split into parts which can each be solved exactly. This was the major achievement of Lubich *et al.* (2010). As a composition of exact and symplectic flows, the overall integrator will then preserve the structure (4.54). Let us now show briefly how to obtain $\Phi_{SS,SO}$.

First, one decomposes the spin-orbit Hamiltonian as

$$H_{SO} = H_{SO}^x + H_{SO}^y + H_{SO}^z, \quad (4.58)$$

with

$$H_{SO}^i = \frac{2}{q^3} (\mathbf{S}_{\text{eff}} \cdot \hat{\mathbf{e}}_i) (\mathbf{L} \cdot \hat{\mathbf{e}}_i). \quad (4.59)$$

The equations of motion corresponding to H_{SO}^i are

$$\frac{d\mathbf{p}}{dt} = \frac{2\mathbf{S}_{\text{eff}} \cdot \hat{\mathbf{e}}_i}{q^3} \hat{\mathbf{e}}_i \times \mathbf{p} + 3H_{SO}^i \frac{\mathbf{x}}{q^2}, \quad (4.60)$$

$$\frac{d\mathbf{x}}{dt} = \frac{2\mathbf{S}_{\text{eff}} \cdot \hat{\mathbf{e}}_i}{q^3} \hat{\mathbf{e}}_i \times \mathbf{x}, \quad (4.61)$$

$$\frac{d\mathbf{S}_1}{dt} = \left(1 + \frac{3m_2}{4m_1}\right) \frac{2\mathbf{L} \cdot \hat{\mathbf{e}}_i}{q^3} \hat{\mathbf{e}}_i \times \mathbf{S}_1, \quad (4.62)$$

$$\frac{d\mathbf{S}_2}{dt} = \left(1 + \frac{3m_1}{4m_2}\right) \frac{2c_a \mathbf{L} \cdot \hat{\mathbf{e}}_i}{q^3} \hat{\mathbf{e}}_i \times \mathbf{S}_2. \quad (4.63)$$

Taking the inner product of (4.61) with \mathbf{x} yields

$$0 = \frac{d\mathbf{p}}{dt} \cdot \mathbf{x} = \frac{1}{2} \frac{dq^2}{dt}. \quad (4.64)$$

Similarly, one can deduce

$$\frac{d\mathbf{S}_a}{dt} \cdot \hat{\mathbf{e}}_i = 0. \quad (4.65)$$

This implies that $\mathbf{S}_{\text{eff}} \cdot \hat{\mathbf{e}}_i$ and q are constant. We now observe that equations of the form

$$\frac{d\mathbf{a}}{dt} = \boldsymbol{\Omega} \times \mathbf{a}, \quad (4.66)$$

where $\boldsymbol{\Omega}$ is a constant vector, are solved by a simple rotation, i.e.,

$$\mathbf{a}(t) = \text{rot}(\boldsymbol{\Omega}, t)\mathbf{a}(0). \quad (4.67)$$

Here, the rotation operator is defined via

$$\text{rot}(\boldsymbol{\Omega}, t)\mathbf{a}(0) := \mathbf{a}(0) + \frac{\sin(\|\boldsymbol{\Omega}\|t)}{\|\boldsymbol{\Omega}\|} \boldsymbol{\Omega} \times \mathbf{a}(0) + 2 \left(\frac{\sin\left(\frac{\|\boldsymbol{\Omega}\|t}{2}\right)}{\|\boldsymbol{\Omega}\|} \right)^2 \boldsymbol{\Omega} \times \boldsymbol{\Omega} \times \mathbf{a}(0). \quad (4.68)$$

The constancy of $\mathbf{S}_{\text{eff}} \cdot \hat{\mathbf{e}}_i$ and q combined with (4.67) immediately gives

$$\mathbf{x}(t) = \text{rot}\left(\frac{2\mathbf{S}_{\text{eff}} \cdot \hat{\mathbf{e}}_i}{q^3} \hat{\mathbf{e}}_i, t\right) \mathbf{x}(0) \quad (4.69)$$

and

$$\mathbf{p}(t) = \text{rot}\left(\frac{2\mathbf{S}_{\text{eff}} \cdot \hat{\mathbf{e}}_i}{q^3} \hat{\mathbf{e}}_i, t\right) \left(\mathbf{p}(0) + \frac{3tH_{\text{SO}}^i}{q^2} \mathbf{x}(0)\right). \quad (4.70)$$

Furthermore, equations (4.60) and (4.61) imply that the equation of motion for the angular momentum \mathbf{L} is also of the form (4.67). Therefore, its length is conserved and, as a consequence, the equations for the spins (4.62) and (4.63) are again of the type (4.67). Thus, the motion of the spins is given by

$$\mathbf{S}_1(t) = \text{rot}\left(\left(1 + \frac{3m_2}{4m_1}\right) \frac{2\mathbf{L} \cdot \hat{\mathbf{e}}_i}{q^3} \hat{\mathbf{e}}_i, t\right) \mathbf{S}_1(0), \quad (4.71)$$

$$\mathbf{S}_2(t) = \text{rot}\left(\left(1 + \frac{3m_1}{4m_2}\right) \frac{2\mathbf{L} \cdot \hat{\mathbf{e}}_i}{q^3} \hat{\mathbf{e}}_i, t\right) \mathbf{S}_2(0). \quad (4.72)$$

In the same way, one can split the spin-spin Hamiltonian as

$$H_{\text{SS}} = H_{\text{SS}}^1 + H_{\text{SS}}^2 + H_{\text{SS}}^3 + H_{\text{SS}}^4, \quad (4.73)$$

with

$$H_{\text{SS}}^1 = -\frac{\mathbf{S}_1 \cdot \mathbf{S}_2}{q^3}, \quad (4.74)$$

$$H_{\text{SS}}^2 = -\frac{\mathbf{S}_1 \cdot \mathbf{S}_1}{2q^3} - \frac{\mathbf{S}_2 \cdot \mathbf{S}_2}{2q^3}, \quad (4.75)$$

$$H_{\text{SS}}^3 = \frac{3(\mathbf{S}_1 \cdot \mathbf{n})(\mathbf{S}_2 \cdot \mathbf{n})}{q^3}, \quad (4.76)$$

$$H_{\text{SS}}^4 = \frac{3(\mathbf{S}_1 \cdot \mathbf{n})(\mathbf{S}_1 \cdot \mathbf{n})}{2q^3} + \frac{3(\mathbf{S}_2 \cdot \mathbf{n})(\mathbf{S}_2 \cdot \mathbf{n})}{2q^3}. \quad (4.77)$$

The corresponding flows Φ_{SS}^i are derived with the same methods as in the spin-orbit case. The result is given in appendix C. Putting everything together, one arrives at

$$\Phi_{\text{SO,SS}} = \varphi_{\text{SO}}^x \circ \varphi_{\text{SO}}^y \circ \varphi_{\text{SO}}^z \circ \varphi_{\text{SS}}^1 \circ \varphi_{\text{SS}}^2 \circ \varphi_{\text{SS}}^3 \circ \varphi_{\text{SS}}^4. \quad (4.78)$$

The sequence of the individual flows is not fixed and can be changed ad libitum.

Right after the first, we want to present another possibility to obtain structure preserving algorithms for the post-Newtonian formalism.

4.5. Transformation to symplectic form

The *Darboux-Lie theorem* states that for every Poisson system (4.54), one can find a transformation

$$\mathbf{z} = \Psi(\mathbf{y}), \quad (4.79)$$

such that the system in the coordinates \mathbf{z} is locally canonical. There are two properties of the post-Newtonian equations which enable us to find such a transformation in this case. Firstly, the positions and momenta are already in canonical form. Thus, a transformation (4.79) only has to focus on the spin coordinates. Secondly, by multiplying the equations of motions of the spins (4.43) with the respective spin \mathbf{S}_a , we see that

$$\frac{1}{2} \frac{d\|\mathbf{S}_a\|}{dt} = \frac{d\mathbf{S}_a}{dt} \cdot \mathbf{S}_a = 0, \quad (4.80)$$

i.e., the length of the individual spins is a first integral. These two observations make it surprisingly easy to obtain the transformation to symplectic form.

From the constancy of the spin-length we see that two spin variables are redundant. The post-Newtonian system can therefore be described by $N = 10$ variables. Because of this, [Wu and Xie \(2010\)](#) proposed the use of cylindrical coordinates for the spins:

$$\mathbf{S}_a = m_a^2 \chi_a \begin{pmatrix} \rho_a \cos(\xi_a) \\ \rho_a \sin(\xi_a) \\ \xi_a \end{pmatrix}, \quad (4.81)$$

where χ_a relates the length of an object's spin to the square of its mass. The conservation of the spin-length allows for the elimination of one of the variables (ρ_a, ϕ_a, ξ_a) . Therefore, we can express ρ_a in terms of ξ_a as

$$\rho_a = \sqrt{1 - \xi_a^2}, \quad (4.82)$$

whereby the spin and thus the Hamiltonian only depend on ϕ_a and ξ_a . In order to deduce the equations of motion for the two independent variables, we observe that the following equalities hold true:

$$\frac{\partial H}{\partial \phi_a} = \frac{\partial H}{\partial S_{ax}} \frac{\partial S_{ax}}{\partial \phi_a} + \frac{\partial H}{\partial S_{ay}} \frac{\partial S_{ay}}{\partial \phi_a}, \quad (4.83)$$

$$\frac{\partial H}{\partial \xi_a} = \frac{\partial H}{\partial S_{ax}} \frac{\partial S_{ax}}{\partial \xi_a} + \frac{\partial H}{\partial S_{ay}} \frac{\partial S_{ay}}{\partial \xi_a} + \frac{\partial H}{\partial S_{az}} \frac{\partial S_{az}}{\partial \xi_a}, \quad (4.84)$$

$$\frac{\partial S_{ax}}{\partial \phi_a} = -\rho_a \sin(\phi_a) = -S_{ay}, \quad (4.85)$$

$$\frac{\partial S_{ay}}{\partial \phi_a} = \rho_a \cos(\phi_a) = S_{ax}, \quad (4.86)$$

$$S_{az} = \chi_a m_a^2 \xi_a. \quad (4.87)$$

For the sake of shorter notation, we assume w.l.o.g. that $\chi_a m_a^2 = 1$ until the end of this section. Due to relation (4.87), we have

$$\frac{d\xi_a}{dt} = \frac{dS_{az}}{dt} = \frac{\partial H}{\partial S_{ax}} S_{ay} - \frac{\partial H}{\partial S_{ay}} S_{ax}, \quad (4.88)$$

where the second equality is simply the equation of motion for the z -component of the spin. Substituting S_{ax} and S_{ay} with the help of equations (4.85) and (4.86), and then applying (4.83) we get

$$\frac{d\xi_a}{dt} = -\frac{\partial H}{\partial S_{ax}} \frac{\partial S_{ax}}{\partial \phi_a} + \frac{\partial H}{\partial S_{ay}} \frac{\partial S_{ay}}{\partial \phi_a} = -\frac{\partial H}{\partial \phi_a}. \quad (4.89)$$

We now consider the time-derivatives of the x - and y - components. Taking into account the equations of motion for these components, the derivatives with regard to time are

$$\frac{\partial H}{\partial S_{ay}} S_{az} - \frac{\partial H}{\partial S_{az}} S_{ay} = \frac{dS_{ax}}{dt} = \frac{\partial S_{ax}}{\partial \xi_a} \frac{d\xi_a}{dt} + \frac{\partial S_{ax}}{\partial \phi_a} \frac{d\phi_a}{dt}, \quad (4.90)$$

$$\frac{\partial H}{\partial S_{az}} S_{ax} - \frac{\partial H}{\partial S_{ax}} S_{az} = \frac{dS_{ay}}{dt} = \frac{\partial S_{ay}}{\partial \xi_a} \frac{d\xi_a}{dt} + \frac{\partial S_{ay}}{\partial \phi_a} \frac{d\phi_a}{dt}. \quad (4.91)$$

We can multiply the first equation with $\partial S_{ay}/\partial \xi_a$ and the second with $\partial S_{ax}/\partial \xi_a$ and subtract the two equations. This leads to

$$\begin{aligned} \left(\frac{\partial S_{ax}}{\partial \phi_a} \frac{\partial S_{ay}}{\partial \xi_a} - \frac{\partial S_{ay}}{\partial \phi_a} \frac{\partial S_{ax}}{\partial \xi_a} \right) \frac{d\phi_a}{dt} &= \frac{\partial H}{\partial S_{ay}} \frac{\partial S_{ay}}{\partial \xi_a} S_{az} - \frac{\partial H}{\partial S_{az}} \frac{\partial S_{ay}}{\partial \xi_a} S_{ay} - \dots \\ &\quad - \frac{\partial H}{\partial S_{ay}} S_{az} \frac{\partial S_{ax}}{\partial \xi_a} S_{ax} + \frac{\partial H}{\partial S_{ax}} \frac{\partial S_{ax}}{\partial \xi_a} S_{az}. \end{aligned} \quad (4.92)$$

Calculating the partial derivatives of the spin components with regard to the new variables on the left hand side and some of the partial derivatives on the right hand side, equation (4.92) becomes

$$\xi_a \frac{d\phi_a}{dt} = \frac{\partial H}{\partial S_{ay}} \frac{\partial S_{ay}}{\partial \xi_a} \xi_a + \frac{\partial H}{\partial S_{az}} \xi_a + \frac{\partial H}{\partial S_{ax}} \frac{\partial S_{ax}}{\partial \xi_a} \xi_a. \quad (4.93)$$

Keeping in mind that $\partial S_{az}/\partial \xi_a = 1$ and then taking use of relation (4.84), we arrive at

$$\frac{d\phi_a}{dt} = \frac{\partial H}{\partial \xi_a}. \quad (4.94)$$

Thus, the post-Newtonian equations for the ten independent variables $(\mathbf{p}, \xi_a, \mathbf{x}, \phi_a)$ read

$$\frac{d}{dt} \begin{pmatrix} \mathbf{p} \\ \xi_1 \\ \xi_2 \\ \mathbf{x} \\ \phi_1 \\ \phi_2 \end{pmatrix} = \begin{pmatrix} 0 & -\mathcal{I} \\ \mathcal{I} & 0 \end{pmatrix} \begin{pmatrix} \nabla_{\mathbf{p}} \\ \partial_{\xi_1} \\ \partial_{\xi_2} \\ \nabla_{\mathbf{x}} \\ \partial_{\phi_1} \\ \partial_{\phi_2} \end{pmatrix} H. \quad (4.95)$$

Sadly, the proof of symplecticity in the new coordinates given by [Wu and Xie \(2010\)](#) is wrong. But as has been shown by the last few lines, the system is indeed symplectic. What is more, the transformation is defined globally as it only consists in expressing the spins with constant length via cylindrical coordinates. As a consequence, a structure preserving algorithm for the post-Newtonian equations can be obtained by carrying out the global transformation to canonical form and then applying a symplectic integrator.

Next, we take use of the the last two sections' theory and present some integrators.

4.6. Structure preserving integrators for post-Newtonian equations of motion

In the last two sections, the groundwork for a structure preserving integration was laid down. Now, we consider another property of section 4.3, namely the shape of the Hamiltonian (4.57). This gives a natural splitting of the Hamiltonian into two parts. It is well known, e.g., ([Liao, 1997](#)), that an integrator which is splitted in this natural way has a smaller local error than a comparable scheme. More precisely, when comparing the splitted integrator

$$\Phi_{\text{split},h} := \varphi_{N,\frac{h}{2}} \circ \Phi_{\delta\tilde{H},h} \circ \varphi_{N,\frac{h}{2}} \quad (4.96)$$

with the scheme $\Phi_{H,h}$, where Φ_h is the same second order scheme for both methods, the corresponding local errors are

$$\|\varphi_{H,h} - \Phi_{H,h}\| = \mathcal{O}(h^3) \quad (4.97)$$

and

$$\|\varphi_{H,h} - \Phi_{\text{split},h}\| = \mathcal{O}(\delta h^3). \quad (4.98)$$

Having thus obtained a second order scheme with a small truncation error, one can lift the scheme to higher order by apt composition. In this work, we consider 4th order methods given by the state-of-the art *Suzuki composition*

$$\Phi_{4\text{th},h} = \Phi_{\text{split},\alpha h} \circ \Phi_{\text{split},\alpha h} \circ \Phi_{\text{split},\beta h} \circ \Phi_{\text{split},\alpha h} \circ \Phi_{\text{split},\alpha h}, \quad (4.99)$$

with

$$\alpha = \frac{1}{4 - 4^{1/3}}, \quad (4.100)$$

$$\beta = \frac{4^{1/3}}{4 - 4^{1/3}}. \quad (4.101)$$

Concerning the splitted, second order integrator $\Phi_{\text{split},h}$, we notice that the error estimate (4.98) still holds, when we replace the scheme by

$$\tilde{\Phi}_{\text{split},h} = \Phi_{\delta\tilde{H},\frac{h}{2}} \circ \varphi_{N,h} \circ \Phi_{\delta\tilde{H},\frac{h}{2}}. \quad (4.102)$$

There are two reasons why one should expect $\Phi_{\text{split},h}$ to be superior to $\tilde{\Phi}_{\text{split},h}$:

- At every composition in (4.99), one can combine

$$\dots \circ \varphi_{N,\gamma_1 h} \circ \varphi_{N,\gamma_2 h} \circ \dots = \dots \circ \varphi_{N,(\gamma_1+\gamma_2)h} \circ \dots \quad (4.103)$$

due to the group property of the exact flow,

$$\varphi_h \circ \varphi_s = \varphi_{h+s}. \quad (4.104)$$

When employing $\tilde{\Phi}_{\text{split},h}$ instead, one cannot ‘merge’ parts in the Suzuki composition without catching more errors.

- The post-Newtonian terms in the Hamiltonian are non-separable, as has already been stated in 4.3. Therefore, the numerical flow $\Phi_{\delta\tilde{H},h}$ corresponding to the non-Newtonian Hamiltonian requires the solution of implicit equations. This yields computational cost and we can expect the calculation of $\Phi_{\delta\tilde{H},h}$ to be more expensive than the calculation of $\varphi_{N,h}$. Thus, the scheme where $\Phi_{\delta\tilde{H},h}$ has to be calculated less often, i.e., the scheme using compositions of $\Phi_{\text{split},h}$, should be more efficient.

On the other hand, the splitting $\tilde{\Phi}_{\text{split},h}$ uses half as large a step size in the approximation $\Phi_{\delta\tilde{H},\frac{h}{2}}$. This gives a smaller error in each application of $\Phi_{\delta\tilde{H},h}$. Furthermore, when using a smaller step size in the implicit method, the number of iterations per application of $\Phi_{\delta\tilde{H},h}$ should be smaller, thus partly compensating for the extra numerical cost caused by the form of $\tilde{\Phi}_{\text{split},h}$.

Using the ideas for sections 4.4 and 4.5, as well as Suzuki’s composition (4.99), we explicitly construct four different integrators. We will use both the splitting $\Phi_{\text{split},h}$ and its alternative $\tilde{\Phi}_{\text{split},h}$:

- For the first integrator, we combine the ideas of 4.4 with the splitting (4.96). We numerically calculate the flow given by the non-classical corrections as

$$\Phi_{\delta\tilde{H},h} = \Phi_{\text{SO,SS},\frac{h}{2}}^* \circ \Phi_{\text{PN},h} \circ \Phi_{\text{SO,SS},\frac{h}{2}}, \quad (4.105)$$

with $\Phi_{\text{SO,SS}}$ as given in (4.78) and its adjoint

$$\Phi_{\text{SO,SS}}^* = \Phi_{\text{SS}}^4 \circ \Phi_{\text{SS}}^3 \circ \Phi_{\text{SS}}^2 \circ \Phi_{\text{SS}}^1 \circ \Phi_{\text{SO}}^z \circ \Phi_{\text{SO}}^y \circ \Phi_{\text{SO}}^x. \quad (4.106)$$

The orbital part Φ_{PN} is solved by the symplectic 2nd order *implicit midpoint rule*

$$\mathbf{y}_{n+1} = \mathbf{y}_n + hf \left(\frac{1}{2}(\mathbf{y}_n + \mathbf{y}_{n+1}) \right). \quad (4.107)$$

With this, the splitted integrator $\Phi_{\text{split},h}$ is symplectic, time-reversible and of second order. When applying the Suzuki composition, we merge terms as in (4.109). The integrator obtained in this way is called *PoissonI* in the following.

- We also construct a Poisson integrator with the splitting (4.102). Again, we solve the orbital post-Newtonian contributions with the help of the implicit midpoint rule and set

$$\tilde{\Phi}_{\text{split},h} = \Phi_{\text{SO,SS},\frac{h}{2}}^* \circ \Phi_{\text{PN},\frac{h}{2}} \circ \varphi_{\text{N},h} \circ \Phi_{\text{PN},\frac{h}{2}} \circ \Phi_{\text{SO,SS},\frac{h}{2}}. \quad (4.108)$$

In Suzuki’s composition, we can merge

$$\dots \circ \varphi_{\text{SS},\gamma_1 h}^4 \circ \varphi_{\text{SS},\gamma_2 h}^4 \circ \dots = \dots \circ \varphi_{\text{SS},(\gamma_1+\gamma_2)h}^4 \circ \dots. \quad (4.109)$$

This scheme will be referred to as *PoissonII*.

- The next scheme, *SympI*, uses the transformation of section 4.5. Thanks to this transformation, one can solve all the relativistic contributions at once by applying the implicit midpoint rule to the whole Hamiltonian $\delta\tilde{H}$. This gives a second order flow Φ_{rel} . In the case of SympI, we split in the way

$$\Phi_{\text{split},h} = \varphi_{\text{N},\frac{h}{2}} \circ \Phi_{\text{rel},h} \circ \varphi_{\text{N},\frac{h}{2}}. \quad (4.110)$$

which allows us to merge parts of the integration during the composition in the way (4.109).

- As a last example, we split the canonical system as

$$\tilde{\Phi}_{\text{split},h} = \Phi_{\text{rel},\frac{h}{2}} \circ \varphi_{\text{N},h} \circ \Phi_{\text{rel},\frac{h}{2}}, \quad (4.111)$$

where Φ_{rel} again accounts for all non-classical contributions calculated via the implicit midpoint rule. Once more, we enhance the order with the help of composition (4.99). Hereinafter, this scheme will be denoted by *SympII*.

Besides the splitting methods, we can ignore property (4.57) and apply an implicit Gauss-Runge-Kutta scheme to the system in symplectic form $H(\mathbf{p}, \xi_1, \xi_2, \mathbf{x}, \phi_1, \phi_2)$. Gauss-Runge-Kutta schemes have been introduced in section 3.4. Here, we will test schemes with $s = 2$, $s = 3$, and $s = 4$ inner stages. The corresponding integrators will be denoted by *Gauss2*, *Gauss3*, *Gauss4*, respectively.

Before testing and comparing these schemes, we want to expose an interesting fact concerning the flow φ_{N} in the next section.

4.7. Calculating the ‘exact’ Kepler-flow

As is well known, the system described by the Hamiltonian of a classical two-body problem (4.44) can be solved analytically. But, the analytical solution is implicit as a function of the time-parameter t . If we consider, without loss of generality, the trajectory to be in the x, y -plane, the solution in cylindrical coordinates (ρ, ϕ) with the stationary mass in the origin is given as

$$\rho(\phi(t)) = \frac{L_z^2}{\mu^2 [1 + e \cos(\phi(t) - \phi_{\text{per}})]}, \quad (4.112)$$

$$\int_{\phi(0)}^{\phi(t)} d\tilde{\phi} \frac{1}{1 + e \cos(\tilde{\phi} - \phi_{\text{per}})} = \frac{\mu^3}{L_z^3} t. \quad (4.113)$$

Here, ϕ_{per} is the angle at the periapsis, L_z is the conserved z -component of the angular momentum and e is the eccentricity,

$$e = \sqrt{1 + \frac{2HL_z^2}{\mu^3}}. \quad (4.114)$$

We clearly observe the implicitness in equation (4.113). Thus, every time we want to calculate the analytic Kepler-flow for the integrators in 4.6, we have to iteratively solve an implicit equation. The smaller the step size, the more often we need to apply an iteration. But as we have already seen in section 3.8, round-off errors can occur which can accumulate during long-time integrations.

Having said this, we can remember the separability of the Kepler Hamiltonian and apply the 2nd order, explicit, symplectic and reversible *Störmer-Verlet* Φ_{SV} :

$$\tilde{\mathbf{p}} = \mathbf{p}_n - \frac{h\mu}{2q^3} \mathbf{x}_n \quad (4.115)$$

$$\mathbf{x}_{n+1} = \mathbf{x}_n + \frac{h}{\mu} \tilde{\mathbf{p}} \quad (4.116)$$

$$\mathbf{p}_{n+1} = \tilde{\mathbf{p}} - \frac{h\mu}{2q^3} \mathbf{x}_{n+1}. \quad (4.117)$$

Lifting the order with the composition

$$\begin{aligned} \Phi_{\text{Kep},h} &= \Phi_{\text{SV},\alpha_1 h} \circ \Phi_{\text{SV},\alpha_2 h} \circ \Phi_{\text{SV},\alpha_3 h} \circ \Phi_{\text{SV},\alpha_4 h} \circ \Phi_{\text{SV},\alpha_5 h} \circ \Phi_{\text{SV},\alpha_6 h} \circ \Phi_{\text{SV},\alpha_7 h} \circ \dots \\ &\circ \Phi_{\text{SV},\alpha_8 h} \circ \Phi_{\text{SV},\alpha_7 h} \circ \Phi_{\text{SV},\alpha_6 h} \circ \Phi_{\text{SV},\alpha_5 h} \circ \Phi_{\text{SV},\alpha_4 h} \circ \Phi_{\text{SV},\alpha_3 h} \circ \Phi_{\text{SV},\alpha_2 h} \circ \Phi_{\text{SV},\alpha_1 h}, \end{aligned} \quad (4.118)$$

$$\begin{aligned} \alpha_1 &= 0.741\,670\,364\,350\,612\,953\,448\,227\,80, \\ \alpha_2 &= -0.409\,100\,825\,800\,031\,593\,997\,300\,10, \\ \alpha_3 &= 0.190\,754\,710\,296\,238\,379\,953\,876\,26, \\ \alpha_4 &= -0.573\,862\,471\,116\,082\,266\,656\,387\,73, \\ \alpha_5 &= 0.299\,064\,181\,303\,655\,923\,844\,463\,54, \\ \alpha_6 &= 0.334\,624\,918\,245\,298\,183\,784\,957\,98, \\ \alpha_7 &= 0.315\,293\,092\,396\,766\,596\,632\,056\,66, \\ \alpha_8 &= -0.796\,887\,939\,352\,916\,354\,019\,788\,84, \end{aligned}$$

one obtains a fast and accurate method of order 8 to calculate the flow of the two-body problem, see, e.g., (Hairer *et al.*, 2006). When using compensated summation, there should be no rounding errors during the numerical integration, as was argued in 3.8. We note in passing that one can merge the steps (4.115) and (4.117), thus saving computational effort. But we will not do so in the test below as this merger is not possible in the post-Newtonian splitting. When the analytical solution is divided into many steps, as is the case when using it in the splitting integrators of the last section, we have reason to believe that it is inferior to the explicit Φ_{Kep} in speed and accuracy. In order to check this, we consider a two-body problem

in center-of-mass coordinates with $\mu = 3/16$ and initial conditions

$$x = 50, \tag{4.119}$$

$$p_y = 0.027475637, \tag{4.120}$$

$$y = z = p_x = p_z = 0. \tag{4.121}$$

For different step-sizes h , we integrate this system until $t_{\text{end}} = 10^7$, once with the numerical flow $\Phi_{\text{Kep},h}$ and once with the analytic flow $\varphi_{\text{N},h}$ which is qualitatively described by the following lines of pseudo-code:

```

1      function analytical_solution_step( $h, x_n, y_n, p_{x,n}, p_{y,n}$ )
2          calculate  $\phi_n(x_n, y_n)$ ;
3          calculate  $L_z(x_n, y_n, p_{x,n}, p_{y,n})$ ;
4          calculate  $e(H, L_z, \mu)$ ;
5          calculate  $\text{eccentric\_anomaly } E_n$ ;
6          calculate  $\text{mean\_anomaly } M_n = E_n - e \sin E_n$ ;
7          calculate  $\text{major\_semi-axis } a$ ;
8           $M_{n+1} = M_n + \sqrt{\frac{1+\mu}{a^3}} h$ ;
9          iteratively_solve_for  $E_{n+1}$  in  $M_{n+1} = E_{n+1} - e \sin E_{n+1}$ ;
10         calculate  $x = a[\cos(E_{n+1}) - e]$ ;
11         calculate  $y = a\sqrt{1 - e^2} \sin(E_{n+1})$ ;
12         calculate  $\rho_{n+1} = \sqrt{x_{n+1}^2 + y_{n+1}^2}$ ;
13         calculate  $\dot{\phi}_{n+1} = L_z / \mu \rho_{n+1}^2$ ;
14         calculate  $\dot{\rho}_{n+1} = \sqrt{1/\mu [2(H + \mu/\rho_{n+1}) - L_z^2/\mu \rho_{n+1}^2]}$ ;
15         calculate  $p_{x,n+1}(\dot{\phi}_{n+1}, \dot{\rho}_{n+1}, \rho_{n+1})$ ;
16         calculate  $p_{y,n+1}(\dot{\phi}_{n+1}, \dot{\rho}_{n+1}, \rho_{n+1})$ ;
17     end

```

We list the calculation times in table 4.1 and plot the relative error in the Hamiltonian

$$\Delta H(t) = \left| \frac{H(\mathbf{y}(t)) - H_0}{H_0} \right| \tag{4.122}$$

in Fig. 4.1. Obviously, $\Phi_{\text{Kep},h}$ is much faster than $\varphi_{\text{N},h}$. Furthermore, for not too large step

h	$\varphi_{\text{N},h}$	$\Phi_{\text{Kep},h}$
1	94 s	12 s
5	18 s	2 s
20	4 s	0.4 s
40	2 s	$\ll 1$ s

Table 4.1: Comparison of the calculation times for the integrators $\varphi_{\text{N},h}$ and $\Phi_{\text{Kep},h}$ applied with different step sizes h to the Kepler problem in the time interval $t \in [0, 10^7]$.

sizes, the numerical solution is more accurate than the ‘exact’ one. We can see very well how the round-off errors of the iteration sum up over time for the ‘exact’ solution. Therefore, we recommend to replace the ‘exact’ solution $\varphi_{\text{N},h}$ with the composition of Störmer-Verlet methods (4.118) when implementing the integrators of section 4.6.

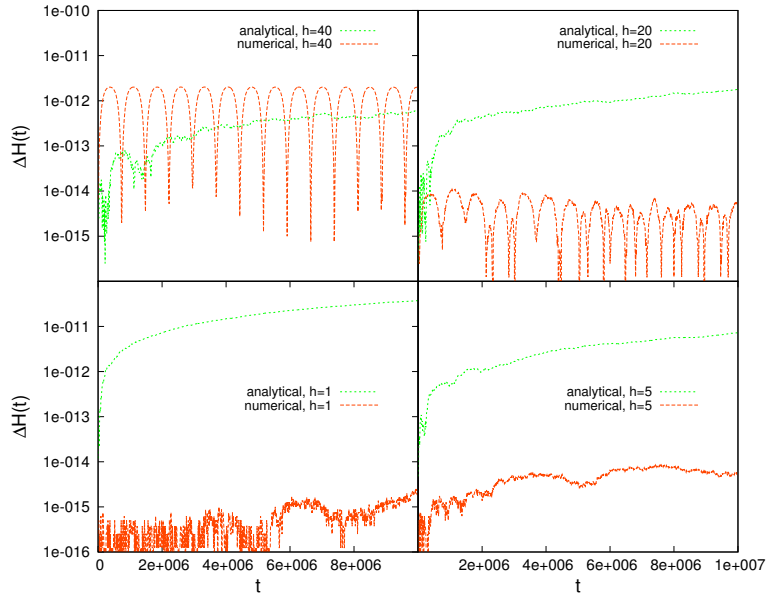


Figure 4.1: The energy error ΔH as a function of time t for the integrators $\varphi_{N,h}$ ('analytical') and $\Phi_{\text{Kep},h}$ ('numerical') in the time interval $t \in [0, 10^7]$ for various step sizes h .

4.8. Numerical experiments

In this section, we want, among others, to compare the accuracy of different schemes. Therefore, we will employ measures in line with section 3.10, namely the relative error in the Hamiltonian

$$\Delta H = \left| \frac{H(\mathbf{y}_n) - H(\mathbf{y}_0)}{H(\mathbf{y}_0)} \right|, \quad (4.123)$$

and the relative error along the trajectory

$$err = \sqrt{\sum_{i=1}^N \left(\frac{y_{\text{num}}^i - y_{\text{ex}}^i}{y_{\text{ex}}^i} \right)^2}. \quad (4.124)$$

Unless stated otherwise, the 'exact' solution $\mathbf{y}_{\text{ex}}(t)$ will be given by an $s = 6$ -stage Gauss-Runge-Kutta scheme with a step size $h = 0.1$ which we apply to the system in canonical coordinates.

The simulations are aborted due to poor accuracy as soon as the error in the energy exceeds the tolerance

$$\Delta H > 10^{-6}. \quad (4.125)$$

We will show below that setting a tolerance for the error in the energy is necessary in the long-time analysis of a binary's behaviour, as for such systems, integrators with bad energy conservation lead to false chaos indicators. This is the same effect as the one observed for the classical Hénon-Heiles problem in section 2.

As standard explicit competitors for the structure preserving integrators, we choose the classical RK4 method (2.13) and the CK5 scheme (3.151).

Let us now present the test cases with the help of which we compare the individual methods.

4.8.1. The test cases

We model three different kinds of motion, each of which is often encountered in binary simulations. We always fix the total mass as $m = 1$. Consequently, the important parameter concerning the two compact object's masses is the mass ratio $\sigma = m_1/m_2$. The individual masses and the reduced mass are thus given as

$$m_1 = \frac{\sigma}{1 + \sigma}, \quad (4.126)$$

$$m_2 = \frac{1}{1 + \sigma}, \quad (4.127)$$

$$\mu = \frac{\sigma}{(1 + \sigma)^2}. \quad (4.128)$$

The other relevant parameter is the factor χ_a , already introduced in section 4.5, that links masses with spins via

$$\|\mathbf{S}_a\| = \chi_a m_a^2. \quad (4.129)$$

Hence, the nature of a binary's orbit depends on the parameters σ, χ_1, χ_2 and the initial values

$$\mathbf{y}(0) = (p_x(0), p_y(0), p_z(0), \xi_1(0), \xi_2(0), x(0), y(0), z(0), \phi_1(0), \phi_2(0))^T. \quad (4.130)$$

This said, the three kinds of motion are represented by the following respective examples:

- With the set of initial data

$$\begin{aligned} \mathbf{y}(0) &= \left(0, \frac{3}{80}, 0, 0, 0, 35, 0, 0, 0, 0\right)^T, \\ \sigma &= \frac{1}{3}, \\ \chi_1 &= \chi_2 = 0, \end{aligned} \quad (4.131)$$

we model a system without spin effects. The spin contributions being switched off, the post-Newtonian system is integrable, e.g., (Zhong *et al.*, 2010), and the motion is restricted to the initial plane due to the conservation of the angular momentum. We present the orbit and the Poincaré sections for $t \in [0, 10^7]$ as obtained via ‘exact’ integration in Fig. 4.2. The orbit is apparently quasiperiodic.

- As a second test case, we choose the data set

$$\begin{aligned} \mathbf{y}(0) &= \left(0, \frac{3}{80}, 0, 0.25, -0.025, 35, 0, 0, \frac{\pi}{4}, \frac{\pi}{4}\right)^T, \\ \sigma &= \frac{1}{3}, \\ \chi_1 &= \chi_2 = \frac{3}{4}. \end{aligned} \quad (4.132)$$

In Fig. 4.3, we plot a part of the orbital trajectory for $t \in [0, 10^7]$. Alongside this, we plot the frequency spectrum of the x component for $I_1 = [0, 10^6]$ and $I_2 = [10^7 - 10^6, 10^7]$. We see that although the spin contributions have been switched on, the motion is still regular.

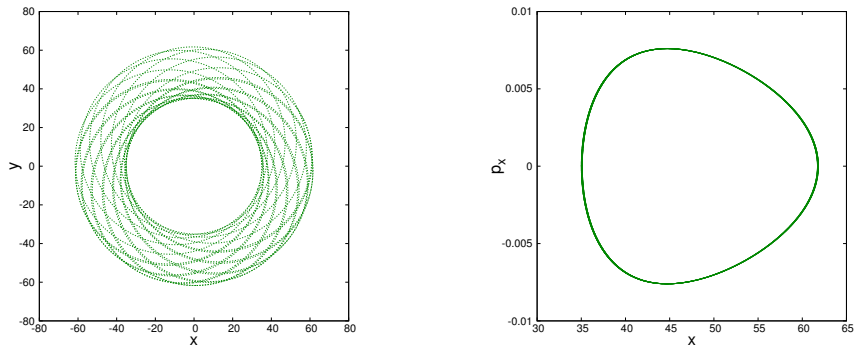


Figure 4.2: For the test case without spin contributions and $t \in [0, 10^7]$, the left panel shows an extract of the trajectory. The Poincaré sections for $y = 0$ and $p_y > 0$ are given in the right panel.

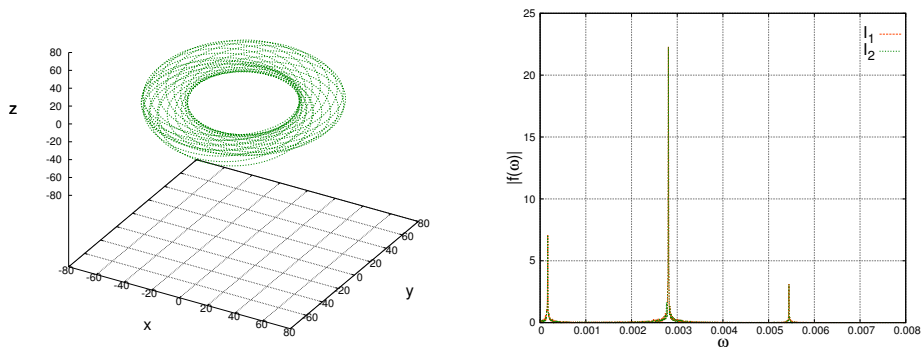


Figure 4.3: For the test case (4.132), the left panels shows the trajectory for $t \in [0, 50000]$. The frequency spectra $|f^x(\omega)|$ for the time intervals $I_1 = [0, 10^6]$ and $I_2 = [10^7 - 10^6, 10^7]$ are depicted in the right panel.

- We also consider a chaotic orbit. More precisely, we set

$$\begin{aligned} \mathbf{y}(0) &= \left(1, 0, \frac{3}{40}, 0, 0.25, -0.025, 6, 0, 0, \frac{\pi}{4}, \frac{\pi}{4} \right)^T, \\ \sigma &= 1, \\ \chi_1 &= \chi_2 = 1. \end{aligned} \tag{4.133}$$

We illustrate the chaotic behaviour by showing a part of the orbital trajectory and the FLI in Fig. 4.4.

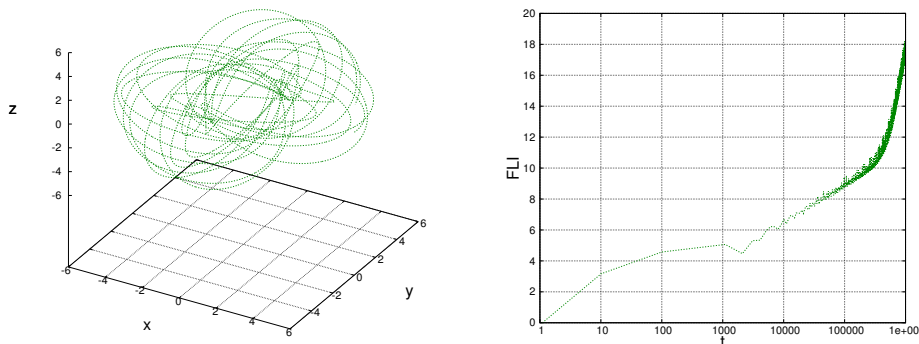


Figure 4.4: For the chaotic test case, the left panel shows the trajectory for $t \in [0, 25000]$. The linearly growing FLI is depicted in the right panel in semi-logarithmic scale.

Having thus established the test cases, we are able to start with our experiments.

4.8.2. Comparing splitting methods I

In section 4.6 we discussed different ways to split operators with regard to the special structure of the Hamiltonian (4.57). We now want to find out which possibility yields the better performance. More precisely, we want to compare the splitting methods (4.96) and (4.102). Therefore, we apply the integrators SympI, SympII, PoissonI, and PoissonII to the two regular test cases using various step sizes. We plot the relative error in the Hamiltonian (4.123) in Figs. 4.5, 4.6 and tabulate the corresponding calculation times T_{calc} in tables 4.2 and 4.3. During all simulations, the integration time was $t \in [0, 10^7]$.

The plots show quite clearly that splitting technique (4.96) leads to an energy error roughly half an order of magnitude smaller than the one of method (4.102). But not only is this splitting method more accurate but also does it result in less computational costs, cf. table 4.3. Apparently, having to calculate the implicit schemes less often and being able to apply mergers of the sort (4.109) is more of an advantage than the smaller step size for the implicit scheme. This circumstance is more pronounced for the Symp-algorithms, as for them, the implicit equations also include the spins and are thus of higher dimension. Therefore, we strongly recommend alternative (4.96) for the construction of splitting schemes.

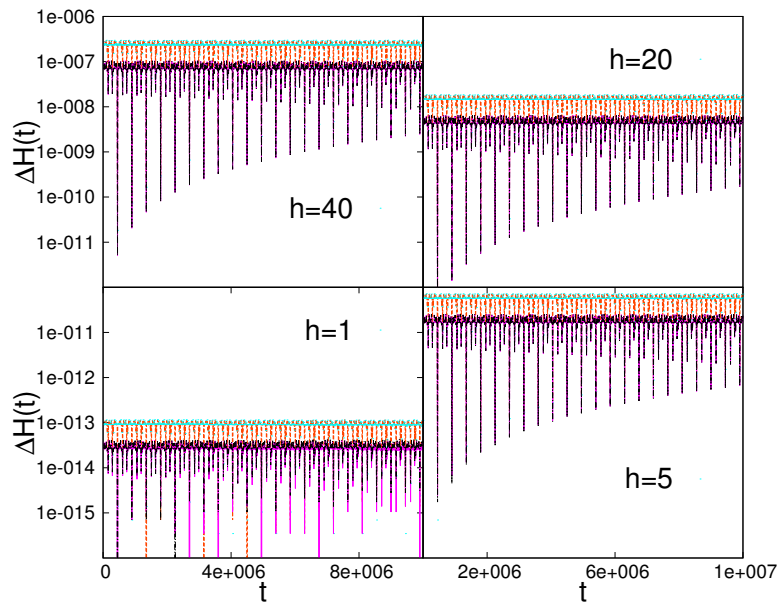


Figure 4.5: For initial data (4.131), $t \in [0, 10^7]$ and different step sizes h , the relative error in the Hamiltonian ΔH is plotted against time t for the splitting integrators of section 4.6, PoissonII (orange), SympII (light blue), PoissonI (magenta), and SympI (black).

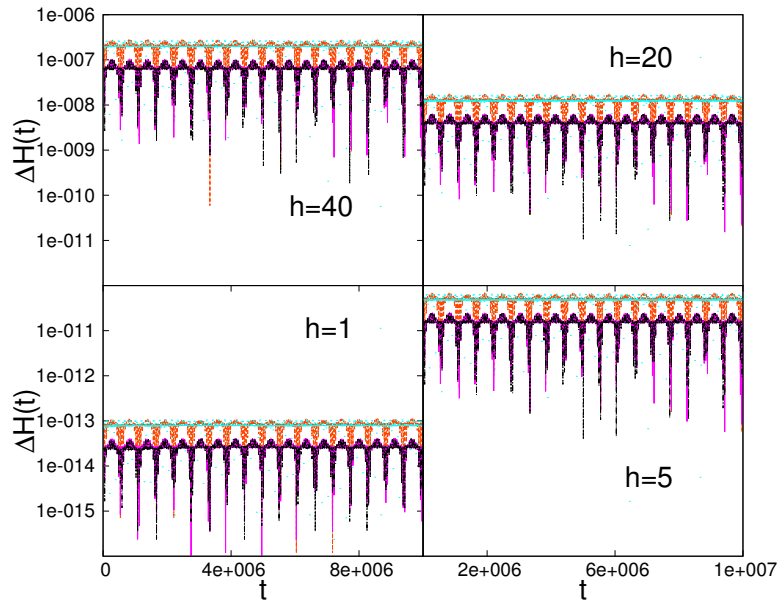


Figure 4.6: For initial data (4.132), $t \in [0, 10^7]$ and different step sizes h , the relative error in the Hamiltonian ΔH is plotted against time t for the splitting integrators of section 4.6, PoissonII (orange), SympII (light blue), PoissonI (magenta), and SympI (black).

Integrator	$h = 40$	$h = 20$	$h = 5$	$h = 1$
PoissonI	4.36	8.35	30.95	142.86
SympI	4.36	8.35	30.95	142.86
SympII	6.11	11.56	41.91	191.55
PoissonII	6.11	11.56	41.91	191.55

Table 4.2: The CPU calculation times in [s] for the splitting integrators of section 4.6 applied to the regular test case (4.131) with different step sizes h . The integration interval was $t \in [0, 10^7]$ in all simulations. N.b.: As the spin contributions are turned off, methods I and II are the same in this case.

Integrator	$h = 40$	$h = 20$	$h = 5$	$h = 1$
SympI	9.90	18.72	67.75	304.95
PoissonI	17.37	34.23	133.34	655.11
SympII	15.41	29.36	104.03	463.43
PoissonII	19.15	37.48	144.65	705.18

Table 4.3: The CPU calculation times in [s] for the splitting integrators of section 4.6 applied to the regular, spinning test case (4.132) with different step sizes h . The integration interval was $t \in [0, 10^7]$ in all simulations.

4.8.3. Comparing splitting methods II

We now want to compare the two underlying ideas for our splitting integrators, namely the Poisson integrator introduced in section 4.4 and the transformation to canonical form as illustrated in section 4.5. For the purely orbital motion, both ideas result in the same integration scheme wherefore we consider the test cases with spin.

By analysing Fig. 4.6, we observe that there is no difference in the accuracy for the regular motion. However, with regard to the computation times in table 4.3, the Poisson scheme turns out to be much more expensive. Taking into account table 4.2, we notice that the exact calculation of all terms for the spin-orbit, spin-spin part (4.78) increases the computational effort drastically. For SympI and SympII the additional costs are lower. One can see further that the difference between the Poisson... and Symp... schemes is much larger than the difference due to the splitting techniques (4.96) and (4.102).

This said, we focus on the chaotic test orbit (4.133) and analyse the error in the energy ΔH . As, for these initial values, the system has an unfavourable behaviour, we use smaller step sizes than before. The results for SympI are shown in Fig. 4.7, the corresponding CPU times are listed in table 4.4. Although for $h = 5$ the simulation falls victim to criterion (4.125), SympI can cope with the chaotic orbit for smaller step sizes. Not so PoissonI. When applying this scheme to the chaotic orbit, simulations are soon aborted even for very small step sizes. As an illustration, we plot the energy error for the small step size $h = 0.1$ in Fig. 4.8. We observe perturbations at some times which successively take the numerical solution away from the exact one until, at one point, the system is exploding altogether. Numerical tests reveal that reducing the step size to $h = 0.01$ does not alleviate the problem.

Thus, integration schemes based on the transformation to symplectic form are faster and more reliable for chaotic systems than Poisson integrators such as PoissonI. But how do splitting schemes fare in comparison to other methods?

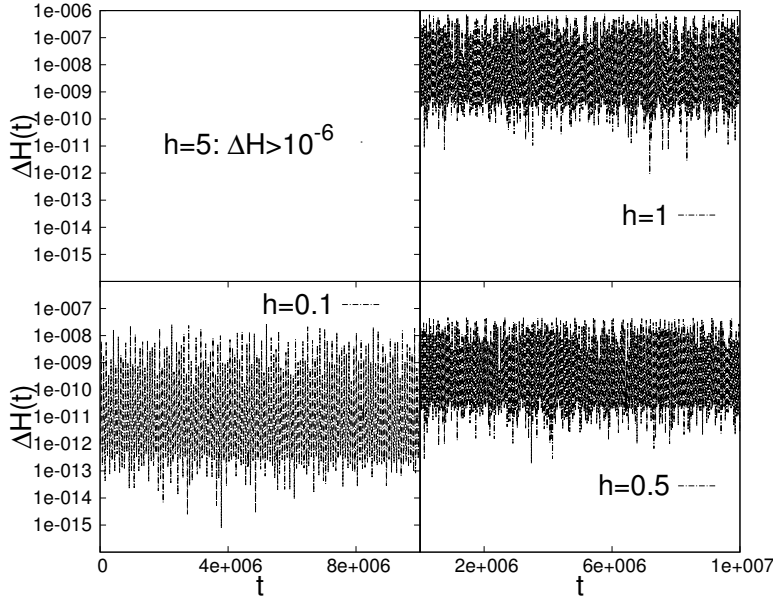


Figure 4.7: For initial data (4.133), $t \in [0, 10^7]$ and different step sizes h , the relative error in the Hamiltonian ΔH during simulations with SympI is plotted against time t .

Integrator	$h = 5$	$h = 1$	$h = 0.5$	$h = 0.1$
SympI	a	463.78	833.85	3445.49

Table 4.4: The CPU calculation times in [s] for the splitting integrator SympI applied to the chaotic test case (4.133) with different step sizes h . The integration interval was $t \in [0, 10^7]$ in all simulations. ‘a’ signifies ‘aborted due to condition (4.125)’.

4.8.4. Comparing various integration methods

As was already mentioned in section 4.6, the binary system in canonical form can be solved with Gauss collocation schemes instead of splitting methods. Of course, one can also try standard explicit schemes. Therefore, we apply Gauss2, Gauss3, Gauss4, RK4, and CK5 to our three orbits (4.131)-(4.133). As for the Gauss collocation schemes, we use the same step sizes as for the splitting integrators. For the explicit schemes, the step size is reduced because we expect these to have worse accuracy. The simulation times for the three test cases are shown in tables 4.5-4.7. It is obvious that all five Runge-Kutta schemes are much faster than the splitting schemes, cf. tables 4.2-4.4. Looking more closely, one can observe that the implicit, structure preserving Gauss collocation methods are not significantly slower than the explicit schemes when using the same step size. Above all for small step sizes, the additional cost is minimal. This is thanks to the starting approximations, introduced in section 3.8, resulting in

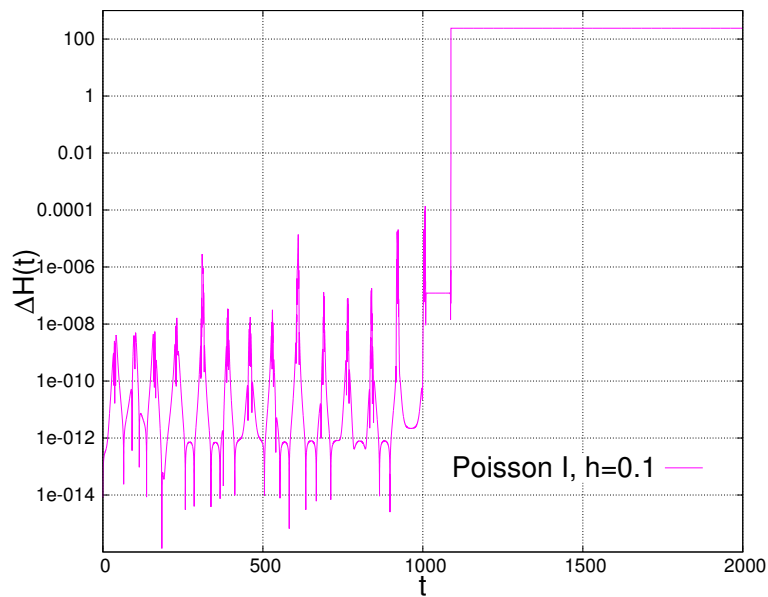


Figure 4.8: For initial data (4.133) and a step size $h = 0.1$, the relative error in the Hamiltonian ΔH is plotted against time t for the PoissonI scheme.

small numbers of iterations per step. We illustrate this by listing the iterations per step for Gauss 4 in table 4.8. Tables 4.2-4.4 show further that the Gauss Runge-Kutta schemes allow for the use of larger step sizes without violating condition (4.125).

Integrator	$h = 40$	$h = 20$	$h = 5$	$h = 1$	$h = 0.5$	$h = 0.1$
RK4	a	a	a	13.80	27.58	137.91
CK5	a	a	4.70	23.01	46.07	230.01
Gauss2	a	3.89	11.44	43.81	81.73	344.41
Gauss3	3.27	5.32	15.44	58.48	105.73	422.69
Gauss4	3.96	6.47	18.74	67.26	120.59	443.49

Table 4.5: The CPU calculation times in [s] for explicit and implicit Runge-Kutta schemes applied to the orbital test case (4.132) with different step sizes h . The integration interval was $t \in [0, 10^7]$ in all simulations. ‘a’ signifies ‘aborted due to condition (4.125)’.

In order to investigate the accuracy in detail, we consider the cases with spin and compare the relative error along the trajectory (4.124) in Figs. 4.9, 4.11, as well as the error in the energy (4.123) in Figs. 4.10, 4.12. The explicit schemes show pronounced drifts in the energy and the relative error. SympI has good conservation properties but the Gauss collocation schemes offer by far the best accuracy for small computational cost.

Having found the fastest and most accurate way to integrate post-Newtonian equations of motion – a transformation to symplectic form followed by the application of a Gauss collocation method – we now turn our attention towards the indicators of chaos. We start with the Poincaré sections.

Integrator	$h = 40$	$h = 20$	$h = 5$	$h = 1$	$h = 0.5$	$h = 0.1$
RK4	a	a	a	43.99	87.93	439.44
CK5	a	a	14.31	71.56	143.02	716.16
Gauss2	a	10.03	29.37	111.23	205.68	852.88
Gauss3	8.10	13.19	38.09	141.19	255.60	997.65
Gauss4	10.00	16.44	46.63	160.95	283.26	1068.56

Table 4.6: The CPU calculation times in [s] for explicit and implicit Runge-Kutta schemes applied to the regular, spinning test case (4.132) with different step sizes h . The integration interval was $t \in [0, 10^7]$ in all simulations. ‘a’ signifies ‘aborted due to condition (4.125)’.

Integrator	$h = 5$	$h = 1$	$h = 0.5$	$h = 0.1$	$h = 0.05$	$h = 0.01$
RK4	a	a	a	a	a	2997.76
CK5	a	a	a	a	a	4840.96
Gauss2	a	a	a	1190.14	–	–
Gauss3	a	a	449.47	1548.56	–	–
Gauss4	a	347.22	566.67	1893.45	–	–

Table 4.7: The CPU calculation times in [s] for explicit and implicit Runge-Kutta schemes applied to the chaotic test case (4.132) with different step sizes h . The integration interval was $t \in [0, 10^7]$ in all simulations. ‘a’ signifies ‘aborted due to condition (4.125)’, ‘-’ means that no simulation has been run for the corresponding step size.

test case	$h = 40$	$h = 20$	$h = 5$	$h = 1$	$h = 0.5$	$h = 0.1$
initial values (4.131)	9.19	7.44	5.16	3.46	2.99	2.13
initial values (4.132)	9.31	7.59	5.30	3.54	3.07	2.24
initial values (4.133)	–	–	a	9.21	7.44	4.85

Table 4.8: Number of iterations per step for Gauss4, applied with different step sizes to the three test cases. ‘a’ signifies ‘aborted due to condition (4.125)’, ‘-’ means that no simulation has been run for the corresponding step size.

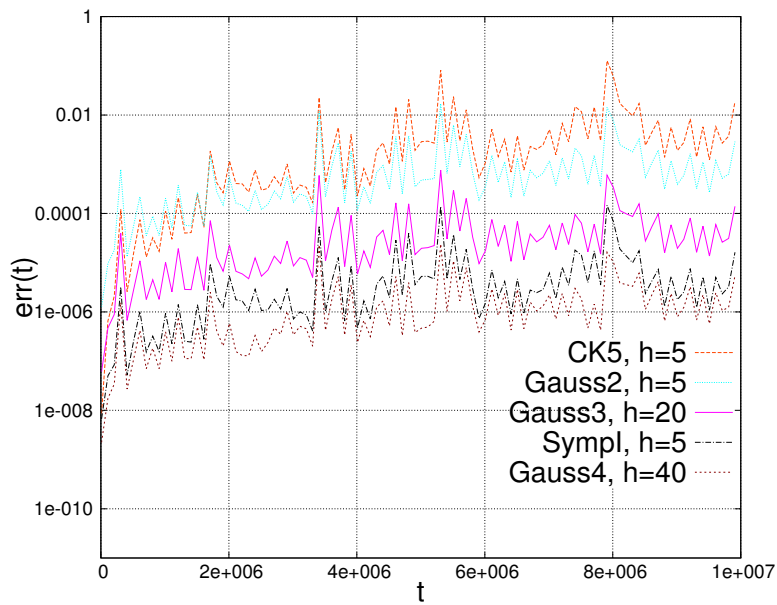


Figure 4.9: For initial data (4.132) and $t \in [0, 10^7]$, the relative error along the trajectory err is plotted against time t for various integration schemes.

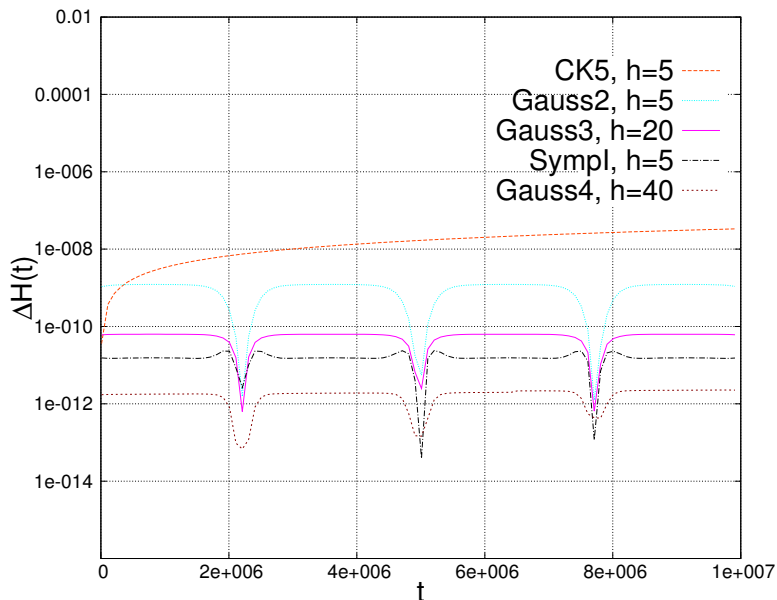


Figure 4.10: For initial data (4.132) and $t \in [0, 10^7]$, the relative error in the Hamiltonian ΔH is plotted against time t for various integration schemes.

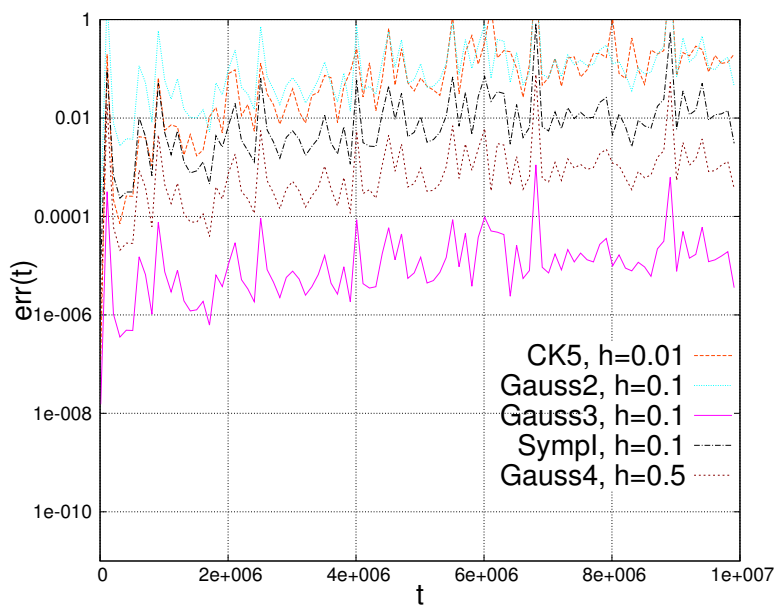


Figure 4.11: For initial data (4.133), the relative error along the trajectory err is plotted against time t for various integration schemes.

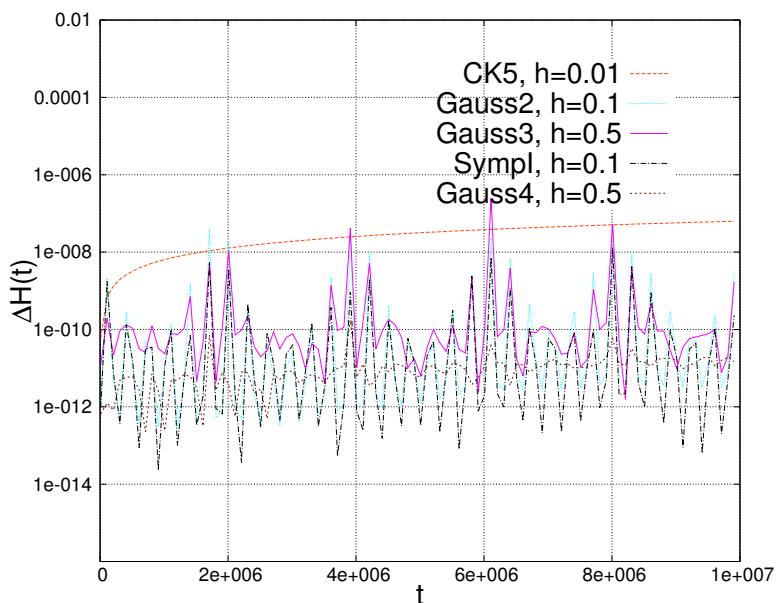


Figure 4.12: For initial data (4.133) and $t \in [0, 10^7]$, the relative error in the Hamiltonian ΔH is plotted against time t for various integration schemes.

4.8.5. Comparing methods to calculate Poincaré sections

In subsection 2.2.1, three distinct methods for the calculation of Poincaré sections were presented. We now test which of these is best suited for applications in the realm of post-Newtonian equations. Therefore, we calculate sections in all three ways once for the purely orbital motion and once for the chaotic test case. We choose Gauss3 as the underlying integrator as this scheme has proven to be a trustworthy tool in the last subsection. The step size in the purely orbital case is $h = 20$; for the chaotic orbit it is set to be $h = 0.1$. For the first algorithm, the successive reduction of the step size, we reduce the time steps until they reach a value of $h_{\text{step}} = \text{eps}$, where $\text{eps} \approx 10^{-16}$ is the double precision. For the interpolation algorithm, we choose a polynomial of order $\tilde{p} = 6$ as this equals the order of a Gauss scheme with $s = 3$ stages. The respective calculation times are listed in table 4.9. Obviously, the reduction of the step size results in much more computational cost. In order to

algorithm	purely orbital motion	chaotic motion
reducing the step size	7.23	1650.96
interpolation	5.34	1557.86
collocation	5.33	1555.72

Table 4.9: The CPU calculation times in [s] for the calculation of all Poincaré sections of the $y = 0$ -plane for $t \in [0, 10^7]$ with Gauss3 and the three algorithms of subsection 2.2.1.

examine whether this additional effort is rewarded by higher accuracy, we plot the error in the energy for points of the section,

$$\Delta H_{\text{sect}} = \left| \frac{H(\mathbf{y}_{\text{sect}}) - H(\mathbf{y}_0)}{H(\mathbf{y}_0)} \right|, \quad (4.134)$$

in Fig. 4.13. We observe that although the reduction of the step size yields a smaller error in the energy, the other algorithms show good results as well. The difference between the interpolation method and the collocation is not very large. For small step sizes, as in the test for the chaotic orbit, the difference between both algorithms vanishes completely. On the whole, if a reliable scheme is used for integrating the equations of motion, the collocation polynomial will yield satisfactory results in the most convenient way. Thus, we were right to recommend its use in subsection 2.2.1 above.

In chapter 2 integration schemes with bad energy conservation were found to be misleading concerning the chaoticity of a classical system. We thus ask ourselves what happens with the Poincaré section of our relativistic system in such a case. In order to answer this question, we apply the RK4 scheme with step sizes $h = 1, 5, 20, 40$ to our purely orbital motion which is in fact four-dimensional and therefore well represented by a two-dimensional section. The respective results are depicted in Fig. 4.14. We see that the larger the step size, the more the sections deviate from the exact form. For $h = 40$, the sections look rather chaotic. Analysing the error in the energy ΔH , shown in Fig. 4.15, we see that the aberration in the sections goes hand in hand with a deteriorating energy conservation. Contrarily, for Gauss3 with $h = 40$ the energy is conserved. This yields the correct Poincaré sections of the quasiperiodic motion, as can be deduced from Fig. 4.16.

We now proceed with the next indicator of chaos.

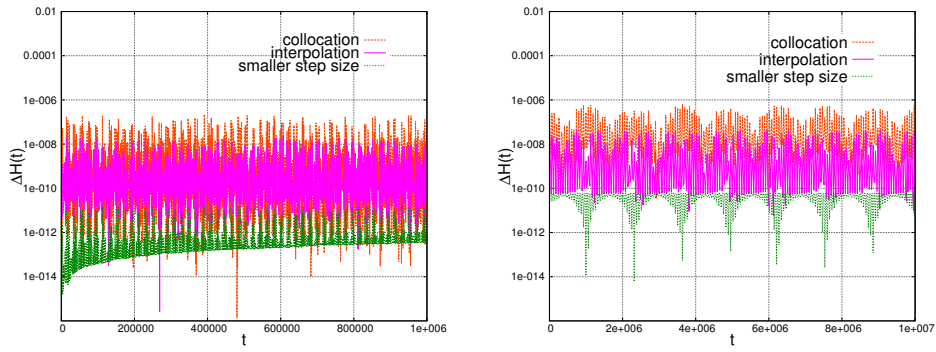


Figure 4.13: For the three methods to calculate Poincaré sections, initial data (4.133), and $t \in [0, 10^7]$, the relative error in the Hamiltonian on the section ΔH_{sect} is plotted against time t in the left panel. The right panel shows the same for initial values (4.131).

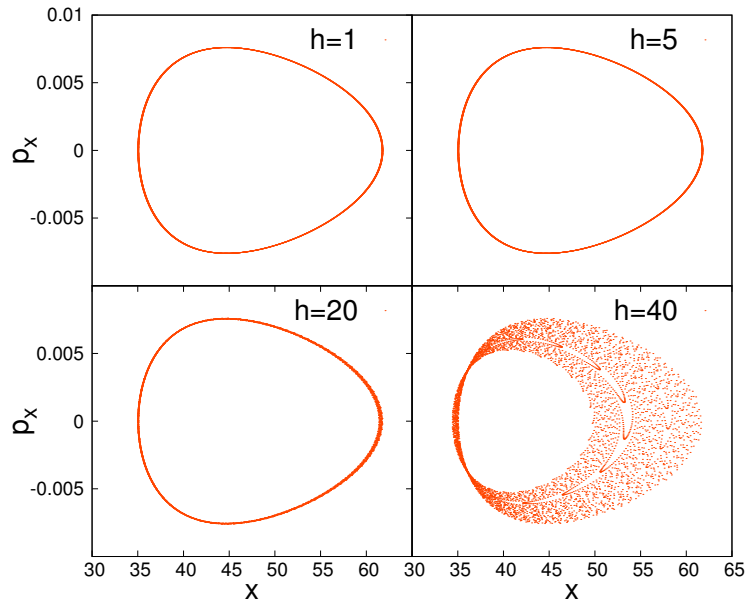


Figure 4.14: Poincaré sections at $y = 0$, $p_y > 0$ for the purely orbital test case obtained with RK4 and four different step sizes h .

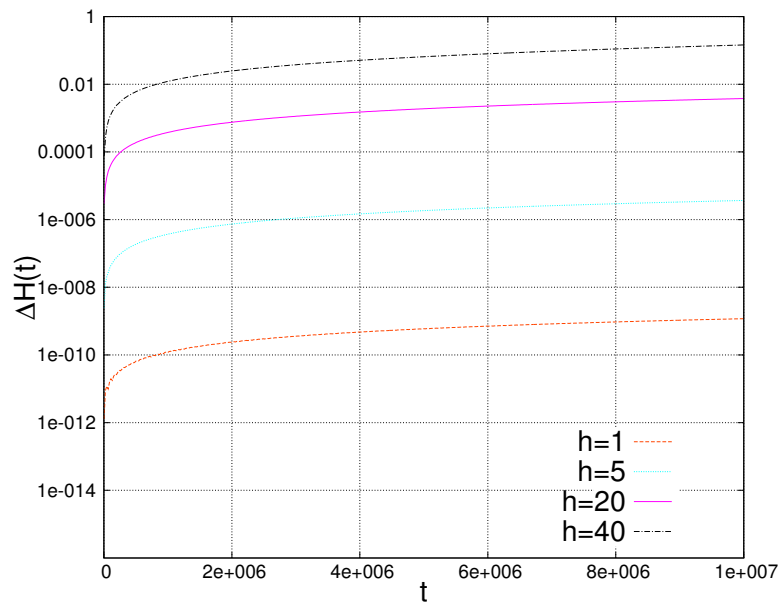


Figure 4.15: For the classical RK4 scheme applied with different step sizes h to the purely orbital test case, the error in the energy ΔH is plotted against integration time t .

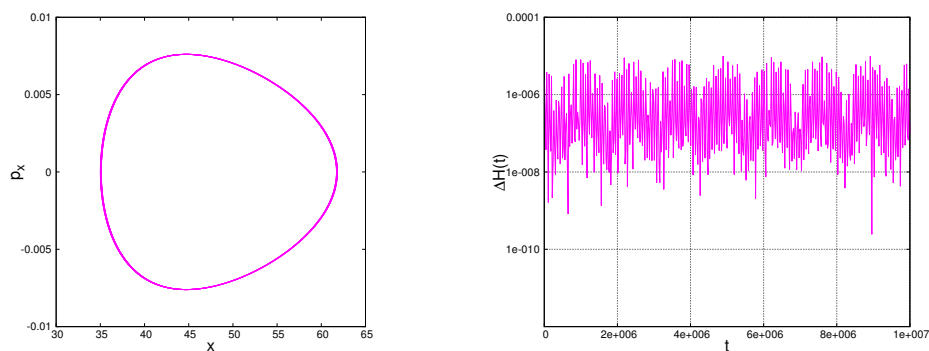


Figure 4.16: The left panel shows Poincaré sections at $y = 0$, $p_y > 0$ for the purely orbital test case obtained with Gauss3 and $h = 40$. In the right panel, the corresponding error in the energy ΔH is plotted against integration time t .

4.8.6. The two-particle method applied to the binary system

In chapter 2 the maximum Lyapunov exponent was introduced as a reliable tool to indicate chaos for systems with more than two degrees of freedom. Furthermore, the two-particle method was shown to be more comfortable than the variational approach. We now examine its results when applied to the post-Newtonian equations of motions in combination with different integration schemes. First we use Gauss3 with the very large step size $h = 40$ to propagate the purely orbital test case along with its shadow trajectory. We also apply Gauss3 with $h = 0.5$ to the chaotic orbit (4.133). The resulting LEs are shown in Fig. 4.17 along with the exact solutions. We delightedly see a striking similarity between numerical and exact solution. Whereas for the quasiperiodic motion the LEs are steadily decreasing, they tend to a small but still positive value in the chaotic case. As in the last subsection, we now employ the classical

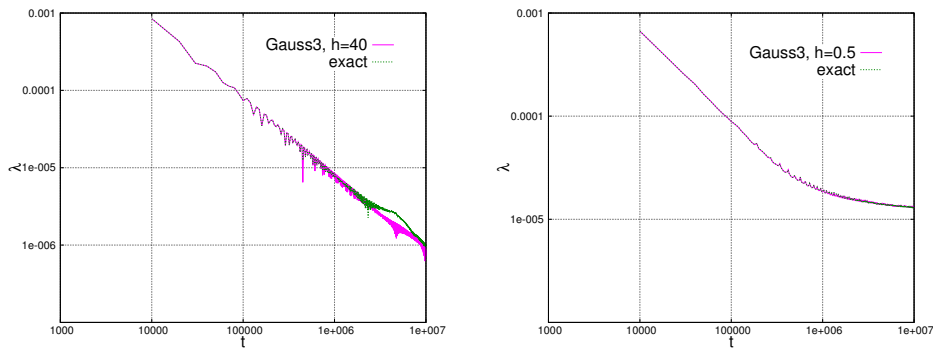


Figure 4.17: The left panel shows the exact solution and the result obtained via Gauss3 and $h = 40$ of the maximum Lyapunov exponent λ for the purely orbital test case. In the right panel, the same results, with $h = 0.5$ instead of $h = 40$ for Gauss3, are plotted for the chaotic test case.

RK4 method. When applying this scheme with $h = 0.5$ to the chaotic test case, simulations were soon aborted because the renormalization interval was too large. This caused an overflow in LE's value. The result for RK4 with $h = 40$ applied to the purely orbital motion is shown in Fig. 4.18. One observes a bent at around $t = 8 \cdot 10^6$, which lets the LE converge towards a finite value. This is in accordance with our results of the previous subsection.

We now focus on a different aspect concerning the two-particle method: [Tancredi et al. \(2001\)](#) found out that for some classical examples, the approximation of the variational method by a finite distance between two trajectories can inflict errors which sum up over the length of the integration, in particular so when small step sizes are used. To examine this phenomenon in our relativistic application, we calculate the orbital motion's LE with explicit and Gauss collocation schemes, choosing for each a step size of $h = 1$. With this step size, even RK4 yielded the correct Poincaré section above. As for the corresponding maximum Lyapunov exponents, however, for large t , the explicit solutions deviate from the exact ones and converge towards a constant positive value, see Fig. 4.19. Hence, for binaries, too, round-off errors can accumulate during the integration if too small a step size is used. For Gauss3, a small drift is observed which for Gauss4, $h = 1$ vanishes altogether. Therefore, we have demonstrated another advantage of the structure preserving schemes: Even if they lead to a small aberration due to round-off errors for small step sizes, they can be applied with large time steps, thus

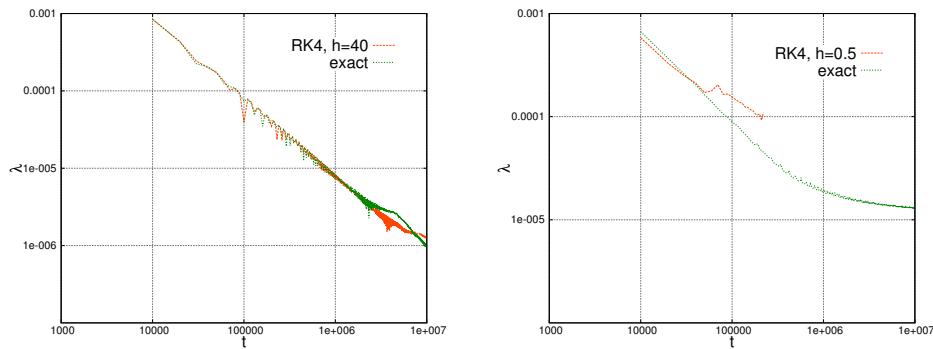


Figure 4.18: The left panel shows the exact solution and the result obtained via RK4 and $h = 40$ for the maximum Lyapunov exponent λ for the purely orbital test case. In the right panel, the same results, with $h = 0.5$ instead of $h = 40$ for RK4, are plotted for the chaotic test case.

avoiding the occurrence of such awkward effects. This said, we go on to another indicator.

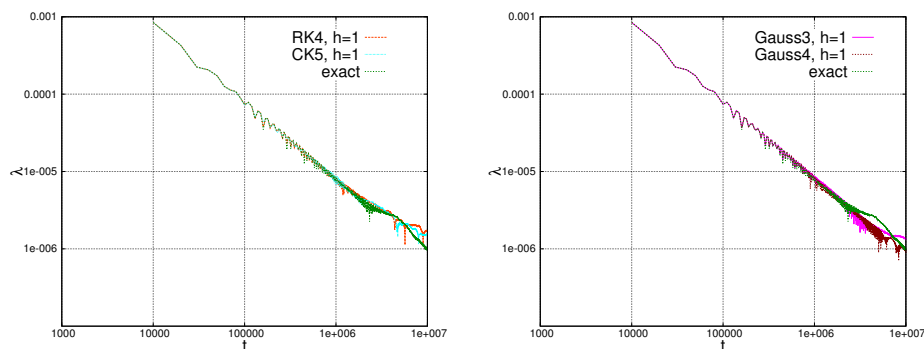


Figure 4.19: The maximum Lyapunov exponent λ obtained via integrations with small step sizes compared with the exact solution. The left panel shows the result for explicit schemes, the right panel is the same for Gauss collocation methods.

4.8.7. The frequency spectra

When calculating frequency spectra for the post-Newtonian equations, we expect the same phenomena as the ones encountered in the last two subsections. To verify this, we again consider RK4 with $h = 1, 5, 20, 40$, and calculate the x -component's frequency spectra in the intervals $t \in [0, 10^6]$ and $t \in [0, 10^7 - 10^6]$ for the regular spinning motion corresponding to the initial values (4.132). Looking at the results in Fig. 4.20, we see that for $h = 20$ there is a shift in the frequencies. For $h = 40$, there is not only a shift but the spectra already resemble a noisy frequency distribution common for chaotic orbits. This fits well to the respective Poincaré sections, cf. Fig. 4.14 above. In contrast, the Gauss collocation schemes show outstanding results even for large step sizes. To illustrate this, we calculate the spectra with Gauss3 and $h = 40$ and plot the results in Fig. 4.21 along with the exact solution. No difference between

the structure preserving algorithm and the exact solution can be observed. Thus, for all three main indicators of chaos, Gauss collocation schemes give the correct predictions with regard to chaoticity. If energy is not conserved, however, the indicators can lead to false conclusions.

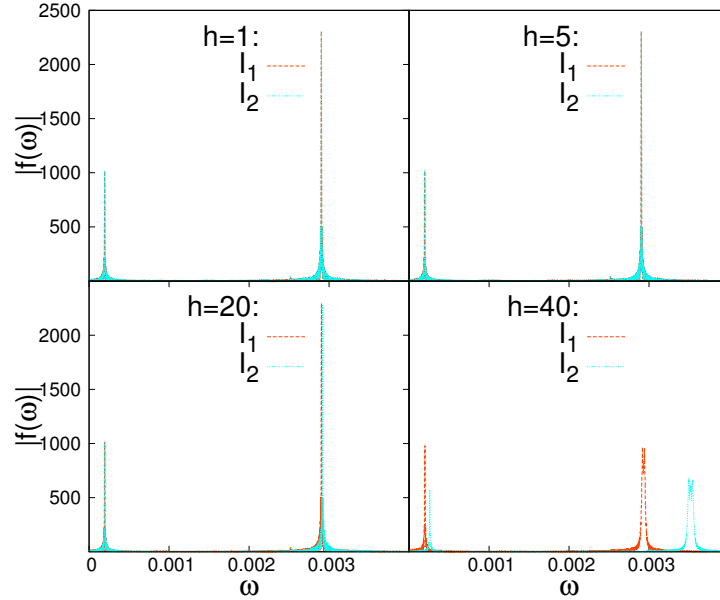


Figure 4.20: The frequency spectra of the x-component, $|f^x(\omega)|$, with arbitrary normalization in the intervals $I_1 = [0, 10^6]$ and $I_2 = [10^7 - 10^6, 10^7]$ as obtained by the RK4 method with different step sizes.

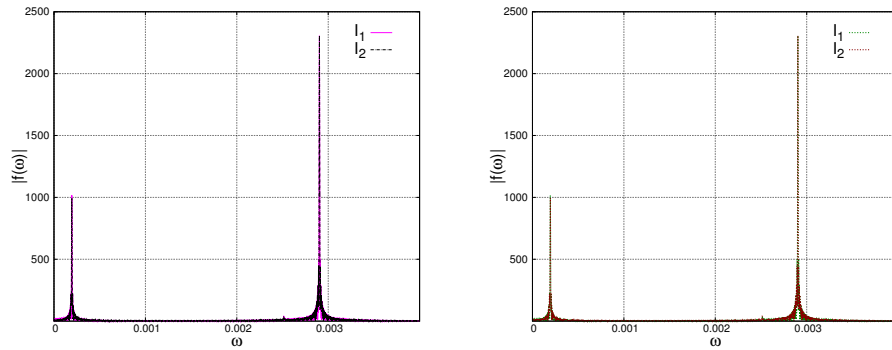


Figure 4.21: The left panel shows the frequency spectra of the x-component, $|f^x(\omega)|$, with arbitrary normalization in the intervals $I_1 = [0, 10^6]$ and $I_2 = [10^7 - 10^6, 10^7]$ as obtained by Gauss3 with $h = 40$. The right panel depicts the corresponding exact solution.

4.8.8. Systems with radiation

We have seen that the structure preserving algorithms have excellent conservation properties when applied to symplectic systems. What will happen if we add a radiation term to the binary

system? On the one hand, the system loses the structure which gave rise to the advantageous integrators in the first place. On the other hand, it is known from classical mechanics that, at least in this field, structure preserving algorithms outperform explicit schemes also when a non-conservative term is added to the Hamiltonian. In order to examine the corresponding behaviour for relativistic binaries, we modify the equation of motion of the momenta (4.41) to account for radiation. We choose a model derived by Buonanno *et al.* (2006) which is commonly used in general relativity and set

$$\frac{d\mathbf{p}}{dt} = -\nabla_{\mathbf{x}}H + \mathbf{F}_{\text{rad}}. \quad (4.135)$$

The exact form of the radiation term \mathbf{F}_{rad} is given in appendix E below. To illustrate its effects on the trajectory, we plot the evolution of the radial distance q for our regular, spinning test case (4.132) as given by the exact solution in Fig. 4.22. Here, we calculate the ‘exact’ solution with CK5 and the very small step size $h = 0.01$. As time increases, the distance between the two particles is decreasing faster and faster. For $t > 500\,000$, the binary will soon collapse. Thus, we restrict our simulations to an interval $t \in [0, 500\,000]$.

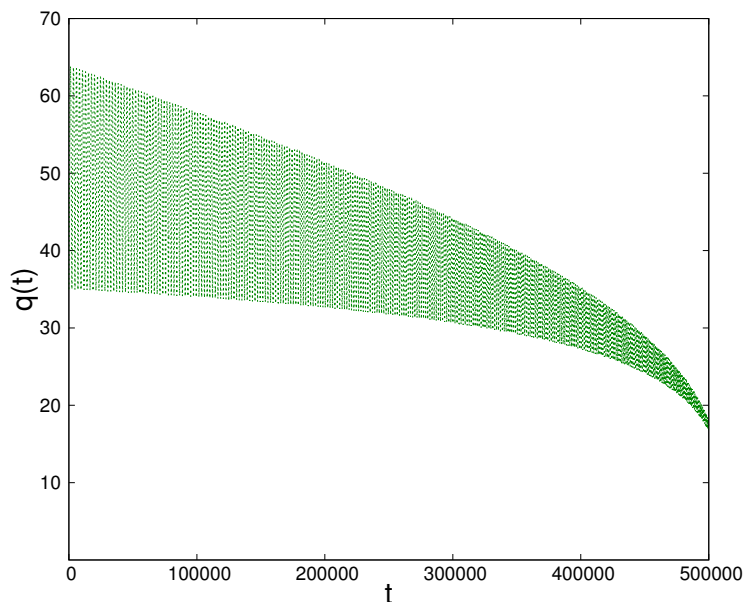


Figure 4.22: The radial distance q as function of integration time t for the regular spinning orbit with radiation effects included.

In the subsections above, CK5 and Gauss3/Gauss4 showed the best results for explicit and structure preserving schemes, respectively. We thus focus on these integrators and compare their performance with the radiation turned on. We first list the calculation times for the three schemes applied with different step sizes each, cf. table 4.10. With increasing time steps, the difference in CPU time becomes ever smaller as the collocation methods’ average number of iterations per step decreases analogously to the conservative case.

As a measure for the accuracy we plot the relative error along the trajectory (4.124) in Fig. 4.23. Taking into account the calculation times, the collocation methods yield the better results for less computational costs – just as in the conservative case.

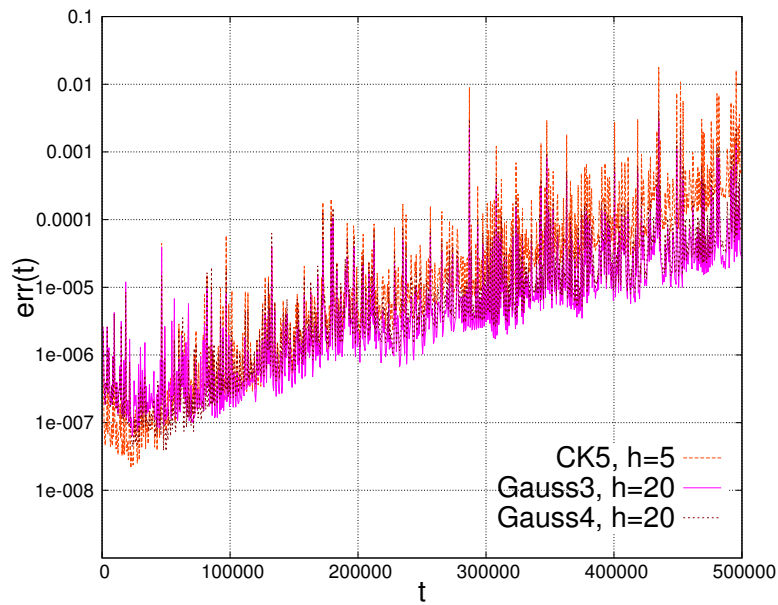


Figure 4.23: The relative error along the trajectory, err against integration time t for explicit and collocation schemes.

Integrator	$h = 40$	$h = 20$	$h = 5$	$h = 1$	$h = 0.5$	$h = 0.1$
CK5	0.14	0.28	1.21	5.75	11.50	57.51
Gauss3	0.92	1.47	4.04	16.45	25.69	99.77
Gauss4	1.08	1.72	4.72	17.28	32.00	133.36

Table 4.10: The CPU calculation times in [s] for explicit and implicit Runge-Kutta schemes applied with different step sizes h to the test case (4.132) with radiation effects included. The integration interval was $t \in [0, 500\,000]$ for all simulations.

Long story short, Gauss-Runge-Kutta schemes turn out to be magnificent tools for the post-Newtonian equations – with or without non-conservative radiation terms. Let us now, finally, summarize our results in the next chapter.

5. Summary

In this work, we first introduced the most important indicators to analyse the chaoticity of a dynamical system, namely Poincaré sections, frequency spectra, maximum Lyapunov exponents, as well as the fast Lyapunov indicator, and discussed how they can be implemented in an efficient way. When applying these indicators to a simple classical system, the Hénon-Heiles problem, we could see that their behaviour is influenced by the numerical integration scheme with which the system is propagated in time. In particular, the use of integrators with a shift in the energy could make regular motion look like chaotic orbits. But by placing appropriate demands on the accuracy of the scheme, the indicators show the right behaviour independent of the integration scheme. Furthermore, we discussed algorithms to calculate all Lyapunov exponents of a system. Unfortunately, these algorithms proved very expensive when testing them for the Hénon-Heiles case. Therefore, we recommended to only calculate the maximum exponent when investigating a system for chaotic behaviour. Having demonstrated that a correct prediction with regard to chaoticity requires accurate schemes and long time intervals, we turned our attention towards relativistic compact binary systems.

First, we considered Extreme Mass Ratio Inspirals. We explained that the resulting equations of motion can show properties which demand for very sophisticated numerical solution techniques. Above all, structure preserving step size algorithms are indispensable in such cases. However, the hitherto available step size controllers failed to deliver satisfactory results. Thus, we proposed a new efficient structure preserving algorithm well-suited for applications in geodesic equations of motion. Due to the non-separability of the geodesic equations of motion, our new algorithm is based on Gauss collocation methods. Therefore, we discussed their properties and then described in detail how to implement these implicit schemes. After proving our integrator's structure-preserving properties, we demonstrated the new algorithm's superior performance in numerical experiments.

Hereafter, we focused on binaries with rather equal masses. We exposed that these systems can be approximated by the post-Newtonian formalism. This approach leads to a Hamiltonian with spins, which from a numerical analysis point of view is equivalent to a Poisson system. We described two different possibilities for the structure preserving integration of these systems. One yields a Poisson integration which splits the Hamiltonian in many parts, almost each of which can be solved analytically. The second method is based on a coordinate transformation. We proved that the system in the new coordinates has a canonical structure. Therefore, symplectic integration schemes can be applied. As the post-Newtonian equations resemble a perturbed Kepler problem, we analysed splitting techniques adapted to the Hamiltonian's perturbative form. We tested splitting methods for both the Poisson integration and the coordinate transformation ansatz. Besides these, Gauss collocation methods were applied to the transformed system. Numerical experiments showed that the splitting methods are much more expensive than the Gauss collocation schemes. Thus, a transformation to canonical form combined with a Gauss-Runge-Kutta scheme was shown to be the best approach.

Afterwards, chaos indicators were tested for the post-Newtonian equations. We saw that here, too, bad energy conservation properties can lead to false estimates with regard to chaoticity. Thus, numerical simulations have to be aborted as soon as the error in the energy becomes too large.

As a last point, we showed that Gauss collocation methods are the best choice even when

radiation effects are taken into account although, then, the system's structure is destroyed by the additional terms.

In short, despite its age, Gauss collocation seems to be the state-of-the-art integration technique when considering relativistic binary systems. Energy conservation is very important to ensure reliable forecasts of a system's behaviour. This said, advantageous integration methods for both common formalisms of relativistic binary systems have been singled out and efficient implementations of the most important chaos indicators have been proposed. We hope that all this will be of great use in simulations by the gravitational wave astronomy.

Acknowledgments

During the whole of this work, I was splendidly supervised by Prof. Dr. Ch. Lubich whom I am grateful for fruitful discussions. I also want to thank Prof. Dr. W. Kley who thankfully volunteered as supervisor for the physics department. I further want to honor all the members of Prof. Lubich's team. Not least the interesting discussions with my colleagues make me proud of being part of the numerical analysis group. I also would like to mention Dhia Mansour and Peter Vastag. I really enjoyed the interesting meetings we had.

Special thanks go to my collaborator Georgios Lukes-Gerakopoulos from the Friedrich-Schiller university in Jena whom it always was and always will be a pleasure to work with. The whole work concerning the geodesic approximation results from our cooperation in this field. But also beyond the geodesic approach, I've got a lot of insight into general relativity and chaoticity thanks to him.

I would not be the one I am, were it not for my parents Dieter and Regine. My parents who would have done anything for their children. Desperate not to have a better way to say 'thank you', I dedicate this work to them. Last but not least, I want to thank my girlfriend Elena who welcomed me at home without any grumbling even after way too many way too long hours in the office.

This work has partly been supported by the DFG grant SFB/Transregio 7.

A.

Using the auxiliary functions of section 3.9, we list here the equations of motion for the MSM spacetime in the form they have been implemented in:

$$\begin{aligned}
\dot{p}_u = & \frac{1}{2g_{uu}} \left\{ -\frac{1}{D} \left(\frac{\partial E}{\partial u} - \frac{E}{D} \frac{\partial D}{\partial u} \right) \frac{(g_{t\phi}L_z + g_{\phi\phi}m_0\mathcal{E})^2}{(\kappa^2(u^2 - 1)(1 - v^2))^2} - 2\frac{1 - v^2}{D} \left(\frac{\partial F}{\partial u} - \frac{F}{D} \frac{\partial D}{\partial u} \right) \times \dots \right. \\
& \times \frac{(g_{t\phi}L_z + g_{\phi\phi}m_0\mathcal{E})(g_{tt}L_z + g_{t\phi}m_0\mathcal{E})}{(\kappa^2(u^2 - 1)(1 - v^2))^2} - \frac{(g_{tt}L_z + g_{t\phi}m_0\mathcal{E})^2}{(\kappa^2(u^2 - 1)(1 - v^2))^2} \times \dots \\
& \times \left[2\lambda_2 \frac{\partial \lambda_1}{\partial u} - \frac{\lambda_2}{D^2} \frac{\partial D}{\partial u} [\lambda_1(P^2 - E) + \lambda_2 T^2] \right. \\
& \quad \left. + \frac{\lambda_2}{D} \left(\frac{\partial \lambda_1}{\partial u} (P^2 - E) + \lambda_1 \left(2P \frac{\partial D}{\partial u} - \frac{\partial E}{\partial u} \right) + 2\lambda_2 T \frac{\partial T}{\partial u} \right) \right] - \dots \\
& - \frac{1}{8\kappa^6(u^2 - 1)(u^2 - v^2)^4} \left(\frac{u^2 - v^2}{2} \left(\frac{\partial D}{\partial u} - \frac{8uD}{u^2 - v^2} \right) - uD \frac{1 - v^2}{u^2 - 1} \right) p_u^2 + \dots \\
& + \frac{1}{16\kappa^6(1 - v^2)(u^2 - v^2)^4} \left((u^2 - v^2) \left(\frac{\partial D}{\partial u} - \frac{8uD}{u^2 - v^2} \right) + 2uD \right) p_v^2 - \dots \\
& \left. - \frac{2}{16\kappa^6(u^2 - 1)(u^2 - v^2)^4} \left((u^2 - v^2) \left(\frac{\partial D}{\partial v} + \frac{8vD}{u^2 - v^2} \right) - 2vD \right) p_u p_v \right\} \\
\dot{p}_v = & \frac{1}{2g_{vv}} \left\{ -\frac{1}{D} \left(\frac{\partial E}{\partial v} - \frac{E}{D} \frac{\partial D}{\partial v} \right) \frac{(g_{t\phi}L_z + g_{\phi\phi}m_0\mathcal{E})^2}{(\kappa^2(u^2 - 1)(1 - v^2))^2} - \dots \right. \\
& - 2 \left(2u \frac{F}{D} - \frac{1 - v^2}{D} \left(\frac{\partial F}{\partial v} - \frac{F}{D} \frac{\partial D}{\partial v} \right) \right) \times \dots \\
& \times \frac{(g_{t\phi}L_z + g_{\phi\phi}m_0\mathcal{E})(g_{tt}L_z + g_{t\phi}m_0\mathcal{E})}{(\kappa^2(u^2 - 1)(1 - v^2))^2} - \frac{(g_{tt}L_z + g_{t\phi}m_0\mathcal{E})^2}{(\kappa^2(u^2 - 1)(1 - v^2))^2} \times \dots \\
& \times \left[2\lambda_1 \frac{\partial \lambda_2}{\partial v} + \frac{1}{D} \left(\frac{\partial \lambda_2}{\partial v} - \frac{\lambda_2}{D} \frac{\partial D}{\partial v} \right) (\lambda_1(P^2 - E) + \lambda_2 T^2) \right. \\
& \quad \left. + \frac{\lambda_2}{D} \left(\lambda_1 \left(2P \frac{\partial P}{\partial v} - \frac{\partial E}{\partial v} \right) + \frac{\partial \lambda_2}{\partial v} T^2 + 2\lambda_2 T \frac{\partial T}{\partial v} \right) \right] + \dots \\
& + \frac{1}{8\kappa^6(u^2 - 1)(u^2 - v^2)^4} \left((u^2 - v^2) \left(\frac{\partial D}{\partial v} + \frac{8vD}{u^2 - v^2} \right) - 2vD \right) p_u^2 - \dots \\
& - \frac{1}{16\kappa^6(1 - v^2)(u^2 - v^2)^4} \left((u^2 - v^2) \left(\frac{\partial D}{\partial v} + \frac{8vD}{u^2 - v^2} \right) + 2vD \frac{u^2 - 1}{1 - v^2} \right) p_v^2 - \dots \\
& \left. - \frac{2}{16\kappa^6(1 - v^2)(u^2 - v^2)^4} \left((u^2 - v^2) \left(\frac{\partial D}{\partial u} - \frac{8uD}{u^2 - v^2} \right) + 2uD \right) p_u p_v \right\}
\end{aligned}$$

$$\dot{u} = p_u$$

$$\dot{v} = p_v,$$

The ‘tmp-variables’ are:

$$\frac{\partial E}{\partial u} = 2R \frac{\partial R}{\partial u} + \lambda_2 S \left(s \frac{\partial \lambda_1}{\partial u} + 2\lambda_1 \frac{\partial S}{\partial u} \right)$$

$$\frac{\partial E}{\partial v} = 2R \frac{\partial R}{\partial v} + \lambda_1 S \left(s \frac{\partial \lambda_2}{\partial v} + 2\lambda_2 \frac{\partial S}{\partial v} \right)$$

$$\frac{\partial D}{\partial u} = \frac{\partial E}{\partial u} + P \frac{\partial R}{\partial u} + R \frac{\partial P}{\partial u} + \lambda_2 \left(T \frac{\partial S}{\partial u} + S \frac{\partial T}{\partial u} \right)$$

$$\frac{\partial D}{\partial v} = \frac{\partial E}{\partial v} + P \frac{\partial R}{\partial v} + R \frac{\partial P}{\partial v} + \lambda_2 \left(T \frac{\partial S}{\partial v} + S \frac{\partial T}{\partial v} \right) + TS \frac{\partial \lambda_2}{\partial v}$$

$$\frac{\partial F}{\partial u} = T \frac{\partial R}{\partial u} + R \frac{\partial T}{\partial u} - \left(SP \frac{\partial \lambda_1}{\partial u} + \lambda_1 S \frac{\partial P}{\partial u} + \lambda_1 P \frac{\partial S}{\partial u} \right)$$

$$\frac{\partial F}{\partial v} = T \frac{\partial R}{\partial v} + R \frac{\partial T}{\partial v} - \lambda_1 \left(S \frac{\partial P}{\partial v} + P \frac{\partial S}{\partial v} \right)$$

$$\frac{\partial \lambda_2}{\partial u} = 2\kappa^2 x$$

$$\frac{\partial \lambda_2}{\partial v} = 2v$$

$$\begin{aligned} \frac{\partial P}{\partial u} = & 2 \{ \kappa m [(2\kappa u + m)^2 - 2v^2(2\delta + ab - b^2) - a^2 + b^2 - q^2] + \dots \\ & + 4\kappa^2 m u (2\kappa u + m) - 4\kappa^2 q^2 u \} \end{aligned}$$

$$\frac{\partial P}{\partial v} = -8[\kappa m u v (2\delta + ab - b^2) + v(4\delta d - m^2 b^2)]$$

$$\frac{\partial R}{\partial u} = 16\kappa u [\kappa^2 (u^2 - 1) + \delta(1 - v^2)]$$

$$\begin{aligned} \frac{\partial R}{\partial v} = & -16\delta v [\kappa^2 (u^2 - 1) + \delta(1 - v^2)] - \dots \\ & - 4v(1 - v^2)(a - b)[(a - b)(d - \delta) - m^2 b + q\mu] \end{aligned}$$

$$\frac{\partial S}{\partial u} = -8(a - b)\kappa^2 u$$

$$\frac{\partial S}{\partial v} = -8v[(a - b)(2\delta - \kappa^2) + (m^2 b - q\mu)]$$

$$\begin{aligned} \frac{\partial T}{\partial u} = & 4\{2\kappa m b [\kappa^2 (u^2 - 1) + \delta(1 - v^2)] + 2\kappa^2 u (2\kappa m b u + 2m^2 b - q\mu)\} - \dots \\ & - k\kappa m (1 - v^2)[(a - b)(d - \delta) - m^2 b + q\mu] \end{aligned}$$

$$\begin{aligned} \frac{\partial T}{\partial v} = & -2v\{(a - b)(m^2 b^2 - 4\delta d) - \dots \\ & - (4\kappa m u + 2m^2 - q^2)[(a - b)(d - \delta) - m^2 b + q\mu]\} - \dots \\ & - 8\delta v (2\kappa m b u + 2m^2 b - q\mu) \end{aligned}$$

B.

The equations of motion of the post-Newtonian formalism with 3PN orbital and leading spin-orbit and spin-spin contribution are given here. They read

$$\begin{aligned}\frac{d\mathbf{p}}{dt} &= -\nabla_{\mathbf{x}}H_N - \nabla_{\mathbf{x}}H_{\text{PN}} - \nabla_{\mathbf{x}}H_{\text{SO,SS}} \\ \frac{d\mathbf{x}}{dt} &= \nabla_{\mathbf{p}}H_N + \nabla_{\mathbf{p}}H_{\text{PN}} + \nabla_{\mathbf{p}}H_{\text{SO,SS}}, \\ \frac{d\mathbf{S}_1}{dt} &= \left[2 \left(1 + \frac{3m_2}{4m_1} \right) \mathbf{L} - \mathbf{S}_2 + 3 \left(\mathbf{nS}_2 + \frac{m_2}{m_1} \mathbf{nS}_1 \right) \mathbf{n} \right] \times \mathbf{S}_1, \\ \frac{d\mathbf{S}_2}{dt} &= \left[2 \left(1 + \frac{3m_1}{4m_2} \right) \mathbf{L} - \mathbf{S}_1 + 3 \left(\mathbf{nS}_1 + \frac{m_1}{m_2} \mathbf{nS}_2 \right) \mathbf{n} \right] \times \mathbf{S}_2.\end{aligned}$$

As they are referred to in the text above, we give the individual terms in (B) and (B) in detail. The Newtonian terms are simply

$$\nabla_{\mathbf{x}}H_N = \frac{\mu}{q^3} \mathbf{x},$$

and

$$\nabla_{\mathbf{p}}H_N = \frac{1}{\mu} \mathbf{p}.$$

The terms due to the spin-orbit and spin-spin Hamiltonian read

$$\begin{aligned}\nabla_{\mathbf{x}}H_{\text{SO,SS}} &= \frac{2}{q^3} \mathbf{p} \times \mathbf{S}_{\text{eff}} + \left\{ \left[3 \left(\mathbf{S}_1 \mathbf{S}_2 + \frac{1}{2} \left(\frac{m_2}{m_1} \mathbf{S}_1 \mathbf{S}_1 + \frac{m_1}{m_2} \mathbf{S}_2 \mathbf{S}_2 \right) \right) - \dots \right. \right. \\ &\quad \left. \left. - 15 \left((\mathbf{nS}_2)(\mathbf{nS}_1) + \frac{1}{2} \left(\frac{m_1}{m_2} (\mathbf{nS}_1)^2 + \frac{m_2}{m_1} (\mathbf{nS}_2)^2 \right) \right) - 6 \mathbf{S}_{\text{eff}} \mathbf{L} \right] \mathbf{n} + \dots \right. \\ &\quad \left. + 3 \left[\left(\mathbf{nS}_2 + \frac{m_2}{m_1} \mathbf{nS}_1 \right) \mathbf{S}_1 + \left(\mathbf{nS}_1 + \frac{m_1}{m_2} \mathbf{nS}_2 \right) \mathbf{S}_2 \right] \right\} \frac{1}{q^4}, \\ \nabla_{\mathbf{p}}H_{\text{SO,SS}} &= \frac{2}{q^3} \mathbf{S}_{\text{eff}} \times \mathbf{x},\end{aligned}$$

where \mathbf{L} , \mathbf{S}_{eff} , and q are given in 4.2. In order to present the orbital post-Newtonian terms in the form in which they have been implemented, we first define the following ‘tmp-variables’:

$$\begin{aligned}P_{1,1} &:= \frac{3\nu - 1}{2}, \\ P_{1,2} &:= \frac{3 + \nu}{2}, \\ P_{1,3} &:= \frac{\nu}{2}, \\ P_{2,1} &:= \frac{6 - 30\nu(1 - \nu)}{16},\end{aligned}$$

$$\begin{aligned}
P_{2,2} &:= \frac{5 - \nu(20 + 3\nu)}{8}, \\
P_{2,3} &:= \frac{\nu^2}{2}, \\
P_{2,4} &:= \frac{3}{2}\nu^2, \\
P_{2,5} &:= 3\nu, \\
P_{2,6} &:= 5 + 8\nu, \\
P_{2,7} &:= \frac{3 + 9\nu}{4}, \\
P_{3,1} &:= \frac{280\nu[1 + \nu(\nu - 2)] - 40}{128}, \\
P_{3,2} &:= \frac{\nu[42 - \nu(53 + 5\nu)] - 7}{16}, \\
P_{3,3} &:= \frac{(2 - 3\nu)\nu^2}{16}, \\
P_{3,4} &:= \frac{3\nu^2(1 - \nu)}{16}, \\
P_{3,5} &:= \frac{\nu(136 + 109\nu) - 27}{16}, \\
P_{3,6} &:= \frac{(17 + 30\nu)\nu}{16}, \\
P_{3,7} &:= \frac{(5 + 43\nu)\nu}{12}, \\
P_{3,8} &:= \left(\nu \left(\frac{\pi^2}{64} - \frac{335}{48} - \frac{23}{8}\nu \right) - \frac{25}{8} \right), \\
P_{3,9} &:= \left(-\frac{85}{16} - \frac{3\pi^2}{64} - \frac{7\nu}{4} \right) \nu, \\
P_{3,10} &:= \left(\frac{1}{2} + \left(\frac{109}{3} - \frac{21\pi^2}{8} \right) \nu \right), \\
P_{3,11} &:= \frac{5}{16}\nu^3.
\end{aligned}$$

With these quantities and

$$\begin{aligned}
p_n &:= \frac{\mathbf{n} \cdot \mathbf{p}}{\mu^2}, \\
p_p &:= \frac{\mathbf{p} \cdot \mathbf{p}}{\mu^2},
\end{aligned}$$

we have

$$\nabla_{\mathbf{x}} H_{\text{PN}} = \left\{ \left[p_p [P_{1,2} - p_p (P_{2,2} + p_p P_{3,2})] + \dots \right. \right.$$

$$\begin{aligned}
& + p_n^2 \left(3P_{1,3} + p_p \left(\frac{3}{2}P_{2,3} - 3p_p P_{3,3} \right) + p_n^2 \left(\frac{5}{4}P_{2,4} + 7P_{3,11}p_n^2 - 5P_{3,4}p_p \right) \right) + \dots \\
& + \frac{1}{q} \left(\frac{1}{q} \left(P_{2,7} - 3p_p P_{3,8} - 5P_{3,9}p_n^2 - \frac{P_{3,10}}{q} \right) - p_p (P_{2,6} + 2P_{3,5}p_p) - \dots \right. \\
& \left. - p_n^2 (2P_{2,5} + 4P_{3,6}p_p + 6p_n^2 P_{3,7}) - 1 \right) \left. \right] \frac{\mu}{q} \mathbf{x} + \dots \\
& + \left[p_p (2P_{3,3}p_p - P_{2,3}) - 2P_{1,3} + p_n^2 (4P_{3,4} - P_{2,4} - 6P_{3,11}p_n^2) + \dots \right. \\
& \left. + \frac{1}{q} \left(P_{2,5} + 2P_{3,6}p_p + 4P_{3,7}p_n^2 + \frac{2P_{3,9}}{q} \right) \right] p_n \mathbf{p} \left. \right\} \frac{1}{q^2}, \\
\nabla_{\mathbf{p}} H_{\text{PN}} = & \left\{ p_p \left[P_{1,1} + \frac{4}{q} \left(P_{2,2} + P_{3,3}p_n^2 + \frac{P_{3,5}}{q} \right) + \dots \right. \right. \\
& + p_p \left(P_{2,1} + \frac{6P_{3,2}}{q} + P_{3,1}p_p \right) \left. \right] + \dots \\
& + \frac{1}{q} \left[-2P_{1,2} + \frac{1}{q} \left(P_{2,6} + \frac{2P_{3,8}}{q} \right) + \dots \right. \\
& \left. + p_n^2 \left(\frac{2P_{3,6}}{q} - P_{2,3} + 2P_{3,4}p_n^2 \right) \right] \left. \right\} \frac{1}{\mu} \mathbf{p} + \dots \\
& + \left[\frac{1}{q} \left(P_{2,5} + \frac{2P_{3,9}}{q} \right) - 2P_{1,3} + 2p_p \left(P_{3,3}p_p - \frac{P_{2,3}}{2} + \frac{P_{3,6}}{q} \right) + \dots \right. \\
& \left. + 4p_n^2 \left(P_{3,4}p_p - \frac{P_{2,4}}{4} - \frac{3P_{3,11}p_n^2}{2} + \frac{P_{3,7}}{q} \right) \right] \frac{p_n}{q^2} \mathbf{x}
\end{aligned}$$

C.

We give here the flows Φ_{SS}^i which are obtained after the splitting of the leading order post-Newtonian spin-spin Hamiltonian H_{SS} . In addition to the rotation operator $\text{rot}(\boldsymbol{\Omega}, t)$ introduced in section 4.4, we make use of the operator $\widetilde{\text{rot}}$ which is defined as

$$\begin{aligned}\widetilde{\text{rot}}(\boldsymbol{\Omega}, t)\mathbf{a}(0) &:= \int_0^t \text{rot}(\boldsymbol{\Omega}, s)\mathbf{a}(0)ds = \dots \\ &= t\mathbf{a}(0) + 2 \left(\frac{\sin(\frac{\|\boldsymbol{\Omega}\|t}{2})}{\|\boldsymbol{\Omega}\|} \right)^2 \boldsymbol{\Omega} \times \mathbf{a}(0) + \frac{\|\boldsymbol{\Omega}\|t - \sin(\|\boldsymbol{\Omega}\|t)}{\|\boldsymbol{\Omega}\|^3} \boldsymbol{\Omega} \times \boldsymbol{\Omega} \times \mathbf{a}(0).\end{aligned}$$

As the spin-spin Hamiltonian is independent of the momenta \mathbf{p} , the positions remain constant. For the Hamiltonian H_{SS}^1 , we have

$$\varphi_{\text{SS},t}^1(\mathbf{p}(0), \mathbf{x}(0), \mathbf{S}_1(0), \mathbf{S}_2(0)) = \begin{pmatrix} \mathbf{p}(t) \\ \mathbf{x}(t) \\ \mathbf{S}_1(t) \\ \mathbf{S}_2(t) \end{pmatrix} = \begin{pmatrix} \mathbf{p}(0) - \frac{3tH_{\text{SS}}^1}{q^2}\mathbf{x}(0) \\ \mathbf{x}(0) \\ \text{rot}\left(-\frac{1}{q^3}(\mathbf{S}_1(0) + \mathbf{S}_2(0)), t\right) \mathbf{S}_1(0) \\ \text{rot}\left(-\frac{1}{q^3}(\mathbf{S}_1(0) + \mathbf{S}_2(0)), t\right) \mathbf{S}_2(0) \end{pmatrix}.$$

The Hamiltonian H_{SS}^2 leads to a motion only in the momenta. Its flow is

$$\varphi_{\text{SS},t}^2(\mathbf{p}(0), \mathbf{x}(0), \mathbf{S}_1(0), \mathbf{S}_2(0)) = \begin{pmatrix} \mathbf{p}(t) \\ \mathbf{x}(t) \\ \mathbf{S}_1(t) \\ \mathbf{S}_2(t) \end{pmatrix} = \begin{pmatrix} \mathbf{p}(0) - \frac{3tH_{\text{SS}}^2}{q^2}\mathbf{x}(0) \\ \mathbf{x}(0) \\ \mathbf{S}_1(0) \\ \mathbf{S}_2(0) \end{pmatrix}.$$

The flow corresponding to H_{SS}^3 yields

$$\begin{aligned}\mathbf{p}(t) &= \mathbf{p}(0) + \frac{5tH_{\text{SS}}^3}{q^2}\mathbf{x}(0) - \frac{3\mathbf{n} \cdot \mathbf{S}_2(0)}{q^4} \widetilde{\text{rot}}\left(\frac{3\mathbf{n}\mathbf{S}_2(0)}{q^3}\mathbf{n}, t\right) \mathbf{S}_1(0) - \dots \\ &\quad - \frac{3\mathbf{n} \cdot \mathbf{S}_1(0)}{q^4} \widetilde{\text{rot}}\left(\frac{3\mathbf{n}\mathbf{S}_1(0)}{q^3}\mathbf{n}, t\right) \mathbf{S}_2(0), \\ \mathbf{x}(t) &= \mathbf{x}(0), \\ \mathbf{S}_1(t) &= \text{rot}\left(\frac{3\mathbf{n}\mathbf{S}_2(0)}{q^3}\mathbf{n}, t\right) \mathbf{S}_1(0), \\ \mathbf{S}_2(t) &= \text{rot}\left(\frac{3\mathbf{n}\mathbf{S}_1(0)}{q^3}\mathbf{n}, t\right) \mathbf{S}_2(0),\end{aligned}$$

whereas φ_{SS}^4 results in

$$\begin{aligned} \mathbf{p}(t) &= \mathbf{p}(0) + \frac{5tH_{\text{SS}}^3}{q^2}\mathbf{x}(0) - \frac{3\mathbf{n} \cdot \mathbf{S}_1(0)}{2q^4} \widetilde{\text{rot}} \left(\frac{3\mathbf{n}\mathbf{S}_1(0)}{2q^3} \mathbf{n}, t \right) \mathbf{S}_1(0) - \dots \\ &\quad - \frac{3\mathbf{n} \cdot \mathbf{S}_2(0)}{2q^4} \widetilde{\text{rot}} \left(\frac{3\mathbf{n}\mathbf{S}_2(0)}{2q^3} \mathbf{n}, t \right) \mathbf{S}_2(0), \\ \mathbf{x}(t) &= \mathbf{x}(0), \\ \mathbf{S}_1(t) &= \text{rot} \left(\frac{3\mathbf{n}\mathbf{S}_1(0)}{2q^3} \mathbf{n}, t \right) \mathbf{S}_1(0), \\ \mathbf{S}_2(t) &= \text{rot} \left(\frac{3\mathbf{n}\mathbf{S}_2(0)}{2q^3} \mathbf{n}, t \right) \mathbf{S}_2(0). \end{aligned}$$

D.

We give here the post-Newtonian equations of motion for the system given in terms of the 10 canonical variables $(\mathbf{p}, \mathbf{x}, \phi_1, \xi_1, \phi_2, \xi_2)$. In this case, the equations of motion for the positions and momenta are the same as in the original coordinates. One only has to re-express \mathbf{S}_1 and \mathbf{S}_2 in (B) and (B) by means of the canonical variables $(\phi_1, \xi_1, \phi_2, \xi_2)$. The equations for the canonical angles are

$$\begin{aligned}
\frac{d\phi_1}{dt} &= \frac{2}{q^3} \left[\left(1 + \frac{3m_2}{4m_1} \right) \left(m_1^2 \chi_1 L_z - \frac{\xi_1}{\rho_1} m_1^2 \chi_1 [\cos(\phi_1) L_x + \sin(\phi_1) L_y] \right) + \dots \right. \\
&\quad + \frac{1}{2q^2} \left(\frac{m_2}{m_1} \mathbf{xS}_1 + \mathbf{xS}_2 \right) \left(z m_1^2 \chi_1 - m_1^2 \chi_1 [\cos(\phi_1) x + \sin(\phi_1) y] \frac{\xi_1}{\rho_1} \right) + \dots \\
&\quad \left. + \frac{1}{2} \frac{\rho_2}{\rho_1} \xi_1 m_1^2 m_2^2 \chi_1 \chi_2 [\cos(\phi_1) \cos(\phi_2) + \sin(\phi_1) \sin(\phi_2) - \xi_2] \right], \\
\frac{d\phi_2}{dt} &= \frac{2}{q^3} \left[\left(1 + \frac{3m_1}{4m_2} \right) \left(m_2^2 \chi_2 L_z - \frac{\xi_2}{\rho_2} m_2^2 \chi_2 [\cos(\phi_2) L_x + \sin(\phi_2) L_y] \right) + \dots \right. \\
&\quad + \frac{1}{2q^2} \left(\frac{m_1}{m_2} \mathbf{xS}_2 + \mathbf{xS}_1 \right) \left(z m_2^2 \chi_2 - m_2^2 \chi_2 [\cos(\phi_2) x + \sin(\phi_2) y] \frac{\xi_2}{\rho_2} \right) + \dots \\
&\quad \left. + \frac{1}{2} \frac{\rho_1}{\rho_2} \xi_2 m_2^2 m_1^2 \chi_2 \chi_1 [\cos(\phi_2) \cos(\phi_1) + \sin(\phi_2) \sin(\phi_1) - \xi_1] \right], \\
\frac{d\xi_1}{dt} &= \frac{2}{q^3} \left[\left(1 + \frac{3m_2}{4m_1} \right) m_1^2 \chi_1 \rho_1 [\cos(\phi_1) L_y - \sin(\phi_1) L_x] + \dots \right. \\
&\quad + \frac{1}{2} \left(\frac{m_2}{m_1} \mathbf{xS}_1 + \mathbf{xS}_2 \right) \rho_1 m_1^2 \chi_1 [\cos(\phi_1) y - \sin(\phi_1) x] + \dots \\
&\quad \left. - \frac{1}{2} m_1^2 m_2^2 \chi_1 \chi_2 \rho_1 \rho_2 [\cos(\phi_1) \sin(\phi_2) - \cos(\phi_2) \sin(\phi_1)] \right], \\
\frac{d\xi_2}{dt} &= \frac{2}{q^3} \left[\left(1 + \frac{3m_1}{4m_2} \right) m_2^2 \chi_2 \rho_2 [\cos(\phi_2) L_y - \sin(\phi_2) L_x] + \dots \right. \\
&\quad + \frac{1}{2} \left(\frac{m_1}{m_2} \mathbf{xS}_2 + \mathbf{xS}_1 \right) \rho_2 m_2^2 \chi_2 [\cos(\phi_2) y - \sin(\phi_2) x] + \dots \\
&\quad \left. - \frac{1}{2} m_1^2 m_2^2 \chi_1 \chi_2 \rho_1 \rho_2 [\cos(\phi_2) \sin(\phi_1) - \cos(\phi_1) \sin(\phi_2)] \right],
\end{aligned}$$

with the orbital angular momentum

$$\mathbf{L} = \begin{pmatrix} L_x \\ L_y \\ L_z \end{pmatrix} = \mathbf{x} \times \mathbf{p},$$

and the other quantities as introduced in 4.5.

E.

We give here the radiation force in our simulations of subsection 4.8.8. With the quantities of chapter 4 and the angular momentum as in the appendix above, the radiation contribution reads

$$\mathbf{F}_{\text{rad}} = \frac{1}{\omega \|\mathbf{L}\|} \frac{dE}{dt} \mathbf{p} + \frac{8}{15} \nu^2 \frac{v_\omega^8}{q \mathbf{L}^2} \left[\left(61 + 48 \frac{m_2}{m_1} \right) \mathbf{p} \mathbf{S}_1 + \left(61 + 48 \frac{m_1}{m_2} \right) \mathbf{p} \mathbf{S}_2 \right] \mathbf{L},$$

with

$$v_\omega = \left(\frac{Gm\omega}{c^3} \right)^{\frac{1}{3}},$$

$$\omega = \frac{\frac{d\mathbf{x}}{dt} - \left(\frac{d\mathbf{x}}{dt} \mathbf{n} \right) \mathbf{n}}{q},$$

and the ‘energy-loss rate’

$$\frac{dE}{dt} = -\frac{32}{5} \nu^2 v_\omega^{10} \left(1 + f_2 v_\omega^2 + [f_3 + f_{3\text{SO}}(\mathbf{p}, \mathbf{x}, \mathbf{S}_1, \mathbf{S}_2)] v_\omega^3 + \dots \right. \\ \left. + [f_4 + f_{4\text{SS}}(\mathbf{p}, \mathbf{x}, \mathbf{S}_1, \mathbf{S}_2)] v_\omega^4 + f_5 v_\omega^5 + [f_6 + f_{61} \ln(4v_\omega)] v_\omega^6 + f_7 v_\omega^7 \right).$$

With Euler’s gamma $\gamma_e = 0.577215$, the coefficients are

$$f_2 = -\frac{1247}{336} - \frac{35}{12} \nu^2,$$

$$f_3 = 4\pi,$$

$$f_4 = -\frac{44711}{9072} + \frac{9271}{504} \nu + \frac{65}{18} \nu^2,$$

$$f_5 = -\left(\frac{8191}{672} + \frac{583}{24} \nu \right) \pi,$$

$$f_6 = \frac{6\,643\,739\,519}{69\,854\,400} + \frac{16}{3} \pi^2 - \frac{1712}{105} \gamma_e + \left(-\frac{134\,543}{7776} + \frac{41}{48} \pi^2 \right) \nu - \dots \\ - \frac{94\,403}{3024} \nu^2 - \frac{775}{324} \nu^3,$$

$$f_{61} = -\frac{1712}{105},$$

$$f_7 = \left(-\frac{16\,285}{504} + \frac{214\,745}{1728} \nu + \frac{193\,385}{3024} \nu^2 \right) \pi,$$

$$f_{3\text{SO}}(\mathbf{p}, \mathbf{x}, \mathbf{S}_1, \mathbf{S}_2) = -\left(\frac{11}{4} + \frac{5m_2}{4m_1} \right) \frac{\mathbf{L}\mathbf{S}_1}{m^2 \|\mathbf{L}\|} - \left(\frac{11}{4} + \frac{5m_1}{4m_2} \right) \frac{\mathbf{L}\mathbf{S}_2}{m^2 \|\mathbf{L}\|},$$

$$f_{4\text{SS}}(\mathbf{p}, \mathbf{x}, \mathbf{S}_1, \mathbf{S}_2) = \frac{\nu}{48m_1^2 m_2^2} \left(289 \frac{(\mathbf{L}\mathbf{S}_1)(\mathbf{L}\mathbf{S}_2)}{\|\mathbf{L}\|^2} - 103(\mathbf{S}_1\mathbf{S}_2) \right).$$

References

- Arnowitt, R., S. Deser, and C. W. Misner 1962.
Republication in 2008 of: The dynamics of general relativity.
General Relativity and Gravitation **40**, 1997–2027.
- Benettin, G., L. Galgani, A. Giorgilli, and J.-M. Strelcyn 1978.
All Lyapunov characteristic numbers are effectively computable.
Academie des Sciences Paris Comptes Rendus Serie B Sciences Physiques **286**, 431–433.
- Benettin, G., L. Galgani, and J.-M. Strelcyn 1976.
Kolmogorov entropy and numerical experiments.
Phys. Rev. A **14**, 2338–2345.
- Blanchet, L. 2002.
Gravitational Radiation from Post-Newtonian Sources and Inspiralling Compact Binaries.
Living Reviews in Relativity **5**, 3.
- Buonanno, A., Y. Chen, and T. Damour 2006.
Transition from inspiral to plunge in precessing binaries of spinning black holes.
Phys. Rev. D **74**(10), 104005.
- Damour, T., P. Jaranowski, and G. Schäfer 2008.
Hamiltonian of two spinning compact bodies with next-to-leading order gravitational spin-orbit coupling.
Phys. Rev. D **77**, 064032.
- Damour, T., and G. Schafer 1988.
Higher-order relativistic periastron advances and binary pulsars.
Nuovo Cimento B Serie **101**, 127–176.
- Dieci, L., D. Russell, and v. E. S. 1997.
On the Computation of Lyapunov Exponents for Continuous Dynamical Systems.
SIAM Journal on Numerical Analysis **34**, 401–423.
- Einstein, A. 1915.
Die Feldgleichungen der Gravitation.
Sitzungsberichte der Königlich Preußischen Akademie der Wissenschaften (Berlin), Seite 844-847., 844–847.
- Flannery, B., W. Press, S. Teukolsky, and W. Vetterling 1992.
Numerical Recipes in C. The art of scientific computing (2 ed.).
Cambridge: Cambridge University Press.
- Galaviz, P., and B. Brügmann 2011.
Characterization of the gravitational wave emission of three black holes.
Phys. Rev. D **83**(8), 084013.
- Hairer, E., C. Lubich, and G. Wanner 2006.
Geometric Numerical Integration: Structure-Preserving Algorithms for Ordinary Differential Equations (2 ed.).
Berlin: Springer Verlag.

- Hairer, E., R. I. McLachlan, and A. Razakarivony 2008.
Achieving Brouwer's law with implicit Runge–Kutta methods.
BIT Numerical Mathematics.
- Hairer, E., S. P. Nørsett, and G. Wanner 1993.
Solving Ordinary Differential Equations I (2 ed.).
Berlin: Springer Verlag.
- Hairer, E., and G. Söderlind 2005.
Explicit, Time Reversible, Adaptive Step Size control.
SIAM Journal on Scientific Computing.
- Hairer, E., and G. Wanner 1996.
Solving Ordinary Differential Equations II: Stiff and Differential-Algebraic problems (2 ed.).
Berlin: Springer Verlag.
- Henon, M., and C. Heiles 1964.
The applicability of the third integral of motion: Some numerical experiments.
The Astronomical Journal **69**, 73.
- Higham, N. J. 1993.
The Accuracy of Floating Point Summation.
SIAM Journal on Scientific Computing.
- Jaranowski, P., and G. Schäfer 2001.
Erratum: Third post-Newtonian higher order ADM Hamilton dynamics for two-body point-mass systems [Phys. Rev. D 57, 7274 (1998)].
Phys. Rev. D **63**(2), 029902.
- Katsanikas, M., and P. A. Patsis 2011.
The Structure of Invariant Tori in a 3d Galactic Potential.
International Journal of Bifurcation and Chaos **21**, 467.
- Kerr, R. P., and A. Schild 1963.
Republication in 2009 of: A new class of vacuum solutions of the Einstein field equations.
General Relativity and Gravitation **41**, 2485–2499.
- Laskar, J. 1990.
The chaotic motion of the solar system - A numerical estimate of the size of the chaotic zones.
Icarus **88**, 266–291.
- Liao, X. 1997.
Symplectic Integrator for General Near-Integrable Hamiltonian System.
Celestial Mechanics and Dynamical Astronomy **66**, 243–253.
- Lubich, C., B. Walther, and B. Brüggemann 2010.
Symplectic integration of post-Newtonian equations of motion with spin.
Phys. Rev. D **81**(10), 104025.
- Manko, V. S., J. D. Sanabria-Gómez, and O. V. Manko 2000.
Nine-parameter electrovac metric involving rational functions.
Phys. Rev. D **62**(4), 044048.

-
- Meiss, J. D. 1992.
Symplectic maps, variational principles, and transport.
Reviews of Modern Physics **64**, 795–848.
- Newton, S. I. 1687.
Philosophiae naturalis principia mathematica.
London.
- Papapetrou, A. 1951.
Spinning Test-Particles in General Relativity. I.
Royal Society of London Proceedings Series A **209**, 248–258.
- Schäfer, G. 1997.
Post-Newtonian Approximations and Equations of Motion of General Relativity.
Banach Center Publications, Warsaw.
- Schwarzschild, K. 1916.
On the Gravitational Field of a Mass Point According to Einstein's Theory.
Abh. Königl. Preuß. Akad. Wissenschaften Jahre 1906,92, Berlin,1907, 189–196.
- Stoffer, D. 1988.
On reversible and canonical integration methods.
SAM-Report ETH Zürich.
- Tancredi, G., A. Sánchez, and F. Roig 2001.
a Comparison Between Methods to Compute Lyapunov Exponents.
The Astronomical Journal **121**, 1171–1179.
- Wu, X., T.-Y. Huang, and H. Zhang 2006.
Lyapunov indices with two nearby trajectories in a curved spacetime.
Phys. Rev. D **74**(8), 083001.
- Wu, X., and Y. Xie 2010.
Symplectic structure of post-newtonian hamiltonian for spinning compact binaries.
Phys. Rev. D **81**, 084045.
- Zhong, S.-Y., X. Wu, S.-Q. Liu, and X.-F. Deng 2010.
Global symplectic structure-preserving integrators for spinning compact binaries.
Phys. Rev. D **82**(12), 124040.

List of Figures

- 2.1. Motion in the Hénon-Heiles potential: For the energy $H = 1/8$, the trajectory in the configuration space of a regular orbit with initial conditions $x = y = p_y = 0$, $p_x = \frac{1}{2}$ is plotted in the left panel. The right panel shows a chaotic orbit with initial conditions $x = p_y = 0$, $x = -0.1$, $p_x = \sqrt{\frac{359}{1500}}$ 14
- 2.2. Poincaré sections at $x = 0$ for the orbits of Fig. 2.1 calculated with the ‘exact’ solution. The left panel shows the regular case (2.2) and the right panel depicts sections of the chaotic orbit (2.3). 15
- 2.3. Relative error of the Hamiltonian ΔH as a function of time $t \in [0, 10^6]$ for a structure preserving algorithm and the explicit RK4 scheme for the Hénon-Heiles potential with regular initial values. 17
- 2.4. Poincaré sections at $x = 0$ for the regular orbit (2.2) calculated with the classical Runge-Kutta scheme, $h = 0.01$ (left panel) and with the Störmer-Verlet method, $h = 0.01$ (right panel). 18
- 2.5. For the time intervals $I_1 = [0, 15000]$ and $I_2 = [10^6 - 15000, 10^6]$, the Fourier spectrum of x , $|f(\omega)^x| = \left| \int_{I_i} e^{i\omega t} x(t) dt \right|$ is plotted. The left panel corresponds to the regular orbit (2.2), the right panel shows the spectrum of the chaotic orbit (2.3). 19
- 2.6. For our regular test orbit in the Hénon-Heiles potential, the left panel shows the frequency spectrum of the x component in the intervals $I_1 = [0, 1500]$ and $I_2 = [28500, 30000]$ obtained with an explicit Euler scheme. In the right panel, an RK4 scheme was applied to calculate the frequency spectrum in the intervals $I_1 = [0, 15000]$ and $I_2 = [10^6 - 15000, 10^6]$ 19
- 2.7. The evolution in time of the Lyapunov exponents λ_i once calculated with the discrete QR method (left panel) and once obtained via the continuous QR algorithm. Both panels also show the LE as a function of time. 23
- 2.8. The evolution in time of LE calculated with the variational and the two-particle method. The left panel shows the result for the regular orbit (2.2). The LE for the chaotic case 2.2 is shown in the right panel in double logarithmic scale. . . 25
- 2.9. The Fast Lyapunov Indicator (FLI) against time for the regular orbit (2.2) (left panel) and the chaotic test case (2.3) (right panel) in semi-logarithmic scale. . 25
- 3.1. For the case $\rho = 30.7$ the left panel is showing the ρ, z -projection of the trajectory of the light particle in the time interval $\tau \in [0, 500\,000]$. The corresponding sections of the $z = 0$ -plane are depicted in right panel. The plots clearly correspond to quasiperiodic motion. N.b.: The quantity along the right panel’s vertical axis is the ‘momentum’ $p_\rho = \dot{\rho}$ as introduced in 3.9. 47
- 3.2. The relative error in the Hamiltonian for the respective integration schemes with initial condition $\rho = 30.7$. The explicit schemes show a linear drift but the other integrators conserve the energy. 47
- 3.3. For the case $\rho = 1.7$ the left panel is showing the ρ, z -projection of the trajectory of the light particle in the time interval $\tau \in [0, 500\,000]$. The corresponding sections of the $z = 0$ -plane are depicted in the right panel. The Poincaré section shows the quasiperiodic character of the motion but the trajectory behaves in a more ill-mannered way. N.b.: The quantity along the right panel’s vertical axis is the ‘momentum’ $p_\rho = \dot{\rho}$ as introduced in 3.9. 48
- 3.4. The variable step size of the IGEM integrator as function of integration time τ . 49

3.5.	The relative error ΔH as function of the proper time τ in normal scale for the orbit with $\rho = 1.7$	49
3.6.	The relative error err at the Poincaré sections as function of the proper time τ in normal scale for the orbit with $\rho = 1.7$	50
3.7.	Poincaré sections for the case $\rho = 1.7$ for an integration time $\tau \in [0, 500\,000]$. All plots resemble the exact Poincaré section shown in the bottom right panel.	51
3.8.	For the case $\rho = 0.7$ the left panel is showing the ρ, z -projection of the trajectory of the light particle in the time interval $\tau \in [0, 5000]$. The unusual Poincaré section as shown in the right panel suggests chaotic motion.	52
3.9.	For the case $\rho = 0.7$ and the the time interval $\tau \in [0, 5000]$, the spectrum of frequencies $ f(\omega)^\rho = \int e^{i\omega\tau}\rho(\tau)d\tau $ clearly shows the characteristic noise of chaotic orbits. A magnification of the Fourier spectrum is shown in the embedded panel.	52
3.10.	The relative error ΔH in semi-logarithmic scale for the IGEM with $\epsilon = 0.1$ as a function of proper time τ for the chaotic orbit with $\rho = 0.7$	53
3.11.	The 'velocity' $V(\tau)^2$ as function of proper time τ for the chaotic orbit with $\rho = 0.7$	54
3.12.	The trajectory of the test particle for $\tau \in [2286, 2306]$. The points correspond to the trajectory calculated by IGEM whereas the continuous line gives the 'accurate' trajectory. One can see how the test particle bounces back once having arrived at $\rho = 0.66$	55
3.13.	Difference between IGEM and the 'accurate' solution directly after the first inflexion at $\tau_{\text{infl}} = 2296$	55
3.14.	For the chaotic test case and $\tau \in [0, 50000]$, the error in the energy at the Poincaré sections obtained via IGEM with $\epsilon = 0.1$ and $s = 4$ and the help of the collocation algorithm is compared with the error along the trajectory for the same integrator.	57
4.1.	The energy error ΔH as a function of time t for the integrators $\varphi_{N,h}$ ('analytical') and $\Phi_{\text{Kep},h}$ ('numerical') in the time interval $t \in [0, 10^7]$ for various step sizes h	74
4.2.	For the test case without spin contributions and $t \in [0, 10^7]$, the left panel shows an extract of the trajectory. The Poincaré sections for $y = 0$ and $p_y > 0$ are given in the right panel.	76
4.3.	For the test case (4.132), the left panels shows the trajectory for $t \in [0, 50000]$. The frequency spectra $ f^x(\omega) $ for the time intervals $I_1 = [0, 10^6]$ and $I_2 = [10^7 - 10^6, 10^7]$ are depicted in the right panel.	76
4.4.	For the chaotic test case, the left panel shows the trajectory for $t \in [0, 25000]$. The linearly growing FLI is depicted in the right panel in semi-logarithmic scale.	77
4.5.	For initial data (4.131), $t \in [0, 10^7]$ and different step sizes h , the relative error in the Hamiltonian ΔH is plotted against time t for the splitting integrators of section 4.6, PoissonII (orange), SympII (light blue), PoissonI (magenta), and SympI (black).	78
4.6.	For initial data (4.132), $t \in [0, 10^7]$ and different step sizes h , the relative error in the Hamiltonian ΔH is plotted against time t for the splitting integrators of section 4.6, PoissonII (orange), SympII (light blue), PoissonI (magenta), and SympI (black).	78
4.7.	For initial data (4.133), $t \in [0, 10^7]$ and different step sizes h , the relative error in the Hamiltonian ΔH during simulations with SympI is plotted against time t	80

4.8. For initial data (4.133) and a step size $h = 0.1$, the relative error in the Hamiltonian ΔH is plotted against time t for the PoissonI scheme.	81
4.9. For initial data (4.132) and $t \in [0, 10^7]$, the relative error along the trajectory err is plotted against time t for various integration schemes.	83
4.10. For initial data (4.132) and $t \in [0, 10^7]$, the relative error in the Hamiltonian ΔH is plotted against time t for various integration schemes.	83
4.11. For initial data (4.133), the relative error along the trajectory err is plotted against time t for various integration schemes.	84
4.12. For initial data (4.133) and $t \in [0, 10^7]$, the relative error in the Hamiltonian ΔH is plotted against time t for various integration schemes.	84
4.13. For the three methods to calculate Poincaré sections, initial data (4.133), and $t \in [0, 10^7]$, the relative error in the Hamiltonian on the section ΔH_{sect} is plotted against time t in the left panel. The right panel shows the same for initial values (4.131).	86
4.14. Poincaré sections at $y = 0$, $p_y > 0$ for the purely orbital test case obtained with RK4 and four different step sizes h	86
4.15. For the classical RK4 scheme applied with different step sizes h to the purely orbital test case, the error in the energy ΔH is plotted against integration time t	87
4.16. The left panel shows Poincaré sections at $y = 0$, $p_y > 0$ for the purely orbital test case obtained with Gauss3 and $h = 40$. In the right panel, the corresponding error in the energy ΔH is plotted against integration time t	87
4.17. The left panel shows the exact solution and the result obtained via Gauss3 and $h = 40$ of the maximum Lyapunov exponent λ for the purely orbital test case. In the right panel, the same results, with $h = 0.5$ instead of $h = 40$ for Gauss3, are plotted for the chaotic test case.	88
4.18. The left panel shows the exact solution and the result obtained via RK4 and $h = 40$ for the maximum Lyapunov exponent λ for the purely orbital test case. In the right panel, the same results, with $h = 0.5$ instead of $h = 40$ for RK4, are plotted for the chaotic test case.	89
4.19. The maximum Lyapunov exponent λ obtained via integrations with small step sizes compared with the exact solution. The left panel shows the result for explicit schemes, the right panel is the same for Gauss collocation methods.	89
4.20. The frequency spectra of the x-component, $ f^x(\omega) $, with arbitrary normalization in the intervals $I_1 = [0, 10^6]$ and $I_2 = [10^7 - 10^6, 10^7]$ as obtained by the RK4 method with different step sizes.	90
4.21. The left panel shows the frequency spectra of the x-component, $ f^x(\omega) $, with arbitrary normalization in the intervals $I_1 = [0, 10^6]$ and $I_2 = [10^7 - 10^6, 10^7]$ as obtained by Gauss3 with $h = 40$. The right panel depicts the corresponding exact solution.	90
4.22. The radial distance q as function of integration time t for the regular spinning orbit with radiation effects included.	91
4.23. The relative error along the trajectory, err against integration time t for explicit and collocation schemes.	92

List of Tables

2.1.	The CPU calculation times for the QR algorithms are compared with the CPU times for the calculation of the LE.	23
3.1.	The CPU calculation times for the proper time interval $\tau \in [0, 500\,000]$ for the individual integration schemes in the quasiperiodic case $\rho = 30.7$	48
3.2.	The calculation times T_{calc} for the proper time interval $\tau \in [0, 500\,000]$ for the different integrators in the case of the still regular orbit with $\rho = 1.7$	50
3.3.	Results of the simulations for the chaotic orbit with $\rho = 0.7$	53
4.1.	Comparison of the calculation times for the integrators $\varphi_{N,h}$ and $\Phi_{\text{Kep},h}$ applied with different step sizes h to the Kepler problem in the time interval $t \in [0, 10^7]$	73
4.2.	The CPU calculation times in [s] for the splitting integrators of section 4.6 applied to the regular test case (4.131) with different step sizes h . The integration interval was $t \in [0, 10^7]$ in all simulations. N.b.: As the spin contributions are turned off, methods I and II are the same in this case.	79
4.3.	The CPU calculation times in [s] for the splitting integrators of section 4.6 applied to the regular, spinning test case (4.132) with different step sizes h . The integration interval was $t \in [0, 10^7]$ in all simulations.	79
4.4.	The CPU calculation times in [s] for the splitting integrator SympI applied to the chaotic test case (4.133) with different step sizes h . The integration interval was $t \in [0, 10^7]$ in all simulations. ‘a’ signifies ‘aborted due to condition (4.125)’.	80
4.5.	The CPU calculation times in [s] for explicit and implicit Runge-Kutta schemes applied to the orbital test case (4.132) with different step sizes h . The integration interval was $t \in [0, 10^7]$ in all simulations. ‘a’ signifies ‘aborted due to condition (4.125)’.	81
4.6.	The CPU calculation times in [s] for explicit and implicit Runge-Kutta schemes applied to the regular, spinning test case (4.132) with different step sizes h . The integration interval was $t \in [0, 10^7]$ in all simulations. ‘a’ signifies ‘aborted due to condition (4.125)’.	82
4.7.	The CPU calculation times in [s] for explicit and implicit Runge-Kutta schemes applied to the chaotic test case (4.132) with different step sizes h . The integration interval was $t \in [0, 10^7]$ in all simulations. ‘a’ signifies ‘aborted due to condition (4.125)’, ‘-’ means that no simulation has been run for the corresponding step size.	82
4.8.	Number of iterations per step for Gauss4, applied with different step sizes to the three test cases. ‘a’ signifies ‘aborted due to condition (4.125)’, ‘-’ means that no simulation has been run for the corresponding step size.	82
4.9.	The CPU calculation times in [s] for the calculation of all Poincaré sections of the $y = 0$ -plane for $t \in [0, 10^7]$ with Gauss3 and the three algorithms of subsection 2.2.1.	85
4.10.	The CPU calculation times in [s] for explicit and implicit Runge-Kutta schemes applied with different step sizes h to the test case (4.132) with radiation effects included. The integration interval was $t \in [0, 500\,000]$ for all simulations.	92